HYDRATION CHARACTERISTICS OF ATMOSPHERIC AEROSOL IN U.S. NATIONAL PARKS

A Dissertation

by

NATHAN FRANK TAYLOR

Submitted to the Office of Graduate and Professional Studies of
Texas A&M University
in partial fulfillment of the requirements for the degree of

DOCTOR OF PHILOSOPHY

Chair of Committee,	Don Collins
Committee Members,	Sarah Brooks
	Qi Ying
	Renyi Zhang
Head of Department,	Ping Yang

May 2017

Major Subject: Atmospheric Sciences

ABSTRACT

Interactions with atmospheric water are central to aerosol impacts on health, climate, and visibility. Many atmospheric aerosol constituents take up water in sub-saturated conditions, enhancing their impact on climate and visibility by modifying the efficiency with which they scatter and absorb radiation. Particulate water also affects the evolution and fate of atmospheric aerosol, typically increasing the uptake of reactive and soluble trace gases, enhancing aerosol growth in both sub-saturated conditions and through cloud processing.

This dissertation explores the hydration characteristics of two major fractions of atmospheric aerosol: sulfates and water soluble organic carbon (WSOC). A series of four month-long measurement campaigns were conducted in three U.S. National Parks evaluating their role in visibility impairment and the validity of two assumptions in regulatory programs addressing visibility. First, while it is well known that under some atmospheric conditions sulfate aerosols exhibit two alternative hydration states—one aqueous, one crystalline—current regulatory programs assume that all atmospheric sulfate is aqueous and few measurements have tested this assumption. These campaigns included such measurements. During all studies, at least some aerosols with two possible hydration states under ambient conditions were detected (ranging from 4% at Acadia NP to 53% at Great Smoky Mountains NP in winter). Only during the winter at Great Smoky Mountains were aerosol found in both hydration states: 65 % of in the more hydrated state, 35 % in the less hydrated state. Otherwise, only the more hydrated

alternative was occupied. We explore how these findings are related to composition, ambient RH, and other atmospheric conditions.

Next, we consider the uptake of water by WSOC in aerosol, which current U.S. regulations treat as negligible. During the four national park studies, and a fifth in remote northern Colorado, WSOC was captured on filters and isolated using selectively adsorptive resins. The ability of this WSOC to take up water or serve as a cloud condensation nuclei was measured. Across all sampling locations and seasons, the hygroscopic growth of WSOC samples at 90% RH, expressed in terms of the hygroscopicity parameter, κ, ranged from 0.05 – 0.15.

DEDICATION

This dissertation is dedicated to my wife, Jill, for unending patience and encouragement.

ACKNOWLEDGEMENTS

I would like to thank the Electric Power Research Institute and National Science Foundation for supporting this research. Also, I gratefully acknowledge the cooperation and support of the park staff at Great Smoky Mountains, Mt. Rainier, and Acadia National Parks during these measurement campaigns. Additionally, I would like to thank my editors at *Aerosol Chemistry and Physics*, Professors Barbara Ervens (Chapter II) and Dr. Armin Sorooshian (Chapter III).

I would also like to recognize my advisor, Professor Don Collins. This work would have been impossible without his patience, support, and direction.

CONTRIBUTORS AND FUNDING SOURCES

Contributors

This work was supervised by a dissertation committee consisting of my advisor, Professor Don Collins; Professors Sarah Brooks and Renyi Zhang in the Department of Atmospheric Sciences; and Professor Qi Ying of the Department of Civil Engineering.

The research reported here was conducted in collaboration with Professor Don Collins and with Dr. Douglas Lowenthal, Research Professor in the Division of Atmospheric Sciences at the Desert Research Institute, Reno, NV.

Funding Sources

This work was primarily supported by grants from the Electric Power Research Institute in Palo Alto, CA, under the direction of Dr. Naresh Kumar. The research conducted at Storm Peak Lab, reported in Chapter III, was supported by the National Science Foundation through collaborative grants AGS-0931431, AGS-0931910, AGS-0931505, and AGS-0931390. These chapters are solely the responsibility of the authors and do not necessarily represent the official views of EPRI or the NSF.

TABLE OF CONTENTS

Page

LIST OF FIGURES

Page

LIST OF TABLES

CHAPTER I

INTRODUCTION AND LITERATURE REVIEW

This dissertation centers on analysis of hydration characteristics of atmospheric aerosol in U.S. National Parks during a series of field campaigns from 2006 – 2011. The experiments and *in situ* measurements were designed to evaluate elements of the IMPROVE program, part of the regulatory implementation of the Clean Air Act provisions protecting visibility within the National Parks. Beyond visibility, the interactions between atmospheric aerosol and water investigated in these projects influence the role aerosols play in Earth's climate, their impacts on human health, and the aging and fate of the aerosols themselves. The findings of these studies are thus relevant in both the narrow regulatory context and broader field of aerosol science.

IMPROVE Program and Studies

History and Objectives

The Interagency Monitoring of Protected Visual Environments (IMPROVE) program is part of the regulatory implementation of Section 169A of the Clean Air Act (CAA), 42 U.S.C. § 7491. Enacted with the 1977 CAA amendments, § 169A directed the EPA administrator to identify "mandatory class I Federal areas . . . where visibility is an important value of the area." Among 158 class I areas--which include all international parks, all national parks over 6,000 acres in size, and all national memorial parks and wilderness areas over 5,000 acres (CAA § 162)—the administrator identified 156 where visibility protections were warranted (40 CFR 81). CAA §169A further

required the EPA to promulgate rules assure progress toward "the prevention of any future, and the remedying of any existing, impairment of visibility in mandatory class I Federal areas which impairment results from manmade air pollution." Similar to other CAA provisions, this was to be accomplished by the states, which were to incorporate federal standards into State Implementation Plans (SIPs) (CAA § 169A(b)(2)). A crucial aspect of these SIPs was developing strategies to quantify visibility impairment, attribute the impairment to sources and types of air pollution, and eventually remedy manmade pollution resulting in visibility impairment (CAA § 169A(a)(3)).

In response to uncertainty about the sources of visibility impairment, the EPA began in 1980 to issue regulations that only required states to cure 'plume blight' in class I areas within their borders—visibility degradation easily attributable to a particular source—but did not attempt to resolve the more complex problem of undifferentiated, regional haze (Visibility Protection for Federal Class I Areas, 45 Fed. Reg. 80084, Dec. 2). By 1982, 35 states had made no move to incorporate even plume blight protections into their environmental programs, and EPA still had not taken steps toward regional-haze regulation (Beissinger et al., 2017). This intransigence prompted environmental advocacy groups to file suit against the EPA seeking to compel action on regional haze and force the EPA to take control of state programs that had not responded to the 1980 regulations. The EPA eventually settled with environmental groups and began taking action.[1] In 1984, the EPA and federal land managers (FLMs) convened an interagency

[1] These suits were part of a very large, coordinated campaign by environmental groups to oppose de-regulation and non-enforcement by the Regan administration. This particular settlement occurred shortly after the resignation of Anne Gorsuch as EPA administrator in 1983.

task force to study regional haze and in 1985, the EPA promulgated federal rules for states that had not taken appropriate action on plume blight (Sisler et al., 1993).[2] As a result, federal, rather than state, agencies initially assumed responsibility to evaluate sources of regional haze and design remedial programs.

The IMPROVE program was created in 1985 as a cooperative program by the EPA and other federal agencies to achieve the monitoring and pollutant attribution tasks required by CAA § 169A and the 1984 settlement (Sisler et al., 1993). Its original objectives were to (1) assess visibility impairment within mandatory class I areas, (2) identify chemical species and emission sources responsible for existing anthropogenic visibility impairment, and (3) document long-term trends for assessing progress towards the national visibility goal (Sisler et al., 1993). It incorporated an existing network of 16 air quality monitors administered by the National Park Service, adding 20 additional sites by 1993, expanding to 110 IMPROVE protocol sites in 1999 following the promulgation of the Regional Haze Rule, and now includes ~170 sites, shown in Fig. 1 (Sisler et al., 1993; IMPROVE Web Site, 2017). Over time, most states promulgated acceptable SIPs and regained regulatory control over remediation; however, most states have elected to participate in the IMPROVE program to fulfil their obligations to assess visibility impairment and its causes. As a result, IMPROVE is now supported and

[2] The CAA is a cooperative federalism statute, with complementary roles for states and the federal government. Typically, states are required to prepare plans (SIPs) to comply with federal standards. This allows states a fair degree of flexibility in allocating the burden of compliance among pollution sources. When states fail to comply with federal standards, or promulgate defective SIPs, the federal government may issue Federal Implementation Plans (FIPs) which strip states of control. This is a major mechanism of federal enforcement.

governed by federal agencies, regional state planning organizations, and even international participants such as Air Canada (Hand et al., 2011).

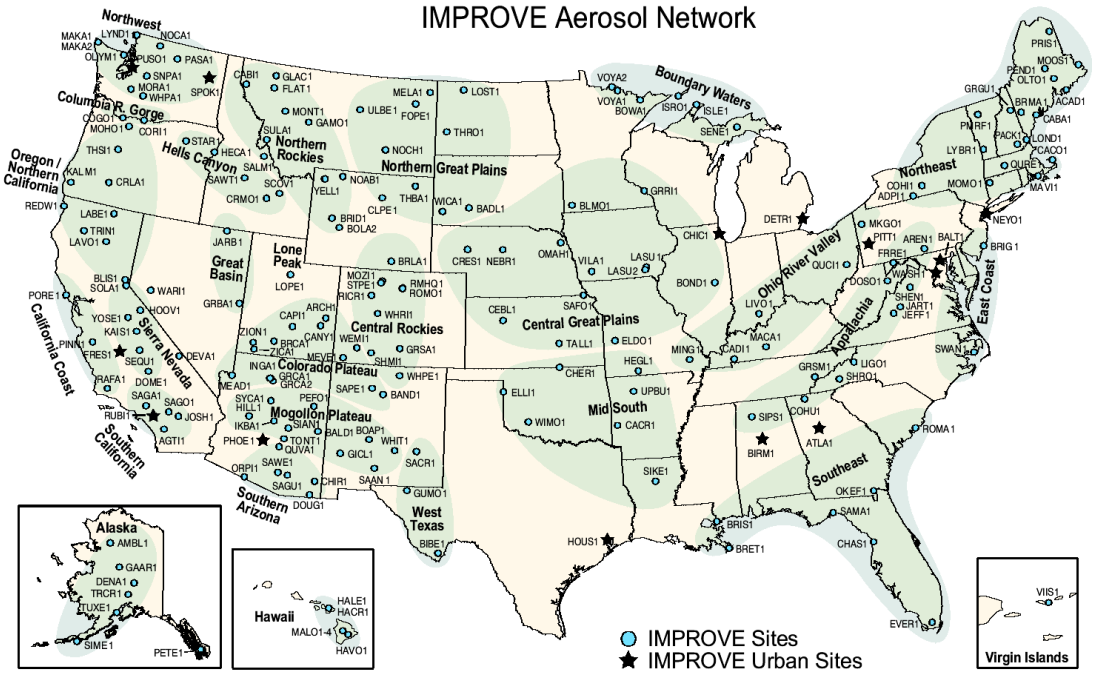

Figure 1: Map of current (170) and discontinued (42) IMPROVE sites from Hand et al. (2011). The vast majority of sites are located in class I areas.

The IMPROVE Protocol and the Light Extinction Reconstruction Equation (LIRE)

The IMPROVE program seeks to link measured visibility impairment to pollution categories and sources to guide remediation efforts. As the initial EPA report to Congress on possible methods of attributing anthropogenic aerosol following the passage of CAA § 169A recognized, light scattering and absorption by atmospheric particulates is primarily responsible for visibility impairment (EPA, 1979). Thus, the IMPROVE network developed to both measure ambient visibility and analyze ambient

aerosols to determine their likely source. The program settled on filter based aerosol measurements and analysis for the major chemical constituents (Sisler, 1993). From this specieated aerosol mass, algorithms were developed to predict the contribution of each constituent to visibility impairment with the intent of apportioning causes and achieving closure with directly measured visibility (Malm et al., 1994). Notably, because of their facility in source attribution and remediation, under EPA regulations the required visibility monitoring must rely on aerosol measurements, rather than direct visibility measurement (Regional Haze Regulations, 64 FR 35714). Aerosol-based visibility is to be estimated by the IMPROVE Light Extinction Reconstruction Equation (LIRE) and its validity is the primary question driving the studies reported in this dissertation.

Aerosol are sampled at IMPROVE protocol sites by bank of four filters, concurrently operated with a "1-day-in-3" sample period (midnight-to-midnight) and analyzed remotely by the University of California, Davis Campus, and Desert Research Institute in Reno, NV (Pitchford et al., 2007). Three of the four filters sample PM2.5. In the first, PM2.5 is captured on a Teflon filter for X-ray florescence elemental analysis of atomic numbers 11-82 (plus hydrogen), gravimetric mass (at ~40% RH), and aerosol absorption using an integrating sphere system (Hand et al., 2011). The second PM2.5 sample, on nylon, is analyzed for sulfate, nitrate, and chloride ions using ion chromatography (Hand et al., 2011). Finally, organic and elemental (or 'light absorbing') carbon is analyzed on a quartz filter using thermal optical reflectance (TOR) (Hand et al., 2011; Chow, 2004). The fourth filter is used to obtain gravimetric mass of PM10.

The current EPA regulation on visibility is the Regional Haze Rule (RHR) (40 CFR § 51.308) which provides that visibility must be assessed from aerosol-based reconstructions as described in EPA guidance documents. The latest guidance incorporates the reconstruction equation described in Pitchford et al. (2007), but allows states to diverge from this formulation with justification.[3] The Pitchford LIRE translates the IMPROVE measurements to visibility impairment as follows: First, an extinction coefficient is derived from IMPROVE masses (Pitchford et al., 2007).

$$
\begin{aligned}
\text{(eq. 1)}\ b_{ext} = {} & 2.2 \cdot f_S(RH) \cdot [\text{Small Sulfate}] + \\
& 4.8 \cdot f_L(RH) \cdot [\text{Large Sulfate}] + \\
& 2.4 \cdot f_S(RH) \cdot [\text{Small Nitrate}] + \\
& 5.1 \cdot f_L(RH) \cdot [\text{Large Nitrate}] + \\
& 2.8 \cdot [\text{Small Organic Mass}] + \\
& 6.1 \cdot [\text{Large Organic Mass}] + \\
& 10 \cdot [\text{Elemental Carbon}] + \\
& 1 \cdot [\text{Fine Soil}] + \\
& 1.7 \cdot f_{SS}(RH) \cdot [\text{Sea Salt}] + \\
& 0.6 \cdot \text{PM10} + \\
& b_{Rayleigh}(\text{elev., temp.}) + \\
& 0.33 \cdot NO_2(\text{ppb})
\end{aligned}
$$

In this formulation bracketed values are filter derived PM2.5 mass loading ($\mu g/m^3$) (see Hand et al., 2011, for details of the retrieval). The mass scattering coefficients for sulfate and nitrate are derived using standard Mie scattering calculations for 550 nm light and assuming particles fall into either a small (0.2 μm) and large (0.5 μm), and are

[3] Pitchford et al. (2007) reports the scientific basis of an equation promulgated by the IMPROVE Steering Committee to address biases reported for the original IMPROVE equation.

fully neutralized by ammonium. Mass is allocated between the modes based on total sulfate, nitrate, or organic mass (Pitchford et al., 2007).

(eq. 2)
$$m_i < 20\ \mu g: \begin{cases} m_{i,small} = m_i \cdot 0.8 \\ m_{i,large} = m_i \cdot 0.2 \end{cases}$$
$$m_i \geq 20\ \mu g: \begin{cases} m_{i,small} = 0 \\ m_{i,large} = m_i \end{cases}$$

Finally, recognizing that hygroscopic growth renders the mass scattering efficiency of sulfate, nitrate, and sea salt highly dependent on RH, the equation includes RH corrections as depicted in Fig. 2 (available at the IMPROVE web site). These curves were derived from similar Mie scattering calculations as the basic mass scattering efficiency values, treating the increased size and decreased refractive index that accompanies hygroscopic growth (Pitchford et al., 2007). For purposes of visibility impairment assessments, as most IMPROVE sites lack RH measurements, the IMPROVE program and RHR rely on month long climatological averages of RH (EPA Guidance, 2016) which are illustrated in Fig. 3.

The extinction coefficient, b_{ext}, is translated into the regulatory visibility impairment measure, *deciview*, which contrasts the current visibility with an approximation of pristine, aerosol-free conditions (Pitchford and Malm, 1994).

(eq.3) $$deciview = 10 \cdot \ln(b_{ext}/0.01\ km^{-1})$$

RHR standards require states to progress toward set visibility goals on a linear path in *deciviews* by the year 2064 (Pitchford et al., 2007).

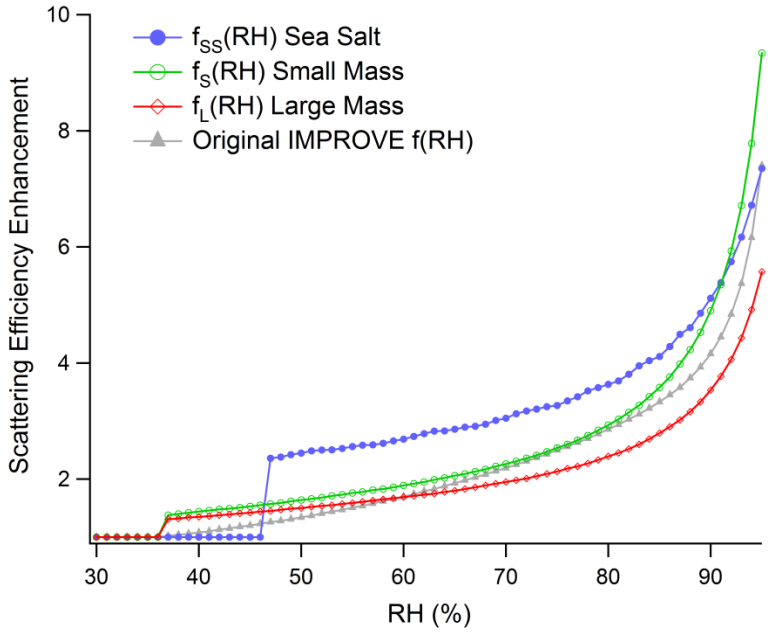

Figure 2: IMPROVE predicted scattering enhancement by hygroscopic growth for sea salt, and large and small nitrate and sulfate (Pitchford et al., 2007). Nitrate and sulfate share RH curves in the Pitchford et al., (2007) LIRE. In the original IMPROVE LIRE large and small mass were not differentiated (nor was sea salt treated). Data from IMPROVE website and Pitchford et al., (2007).

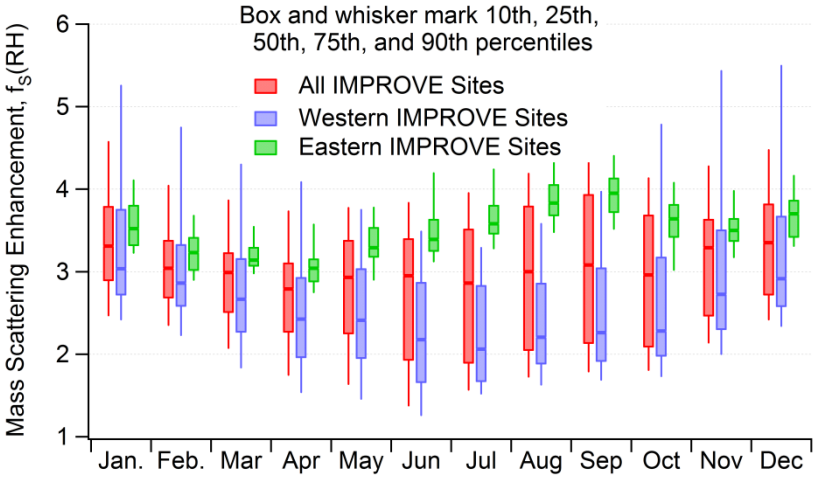

Figure 3: Distribution of monthly f_S(RH) values based on IMPROVE climatological means from EPA Guidance (2016). RH is the climatological monthly average RH at each IMPROVE site for all IMPROVE utilized in the EPA Guidance (2016) and IMPROVE website. Eastern and Western sites are divided at 97°W (i.e., between Dallas and Ft. Worth).

Advanced IMPROVE Studies: Investigating LIRE Assumptions

The LIRE hygroscopicity parameterizations play a critical role in assessing the contribution of pollutants like sulfate to visibility degradation. As depicted in Fig. 3, small sulfate and nitrate particles are expected to scatter 200% more light at most IMPROVE sites than raw mass loading would indicate. Consequently, these formulations have been scrutinized and constantly revisited since the original formulation provided by Malm et al. (1994). In point of fact, the measurements of aerosol-water interactions reported in this dissertation were part of a program of field campaigns investigating the validity of the RH parameterizations used by the IMPROVE program (Lowenthal et al., 2014).

The original IMPROVE LIRE relied on a single f(RH) that applied to all PM2.5 sulfate and nitrate (Fig. 2) and did not account for sea-salt (Malm et al., 1994). This parameterization came under heightened scrutiny when it was incorporated into the RHR in 1999, culminating in the revised LIRE that modified the original hygroscopicity parameterization in three ways.

First, as described in Pitchford et al. (2007), and earlier reviews (Lowenthal and Kumar, 2003, Ryan et al., 2005, Hand and Malm, 2006), this LIRE tended to slightly under-predict scattering (vs. nephelometer measurements) on the most (>20^{th} percentile) polluted days but over-predict elsewhere. This partially motivated the adoption of the large/small division among sulfate, nitrate, and organic mass (Ryan et al., 2005, Hand and Malm, 2006). The f(RH) curves were also recalculated to be consistent with the hypothetical small (0.2 μm) and large (0.5 μm) modes, and now reflect the greater

sensitivity of smaller particles to size changes in this portion of the scattering regime (Pitchford et al. 2007).

The second major change from the original LIRE was the incorporation of sea salt and sea salt hygroscopicity, partly in response to criticism by Lowenthal and Kumar (2003). The current treatment assumes PM2.5 sea salt is, in fact, characterized by a diameter of 2.5 μm (for Mie calculations), which is reflected in its low mass scattering efficiency despite a relatively high refractive index of 1.5. This choice is also reflected in $f_{SS}(RH)$, shown in Fig. 2, which contains ripples corresponding to wavelength harmonics (here 550 nm) in the Mie scattering calculations.

The third change from the original LIRE f(RH) involved the assumptions about aerosol hydration state—whether crystalline salts exist in the atmosphere or if meta-stable, hydrated forms dominate. These assumptions motivated the measurements of aerosol hydration state reported in Chapter II and are explained in greater detail. In the original LIRE f(RH), the fraction of ammonium sulfate and nitrate assumed to be crystalline (f(RH) = 1) transitioned gradually from 1.0 to 0.0 as RH increased from ~35% to 60% (see Fig. 2). Based partly on the recommendation by Hand and Malm (2006) that f(RH) for sulfates and nitrates be based on an assumption of 'no solids,' the current LIRE assume that all particles are meta-stably hydrated (Pitchford et al., 2007). It is notable that, because of the RHR's reliance on monthly-average RH with the results

illustrated in Fig. 3, these assumptions are irrelevant for the majority of IMPROVE sites where average RH is always above 60%.[4]

Finally, despite some discussion in IMPROVE reviews (Malm and Day, 2001, El-Zanan et al., 2005), the updated LIRE did not adopt any parameterization of organic aerosol hygroscopicity. The discussion by Pitchford et al. (2007) indicates that the IMPROVE Steering Committee saw too much uncertainty to make a positive recommendation, but called for further study.

This dissertation primarily presents findings from a measurement campaign in the line of research scrutinizing the scientific basis of the IMPROVE LIRE (Lowenthal et al. 2014). It was initiated before the second LIRE was incorporated, but the questions it addressed are still open. The experiments reported in Chapter II were designed to address the validity of the LIRE assumptions on aerosol hydration state. The bulk of Chapter II was published in Taylor et al. (2009) and presents direct measurements of ambient aerosol hydration state in several U.S. National Parks, concluding that both crystalline and meta-stable aerosols exist naturally. The experiments described in Chapter III were designed to evaluate the contribution of organic particulate matter to water uptake. The results, published in Taylor et al. (2017), not only demonstrate a consistent hygroscopic fraction of organic aerosol during these studies, but suggest that internal mixtures of soluble organic and inorganic compounds may take up more water at atmospherically relevant RH than in isolation.

[4] The increase in f(RH) at low RH that results from assuming meta-stably hydrated, rather than crystalline, sulfate tends to enhance IMPROVE derived visibility impairment on the days with best visibility. The regulatory impact of this enhancement is to increase the acceptable pollution level. The RHR requires states to adopt practices that do not further impair the 20% best visibility days at class I sites (40 C.F.R. § 51.308); where that impairment is enhanced, the latitude for states is increased.

Broad Implications for Narrow Studies: Aerosol-Water Interactions in the Atmosphere

The same challenges and questions of predicting atmospheric behavior and attributing sources of atmospheric aerosol that confront the IMPROVE program are also critical questions in assessing the broader roles aerosol play in climate and atmospheric chemistry. The measurements reported in each chapter are highly relevant to these important issues. Moreover, most research relating to these questions was done outside the narrow focus of the IMPROVE program. Each chapter discusses these impacts as well as the contribution each measurement set makes to the broader field of atmospheric science.

Study Locations and Seasons

Four IMPROVE related studies are reported in this dissertation, and one additional set of similar measurements from an independent project (see Table 1 for basic details). The first two IMPROVE studies were conducted on the boundary of Great Smoky Mountains National Park. The site location is shown in fig. 4, along with the basic source regions for air masses at the national park sites. The first took place during the summer of 2006 (20 July–30 August) and the second in the winter of 2007–2008 (1 November–10 February). These studies were conducted at the Look Rock Air Quality Station. Look Rock is in eastern Tennessee, situated on a ridge (~600 m) overlooking Great Smoky Mountains National Park (GRSM) to the south-east and rural farmland of the Tennessee River valley to the north-west. This site is approximately 30 miles south of Knoxville, TN. In addition to the measurements described here, the site houses both an IMPROVE station and an air quality station operated by the Tennessee

Valley Authority. It has been the location of several intensive IMPROVE studies including the Southeastern Aerosol Visibility Study (Day et al., 2001). The site is typical of the southeastern region of the US, known to possess high loading of sulfate aerosol resulting in significant degradation of visibility—though both have decreased significantly since 2006. As shown in fig.4, GRSM is not subject to a dominant flow pattern, particularly in the summer. In general, the areas north and west are more heavily developed, while areas south and east is dominated by deciduous forest.

Table 1: Study dates and locations.

	Abbr.	Study Dates	Site Location		Elev. (m)
Great Smoky Mountains NP	GRSM(S)	7/19/2006–8/17/2006	35.633°N	83.941°W	806
	GRSM(W)	1/11/2007–2/9/2008	""	""	""
Mt. Rainier NP	MORA	8/1/2009–8/30/2009	46.758°N	122.124°W	426
Acadia NP	ACAD	8/1/2011–8/30/2011	44.341°N	68.060°W	20
Storm Peak Laboratory	SPL	6/24/2010–7/28/2010	40.455°N	106.744°W	3214

The third study took place near the southeast border of Mount Rainier National Park (MORA) in the state of Washington (46.758°N, 122.124°W, 426 m asl) during the summer of 2009. The site was in a remote valley, surrounded by heavily-logged coniferous forest. MORA aerosol was highly variable, with sulfate levels dependent on the influence of the Seattle-Tacoma/Puget Sound region to the north-west. As indicated in fig. 4, this occurred regularly during the study, but not always. The final IMPROVE study, during the summer of 2011, was conducted on the Schoodic Peninsula in Maine, which lies west of Acadia National Park (ACAD) (44.341°N, 68.060°W, 20 m asl), across Bar Harbor. The coast of Maine near Acadia National Park is mostly rural, while

the interior is sparsely inhabited coniferous forest. Figure 4 indicates a prevailing northward flow during this project. As discussed in Chapter II, the aerosol at ACAD varied as the source region shifted onshore into more heavily developed parts of New England.

Finally, data from a fifth study, during the summer of 2010, at Storm Peak Lab (SPL) in remote northern Colorado is also reported in Chapter III. This study did not focus on the same set of IMPROVE assumptions as the four national park studies, but produced a similar set of measurements. More details are given in Chapter III.

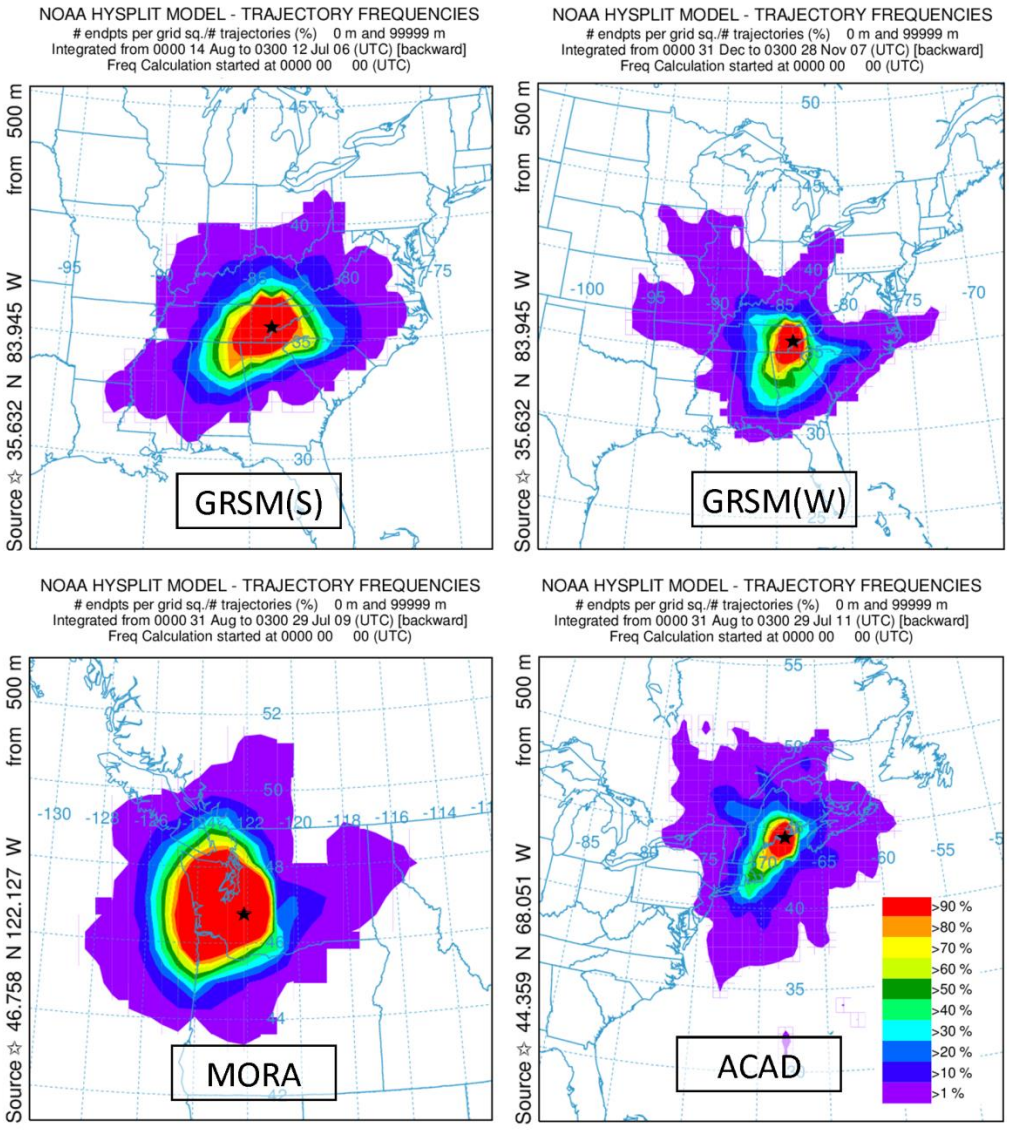

Figure 4: Density maps of 24-hr back trajectories during each study period. GDAS1 meteorological data used.

CHAPTER II

MEASUREMENT OF AMBIENT AEROSOL HYDRATION STATE AT FOUR US NATIONAL PARKS*

Introduction

This chapter presents results from four field deployments of a unique tandem differential mobility analyzer (TDMA) configuration with two primary capabilities: identifying alternative stable or meta-stable ambient aerosol hydration states associated with hysteresis in aerosol hydration behavior and determining the actual Ambient hydration State (AS-TDMA). This data set was the first to fully classify the ambient hydration state of aerosols despite recognition that hydration state significantly impacts the roles of aerosols in climate, visibility and heterogeneous chemistry. The AS-TDMA was installed at a site in eastern Tennessee on the border of Great Smoky Mountains (GRSM) National Park for projects during the summer of 2006 and winter of 2007–2008, and at Mt. Rainier (MORA) and Acadia (ACAD) National Parks during the summers of 2009 and 2011. During all studies, some of the aerosols sampled in continuous AS-TDMA measurements were found to possess two possible hydration states under ambient conditions (ranging from 4% at ACAD to 53% at GRSM in winter). In every case at GRSM(S), MORA, and ACAD, the more hydrated of the possible states was occupied. Only during GRSM(W) were both hydration stated detected, with 65 %

* Parts of this chapter are adapted, with permission, from "Measurement of ambient aerosol hydration state at Great Smoky Mountains National Park in the southeastern United States," by N.F. Taylor, D.R. Collins, C.W. Spencer, D.H. Lowenthal, B. Zielinska, V. Samburova, and N. Kumar, originally published in *Atmospheric Chemistry and Physics* in 2011 (Vol. 11, pp. 12085-12107). The article is fully available for re-use under the Creative Commons 3.0 license.

of ‘hysteretic’ aerosol in the more hydrated state; 35 % in the less hydrated state. This chapter explores how these findings are related to differences in the fine particulate (PM 2.5) composition, ambient RH as measured during the studies periods, and atmospheric conditions.

Background

Atmospheric particulates frequently exhibit transitions between solid and aqueous phases driven by changes in relative humidity. Often, these changes in hydration state are irreversible and display hysteresis due to kinetic limitations on the formation of ordered phases (Tang and Munkelwitz, 1984). For example, ammonium sulfate deliquesces at ~ 80 % RH but effloresces at ~ 40 % RH. Between these critical relative humidities, the RH domain of hysteresis, an ammonium sulfate aerosol may occupy one of two hydration states, meta-stable and supersaturated solution or anhydrous crystal, dependent on its RH history. This behavior is illustrated in Fig. 5, which depicts change in particle diameter due to water uptake for an initially crystalline ammonium sulfate aerosol and water loss for an initially aqueous, solution aerosol.

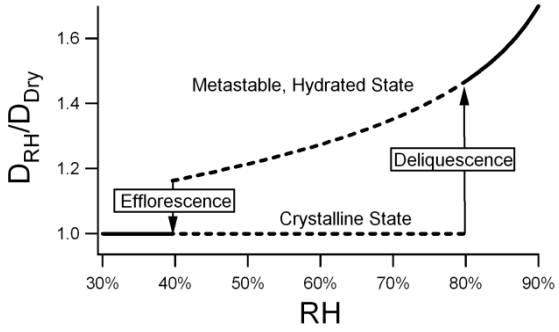

Figure 5: Idealized ammonium sulfate growth curve.

Similar to the idealized ammonium sulfate aerosol, ambient boundary layer aerosol have been observed to display occasional hysteresis at a variety of locations by nephelometry (Brink et al., 1996; Carrico et al., 2000, 2003; Charlson et al., 1974; Day and Malm, 2001; Dougle et al., 1998; Rood et al., 1987; Shaw and Rood, 1990; Swietlicki et al., 2000; Wang et al., 2007) and Tandem Differential Mobility Analyzer (TDMA) measurements (Berg et al., 1998; Gasparini et al., 2006). Hysteresis is not a universal characteristic of ambient aerosol and not consistently detected (Fierz-Schmidhauser et al., 2010; Pitchford and McMurry, 1994; Rissler et al., 2006; Sjogren et al., 2008; Zhou et al., 2001). This is anticipated by laboratory studies of hysteretic aerosol components. In particular, the hydration behavior of sulfate/nitrate/ammonium/proton (SNA) mixtures has been well established and is marked by decreasing critical relative humidities of deliquescence (DRH) and efflorescence (ERH) with increasing acidity (Martin, 2000). When no ammonium is present, these mixtures display continuous hygroscopic growth and exhibit no phase transitions. Further, in situ measurements of hysteresis often report truncated hysteresis loops and gradual phase transitions with partial hydration of the lower hydration state (Berg et al., 1998). This, too, is consistent with laboratory studies of various internal mixtures of both inorganic and organic species whose findings indicate complex interactions affecting the RH and character of phase transitions (Brooks et al., 2002; Ciobanu et al., 2010; Hansson et al., 1998; Martin et al., 2001; Tang et al., 1978).

As aerosol properties may differ greatly between hydration states, knowledge of hydration state of ambient aerosols is critical to understanding their atmospheric roles. In

the common case of ammonium sulfate, a meta-stable, aqueous aerosol near the deliquescence RH may feature over 3 times the volume and light scattering per solute mass of the alternative crystalline state. This greatly affects the influence of ammonium sulfate on the global radiation budget as well as local visibility. An expansive treatment of the radiative effects of SNA hysteresis globally was done by Martin et al. (2004) with follow up by Wang et al. (2008a). These studies utilized global 3-D chemical transport models to predict SNA loading, degree of neutralization, extent of hysteresis, and the effect on the global radiation budget of assuming the least hydrated and most hydrated aerosol hydration states. The first of these studies made no attempt to predict the hydration state, but only compared the result of each assumption. They concluded that an assumption of the lower hydration state would produce a 25 % reduction in negative radiative forcing estimate for global SNA versus an assumed aqueous hydration state. The second work, by Wang et al. (2008a), augmented a similar methodology to include model based prediction of hydration state. Unfortunately, it is difficult to gauge the accuracy of this and other modeling approaches (Colberg et al., 2003; Grant et al., 1999; Haywood et al., 1997; Wang et al., 2008b) as limited measurements have been made fully characterizing ambient aerosol hydration state apart from the work of Santarpia et al. (2004) – the precursor to the present endeavor (Swietlicki et al., 2008).

Other current approaches to measuring hydration state are the nephelometry based work of Rood et al. (1987, 1989), the 1 × 3 TDMA of Martin et al. (2008) and Rosenoern et al. (2009), and the Dry-Ambient Aerosol Size Spectrometer (DAASS) (Engelhart et al., 2011a; Khlystov et al., 2005; Stanier et al., 2004). From the high time

resolution of nephelometry to the broad size range examined by the DAASS to the notable sensitivity of the 1 × 3 TDMA, each has various advantages. However, when considering the alternative hydration states resulting from hysteresis these approaches have less merit. The work of Rood et al. (1987, 1989) only positively indicates the presence of a more hydrated alternative state, while the DAASS does not treat hysteresis. Both could, with sufficient supporting measurements of hysteresis behavior or composition, more fully address alternative hydration states; but this is not inherent in their function. Further, though these instruments do in some fashion retrieve size dependence, it is not with the clarity, resolution, or ability to determine mixing characteristics available to TDMA based systems. Alternatively, the 1 × 3 TDMA has advantages of sensitivity as well as the capability to indicate hysteresis and the ambient hydration state. But this capability has yet to be exploited in field deployments.

The present study develops the methodology of Santarpia et al. (2004), which augmented and modified the conditioning process used by Rood et al. (1987, 1989) to positively determine the existence of both aerosol in a more hydrated, meta-stable state and aerosol in a less hydrated state. This system, termed an Ambient State (AS)-TDMA, takes full advantage of the high resolution and size resolving operation available to TDMA based instruments. A description of the operation and configuration of the AS-TDMA occupies first portion of this manuscript. Further details on the analysis of its unique results are given as an appendix. The second and greater part of this Chapter reports the findings from field deployments of the AS-TDMA.

Methodology

The measurement of ambient hydration state was achieved with a three part experimental process utilizing a modified TDMA. The technique is elaborated here as follows: first, the AS-TDMA instrument is described, especially as it deviates from the conventional TDMA configuration. Next, the configuration is translated into operation and the experimental procedure for the determination of hydration state. Meta-experimental parameters such as measurement frequency are discussed following the operation illustration. Finally, the procedures used to refine the AS-TDMA results are introduced, though their detailed discussion is deferred to Appendix A.

AS-TDMA Instrumentation

The AS-TDMA shares operational principles of TDMA systems: determining the effects on particle size of some process such as heating or humidifying. To measure hydration state, the AS-TDMA retrieves the different effects on the size of an ambient aerosol of three distinct processes: a Deliquescence Forcing (DF), an Efflorescence Forcing (EF) and a Drying process. The modifications necessary to execute these processes on an ambient aerosol are significant but do not involve alterations of the essential TDMA elements. A very brief review of several salient features of TDMAs is included in this section. Further, while the components and configuration involved in the modification are described, no corresponding description is given for the non-unique portions of the AS-TDMA instrument. For details both on TDMA concepts and the specific components, operation, performance and control of the TDMA system modified to form the AS-TDMA, the reader is referred to Gasparini et al. (2004).

All TDMA systems rely on two electrostatic classifiers, often called DMAs, which each acts as a controllable "bandpass" filter on particle electrical mobility. While mobility is determined by both size and morphology, it is convenient to refer to mobility in terms of that of a sphere. Thus, in this paper all mention of size with respect to TDMAs refers to the size of a sphere of equivalent mobility. TDMA utilize the two classifiers in series. The first classifier is controlled to transmit an ensemble of particles with fixed, constant diameter from the aerosol being sampled. The resultant, roughly monodisperse aerosol is then subject to a process (e.g. humidification, heating) that could modify the size of the particles. This creates a particle ensemble in which size reflects responsiveness to the inter-classifier process (e.g. hygroscopicity, volatility). This final size distribution is captured by the second classifier, operating in a scanning configuration, in conjunction with a condensation particle counter (CPC). The count rates recorded by the CPC are inverted to retrieve the size distribution.

There are two primary features of the AS-TDMA modification: the first electrostatic classifier is operated to preserve ambient RH and temperature and a series of three measurements with different inter-classifier RH conditioning processes are employed. This section describes the implementation of these features and their utility in retrieving ambient hydration state. A schematic of the implementation is provided at the top of Fig. 6.

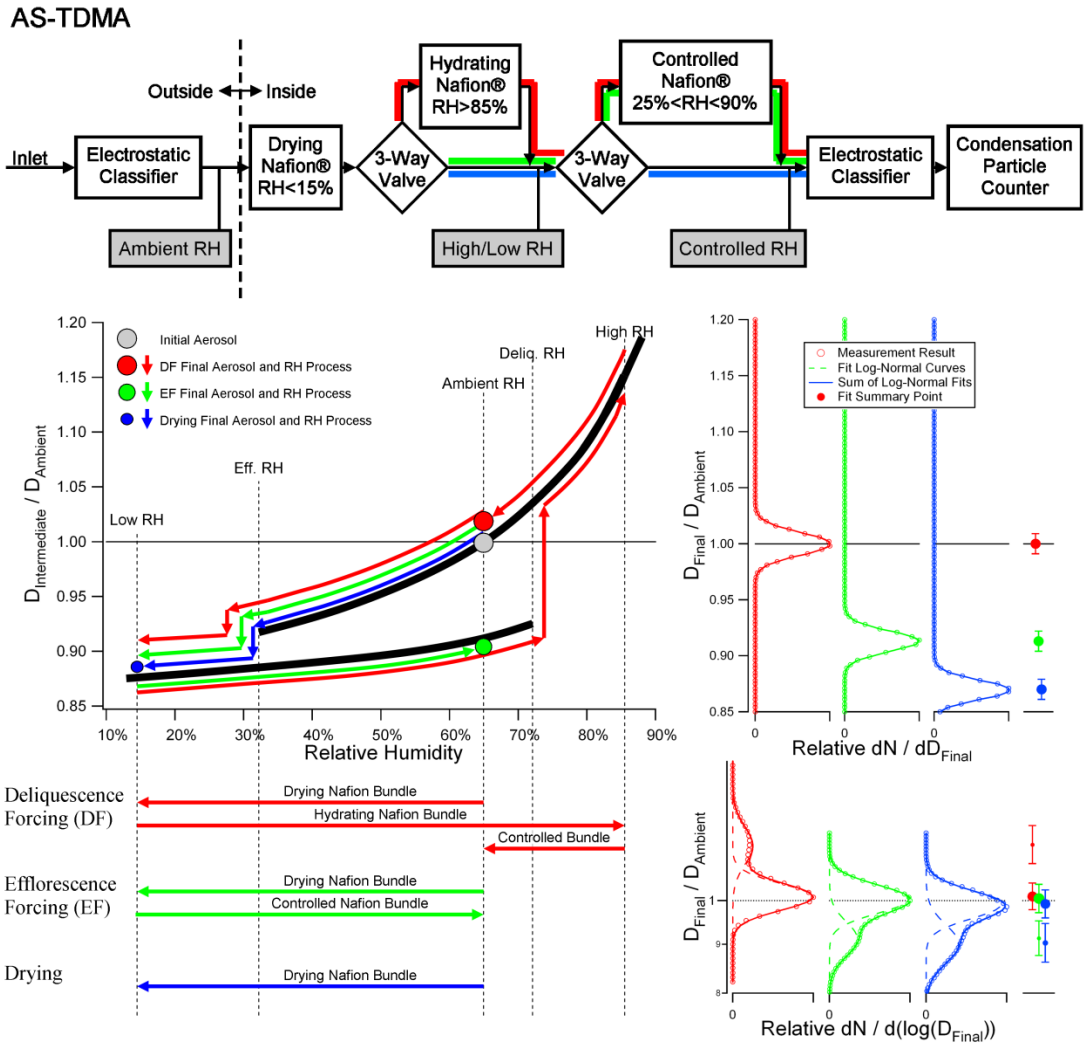

Figure 6: AS-TDMA schematic and experimental procedure illustration. The configuration and results for the DF, EF and Drying process are shown in red, green and blue, respectively. The grey elements of the schematic represent RH Probes. The procedure illustration depicts AS-TDMA operation on a hypothetical aerosol found in a more hydrated state at 65% RH. Its hydration characteristics are illustrated in the upper-left chart. The arrows in the upper left and lower left depict the manipulations of RH achieved in the Nafion tube bundles. The resultant size distributions produced by the process measurements are shown in upper-right corner. In the lower-right, an example taken from the winter study period is displayed. Shown along the right edge is a compact convention for displaying the results.

As illustrated in the schematic, the first classifier is located in the ambient environment. In addition, care is taken to ensure that it operates at ambient RH and

temperature to remove perturbations in ambient conditions before the aerosol has been transmitted through the classifier column. The goal is to select a monodisperse aerosol based on ambient size and especially ambient hydration state. This is a significant difference from common TDMA and is necessary to obtain information about the ambient condition of the aerosol. For this study, the external unit was located on the roof of the climate controlled trailer housing the remaining instrumentation. The unit is shrouded with a heavy, white cover to guard against weather and direct solar heating. In addition, a high volume fan circulates ambient air rapidly around the instrument components to enhance temperature equilibration. The ambient aerosol is sampled with a simple inlet and passes through a Po-210 based neutralizer before entering the first classifier. Immediately downstream of the classifier a Vaisala HMM-22D RH probe, also maintained at ambient conditions, captures the RH of the aerosol sample flow. This, the "Ambient RH" probe, and other Vaisala RH probes are shown in grey in the schematic. At this point the aerosol is directed inside and into a temperature controlled enclosure (29 ◦ C) in order to facilitate the stable manipulations of RH that constitute the inter-classifier processes. This admits the possibility of some volatilization of compounds such as ammonium nitrate; yet, hopefully with limited impact on the results (this is discussed in the first part of the results section below, on the impact of ammonium nitrate volatilization on hydration behavior, and in the fourth part of the appendix for the recovery of systematic mass loss).

The middle portion of the schematic describes the three alternate configurations that achieve the three inter-classifier processes used to resolve ambient hydration states.

The individual processes will be referred to as the Deliquescence Forcing (DF) process, the Efflorescence Forcing (EF) process and the Drying process. They are depicted in red, green and blue, respectively, in the schematic and in the balance of the Chapter.

Each of the processes consists of a different sequence of RH manipulation conducted using variously configured Perma Pure Nafion PD-07018T moisture exchange tube bundles. The first, moving from left to right in the schematic, is configured to dry the aerosol with its purge flow held at high vacuum. The "High/Low RH" probe measures the extent of drying by this Nafion bundle during the EF and Drying processes. Drying varied narrowly during these studies and the RH of the aerosol sample flow exiting this exchange was consistently between 8 and 15 % RH. The second moisture exchange is configured to hydrate the aerosol sample flow by maintaining very high RH (> 95 %) in the purge flow. It achieved consistent sample flow humidification to > 85 % RH, measured by the "High/Low RH" probe during DF measurements. The final Nafion bundle is configured to be controllable. The purge flow contains a high mixing ratio of water, but the purge pressure (vacuum) is controllable. This allows the vapor pressure differential to vary and with it the moisture flux between the purge and sample flow. The "Controlled RH" probe measures the RH of the sample flow exiting this exchange. The RH produced by this Nafion bundle is controlled to mirror the ambient RH measured by the "Ambient RH" probe using a tuned PID (proportional/integral/derivative) routine. Typical displays of its performance are included in Figs. 8 and 9 in the results section, where the average retrieved Ambient RH

and Controlled RH values for a series of measurements are shown. The averages depicted are for 180 s intervals corresponding to the duration of a single measurement.

The three different inter-classifier processes are produced by a series of 3-way valves that determine which Nafion bundles the sample flow is directed through. Each of the processes begins with the initial drying Nafion bundle. This drying bundle is placed immediately within the housing trailer. Apart from its role in the processes, it serves to prevent condensation in the tubing segment exposed to the low (air-conditioned) temperature in the trailer that conducts the aerosol into the internal and finely-temperature-controlled instrument enclosure. From this point, the RH manipulations of the processes diverge. The path followed during the DF process is shown in red. It conditions the aerosol to a high RH and then restores the RH to the ambient level. This process is intended to resolve the presence of ambient particles exhibiting hysteresis and occupying a less hydrated state. The EF process, shown in green, only returns the dried sample flow to its ambient RH. The EF process resolves the presence of particles in a more hydrated state. The Drying process, shown in blue, leaves the aerosol sample flow at low RH. This produces a final aerosol stream in which particle size reduction from the size selected by the first classifier reflects the amount of water initially present in the particles.

The remainder of the AS-TDMA is configured in the standard fashion to retrieve the resultant size distributions of each process. Beyond the two primary modifications here discussed, the AS-TDMA differs from the Gasparini et al. (2004) TDMA cited above in only two other significant aspects. In conventional H-TDMAs, to maximize

separation of size distribution modes comprised of populations of particles having similar hygroscopicities, the inter-classifier RH is typically maintained at around 90 %. In contrast, the effective RH in the AS-TDMA is not prescribed and ranged from 40 to 90 % for the measurements reported here. To partially compensate for the resulting compression of size modes, a higher than usual 13:1 sheath to aerosol flow ratio was employed in the DMAs. Further, the CPC in the AS-TDMA was a TSI model 3762 capable of handling higher sample flow rates and producing better counting statistics than that used by Gasparini, et al. (2004) As a final note on configuration, higher count rates achieved through the use of high flow DMAs (HF-DMAs; Stolzenburg et al., 1998) in both the AS- and Gasparini TDMA also aided production of narrow modes that were more easily identified and isolated.

AS-TDMA Experimental Process and Operation

The following illustration describes the operation of the ASTDMA on a hypothetical aerosol with given hydration characteristics; explicitly covering the effects on the aerosol sample flow as it is transmitted through the three processes as well as the form and type of result each process generates. In addition, consideration is given to what response departures from the hypothetical aerosol would produce in the results to fully establish how AS-TDMA experimental processes resolve hydration state. This subsection concludes with experimental data such as measurement frequency and size.

The following descriptions refer especially to the portion of Fig. 6 below the instrument schematic, which variously depicts the application of the three processes to an ideal, internally mixed aerosol. The particles in this ensemble have the hydration

characteristics illustrated in the upper left: an efflorescence RH of 34 % and a deliquescence RH of 72 %. The abscissa describes the ratio of the diameter of the particles to the initial, ambient diameter selected by the first classifier. The aerosol is depicted as initially in its most hydrated state at an ambient RH of 65 %. This is illustrated by the large grey dot at the intersection of the ambient RH and unity size ratio lines. The arrows below this chart describe the RH to which the aerosol particles are exposed during each of the three processes. The corresponding response in the size of the aerosol particles is traced along the hydration profile above. In the upper right, the resultant normalized size distribution produced by each process is shown, reflecting the distributed response of the instrument to an ensemble of uniform, internally mixed particles. A set of measurements made during this study is shown in the lower right to illustrate several analysis steps. Shown along the right margin are symbols illustrating a compact method of describing the size distributions.

Each of the three processes begins with an approximately monodisperse aerosol stream supplied by the first classifier. This stream is directed into the indoor portion of the instrument and passed through the drying Nafion bundle, as indicated in the instrument schematic. As the monodisperse aerosol passes through this Nafion, the RH of the carrier gas decreases to a low RH ($\sim$ 15 %) and most of the particulate water evaporates. This is depicted in the upper left hand portion of the illustration by the three parallel sets of arrows that trace the growth curve away from the initial ambient size and RH, the point marked by a grey dot, downward and to the left. In the lower left portion of the illustration, the first arrow in each color depicts the change in RH and is labeled

"Drying Nafion Bundle" to relate what element in the instrumentation effects the change. For the hypothetical aerosol, this transition includes the efflorescence of the aerosol. As the hypothetical aerosol is dried to levels below its efflorescence point, the illustration depicts it losing additional water. The aerosol size at this point reflects how much water it initially contained. If the aerosol had initially been in its least hydrated state, the reduction in size would have been less dramatic. If the initial monodisperse aerosol had contained an external mixture of particles containing different amounts of water, it would become polydisperse with drying. At this point, the three processes diverge and the now dry aerosol stream is diverted according to each program of RH manipulation producing the following results: –

Deliquescence Forcing (DF): this process follows the path in the schematic and the illustrated features shown in red. It resolves the presence of ambient, hysteretic aerosol in less hydrated states. During this process, the aerosol stream is diverted by the first 3-way valve into the hydrating Nafion bundle. This increases the RH of the aerosol to at least 85 %. The effect on the illustrated aerosol is traced by the red arrows away from the low RH and small particle size, along the least hydrated branch of the growth curve until the aerosol particles deliquesce at 72 % RH. At RH levels above the deliquescence point, only one hydration state exists and the aerosol particles continue to take up water until high RH (> 85 %) is achieved. Because this RH is above the deliquescence point, the effects of the initial drying and efflorescence are removed. Next, the aerosol enters the controlled Nafion tube bundle, which is configured to restore

ambient RH levels. Thus, the final red arrow in the process depicts the aerosol being restored to ambient RH. This causes the aerosol particles to lose water as they are exposed to decreasing RH. As is depicted in the upper right, the aerosol is restored to its initial condition and its particles to their initial size. The resultant size distribution recorded is shown to the right. It is centered at a unity ratio of final to initial size. The breadth of the distribution reflects the actual range of sizes in the approximately monodisperse aerosol transmitted by the first classifier. If the particles had instead been initially in their least hydrated state, the RH manipulations in this process would have forced them to deliquesce, leaving the particles larger and in their most hydrated state. If the aerosol did not exhibit hysteresis this process would not alter it. Finally, if the aerosol was externally mixed, the resultant size distributions from this and the other processes would contain, superimposed, the responses of the different factions in the aerosol. For example, the results in the lower left depict an external mixture with several distinct populations.

Efflorescence Forcing (EF): this process follows the green path through the instrument and resolves the presence of hysteretic ambient aerosol in a more hydrated state. During this process, the aerosol bypasses the hydrating Nafion bundle. The controlled Nafion is again operated to mirror the ambient RH. As traced on the growth curve, the result of this process is to move the aerosol from its most hydrated state to its less hydrated state, forcing its efflorescence. If the aerosol had been initially in the less hydrated state, or if it did not exhibit

hysteretic phase transitions, there would be no change in the size of its particles. For the case illustrated, the reduction in size is shown in the resultant size distribution on the right. –

Drying: in this final process the blue path is followed and both the hydrating and controlled Nafion are bypassed. This preserves the dry state of the aerosol. The growth curve depicts a reduction in size greater for this process than that caused by the EF process. This results in the size distribution being centered about a lower ratio of final to initial diameter than for the EF process. If the aerosol had been initially in its least hydrated state then the decrease in size would be reduced. If the aerosol did not display hysteretic phase changes, the aerosol would still display water loss, dependent on the aerosol hygroscopicity.

From this illustration, the purpose and use of each process should be mostly apparent: the growth of aerosol particles caused by the DF process implies that the aerosol is hysteretic and in a less hydrated state initially. Similarly, a reduction in aerosol particle size caused by the EF process indicates that the aerosol is hysteretic and in a more hydrated state initially. The Drying process resolves the ambient water content of aerosols, the use of which is elaborated in the next subsection. The comparative moreor less-hydrated state will be used henceforth to reference hysteretic aerosol hydration states detected by the EF and DF processes, respectively. This convention is used in deference to the plausibility of intermediate hydration states and multiple crystalline forms (Mifflin et al., 2009; Rosenoern et al., 2008). Further, this reserves the possibility of water content in less hydrated states.

During these studies, each of the three process measurements was conducted for five ambient sizes: 0.025, 0.05, 0.1, 0.2, and 0.4 μm. In operation, a measurement for every size was conducted using each process before transition to the next. The DF process was conducted first, the EF second and the Drying process last. The time resolution of these measurements varied based on the length of each individual measurement, which was varied between 3 and 5 min, as CPC count rates allowed. An additional 100 s was required between each size measured for the change in size selected by the first classifier to penetrate and achieve steady state in the remainder of the instrument. The transitions between the processes required a period of equilibration as the controlled Nafion bundle adjusted to changes in the RH of the sample flow and for changes in RH to permeate the second classifier. It was determined that 300 s was sufficient for the transitions from DF to EF and from EF to Drying processes. For the transition from Drying to DF process, to begin the next measurement sequence, 900 s was required. In sum, each full measurement cycle took 120–150 min.

Measurements were continuously conducted at this frequency except when instrument limitations forced temporary suspension of operation. These limitations were threefold. First, to avoid condensation within the external classifier column, measurements were suspended when ambient RH was higher than ~90 %. Second, the controlled Nafion bundle produced a minimum RH of approximately 25–30 %. Therefore measurements were also suspended below that threshold. Finally, to avoid frost build up, measurements were suspended, the circulation fan in the external unit was switched off and a small heater was powered on when ambient temperature fell below 0

◦ C. The effect of these limitations on measurement coverage is illustrated in Fig. 7. The most common cause for measurement suspension was high RH and a corresponding depression in measurement frequency at night is evident in the charts for all studies.

AS-TDMA Data Treatment

AS-TDMA results take the form of size distributions, as illustrated on the right side of Fig. 6. While this form is adequate for simple evaluations, additional procedures were applied to refine the results and to facilitate more complicated analysis. These are detailed in the elements of Appendix A titled Log-Normal Curve Fits, Mode Correlation, Hygroscopic Growth Model Use, and Qualification of Hysteresis and Scan Offset. Two final elements cover the treatment of multiply charged particles and AS-TDMA calibration. The following distillation introduces the essential concepts from these processes.

All subsequent presentations of AS-TDMA findings rely on the characterization of the resultant size distributions as a sum of weighted log-normal probability distributions. This is intended to isolate and succinctly describe distinct fractions or modes in the distribution. These log-normal characterizations are depicted in this work as shown at the far right in Fig. 6: each mode isolated by a log-normal distribution is depicted as a single symbol. The size of the circular portion reflects the fraction (by number concentration) of the total size distribution accounted for by the individual log-normal curve. The vertical position of the symbol indicates geometric mean diameter (or size ratio). Lastly, the length of the error bars indicates the breadth of the mode and is

one geometric standard deviation. In the lower right, an application of this technique to a set of results from this study is illustrated.

The remaining major elements of Appendix A describe the procedures used to refine the AS-TDMA findings. Mode Correlation describes the essential process of relating the results from the three different inter-DMA processes. Hygroscopic Growth Model Use covers methods of retrieving errors introduced by occasionally fraught RH control. Also, a use for normalizing results under RH (similar to GF 90%) is described. Finally, Qualification of Hysteresis and Scan Offset establishes flexible methods for determining whether a set of measurements indicates the presence of hysteresis. This qualification is then justified as a means for correcting otherwise irretrievable measurement errors.

GRSM Results and Discussion

This section is broken into three parts. The first contains ancillary descriptions of the study periods including relative humidity and temperature, fine particulate (PM2.5) composition from diel filter based measurements, and H-TDMA results. The two remaining parts present the AS-TDMA results; first as case studies and individual measurements and subsequently as various study length summaries.

Seasonal Characterizations and Ancillary Results

The strongest feature in the AS-TDMA results is the contrast between the two study periods. During the summer campaign (20 July–30 August 2006) 12 % of AS-TDMA measurements indicated ambient aerosol in a more hydrated state, while no measurements indicated ambient aerosol in a less hydrated state and the balance of

measurements showed no hysteresis. The winter campaign (1 November 2007– 10 February 2008) measurements indicated 32 % and 17 % of sampled particles to be in more and less hydrated states, respectively. Moreover, the seasonal contrast is well supported by the differences between the PM 2.5 composition and ambient RH measured during the two study periods. Thus, the comparison of the seasonal results is a consistent element in the presentation of these findings. In this subsection, the salient contrasts in the seasonal conditions evident in the ancillary material are highlighted. This is followed by a brief summary of H-TDMA measurements as they support ASTDMA findings.

Seasonal characterizations

The diurnal variation of RH and temperature during each GRSM study period is shown in Fig. 7. RH is a primary factor in both the appearance of hysteresis and in determining hydration state. Temperature does modulate the RH for phase transitions but is a factor secondary to composition. Additionally, though not treated in this paper, the temperature depictions suggest heating rates and boundary layer dynamics that influence RH history of surface aerosol. The summer period was characterized by a consistent diurnal pattern of warming and drying through the morning and cooling and humidifying through the evenings. Very low levels of RH were infrequently reached, which contributed to the dearth of observed less hydrated ambient states. The winter RH values varied widely. The RH did reach lower levels than during the summer, partially explaining the increased observance of aerosol in less hydrated states. The lack of a consistent diurnal cycle during the winter is also evident in Fig. 7.

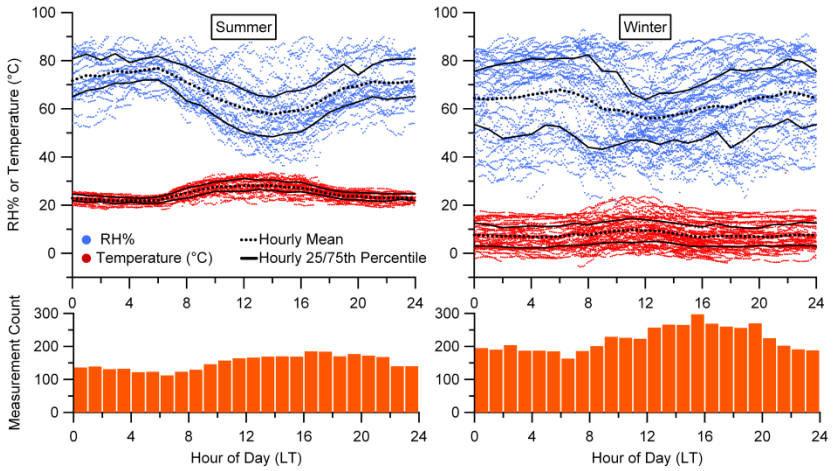

Figure 7: GRSM diurnal temperature, RH and AS-TDMA measurement frequency. Each colored point in the RH and temperature plots is the average value during a single EF, DF or Drying process measurement. A point exists for every measurement during each study. The cessation of operation beyond certain RH and T limits discussed at the end of Section 2.2 produces corresponding artifacts, e.g., few RH points above 90%. The bottom charts show the diurnal measurement frequency, counting each size distribution recorded.

Along with RH history, the critical RH levels for irreversible phase transitions determine hydration state. These levels are primarily driven by particulate composition with secondary influences from morphology and temperature. During month-long intensive portions of each study period, daily filter based PM 2.5 composition measurements were made (Lowenthal et al., 2009). As with seasonal variation in meteorological conditions, the composition of fine aerosol was quite different between the two studies. The results are shown in Fig. 8 together with the expected annual variation derived from measurements made at the on-site IMPROVE network facility and the expected RH levels for complete deliquescence of a solid composed of sulfate, nitrate and ammonium in the proportions determined by the measurements.

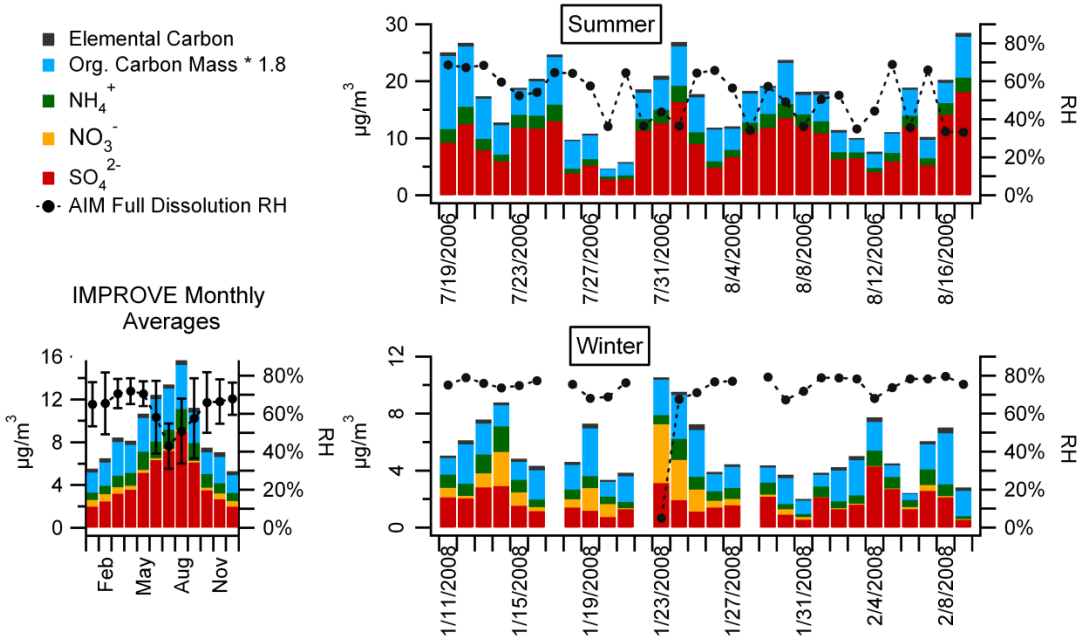

Figure 8: Daily PM 2.5 Filter based measurements made on site at Look Rock near Great Smoky Mountains National Park from Lowenthal, et al. (2009) and the IMPROVE network. IMPROVE values are computed as the average of all days within each month during the period from 1997-2006 in which NH_4^+ ions were measured. The black traces showing expected full dissolution RH were calculated for the measured sulfate/nitrate/ammonium proportions using the Aerosol Inorganics Model (AIM).

The estimation of the RH levels necessary for full dissolution was made using the Aerosol Inorganics Model (AIM) (Clegg et al., 1998a, b, 2001; Clegg and Brimblecombe, 2005). These estimations are intended to aid in interpreting the seasonal composition variation. The calculations neglect surface tension and assumed a temperature of 298.15 K. Also, only the sulfate, nitrate and ammonium fractions were considered. While the neglect of the measured organic components was primarily motivated by a practical lack of thermodynamic data, the effect of heterogeneities in the quantities measured on deliquescence RH is generally a reduction of less than 10 % RH (Brooks et al., 2002; Choi and Chan, 2002), often much less (Cruz and Pandis, 2000;

Hansson et al., 1998; Smith et al., 2011). Exceptions can be found in the work of Marcolli et al. (2004), though these occur with organic aerosol fractions significantly larger than indicated by the filter measurements in consideration. Consequently, these dissolution values are reasonable first order approximations. Beyond these limitations, filter measurements produce results integrated over the sub-2.5 μm size range and 24 h time periods. Their relationship to highly size and time resolved AS-TDMA results is accordingly loose.

Filter based measurements are also fraught with volatilization issues, especially of ammonium. However, the sensitivity of dissolution behavior predicted by AIM to the volatilization of ammonium is quite moderate. This claim is based on the supposition that the ammonium lost is associated with nitrate and that the locally ubiquitous sulfate fraction of any aerosol particle containing ammonium nitrate is fully neutralized (Seinfeld and Pandis, 2006). Thus, it is expected that the winter dissolution estimations were only moderately, artificially high.

Bearing these reservations in mind, broad seasonal differences are persistent. The summer, characterized by high sulfate loading and insufficient ammonium for neutralization, has lower expected full dissolution RH levels. The winter samples were generally neutralized with accordingly high dissolution RH estimations. This difference follows the seasonal trend illustrated in the earlier IMPROVE dataset. The IMPROVE results shown were taken during the period from 1997 to 2006 in which ammonium was included in the filter analysis. These results show a yearly cycle in which peaks in sulfate and nitrate correspond to depressions in expected dissolution thresholds. It is this

seasonal variation in the location of the full dissolution RH along with the seasonal change in ambient RH conditions that likely produced the more frequent detection of hysteretic aerosol during the winter measurement periods than the summer. The correlation between filter results and hysteresis detection is explored more fully in the final GRSM AS-TDMA results subsection.

GRSM TDMA results

An H-TDMA was operated during both GRSM campaigns. During the summer campaign, measurements were intermittent due to instrumentation issues. The winter operation was less fraught and more generally useful. In Fig. 9, an H-TDMA RH scan from each project is shown along with a summary of the phase transition findings from the winter campaign. The two example scans are sufficiently typical and highlight the amount of water operative in AS-TDMA measurements. Fifty-six full RH scans for each size (0.05 and 0.2 μm) were conducted during the winter. The frequency plot indicates the fraction of these with the given phase transition RH. While knowledge of phase transition RH is an essential element in relating atmospheric conditions to local hydration state, in the present work these results primarily serve to indicate common RH levels for phase transition during the study and thus reinforce AS-TDMA results. The discrepancy between the observed deliquescence point and that predicted from composition (Fig. 8) is reasonable given loose correlation between filter and TDMA based measurements. Finally, the H-TDMA phase transitions compare well with the average winter deliquescence RH roughly indicated by the AS-TDMA results as shown in Fig. 16 and surrounding discussion.

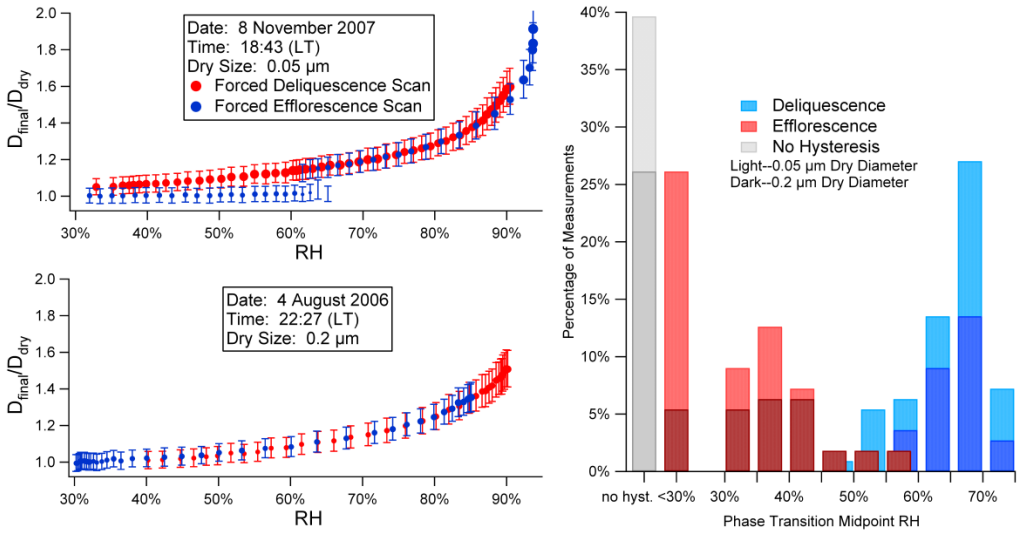

Figure 9: H-TDMA example scans and GRSM winter H-TDMA detected phase transition summary. Whiskers in the example RH scans indicate the breadth (± 1 std. deviation) of the particle distribution for each measurement.

Individual Measurements: Full Cycle Sets and Time Series

This first section of GRSM AS-TDMA findings contains depictions of individual measurements in two arrangements: single full measurement cycles of all sizes and processes, and in sequence as time series. These serve as case studies, depicting typical phenomena from the two studies. The measurement cycle depictions primarily feature size-dependent hydration characteristics while the time series illustrate transitions in hydration behavior driven by changing ambient RH.

Individual measurement sets

The results of three full measurement cycles from both the summer and winter study periods are shown in Figs. 10 and 11. Each full cycle contains 15 measurements: one for each of the five sizes measured during each process. The plots utilize the scheme for depicting these distributions introduced above and illustrated to the far right in Fig. 6.

Here, five such depictions, corresponding to the five ambient sizes considered, are arrayed side-by-side: the ambient diameter is the abscissa.

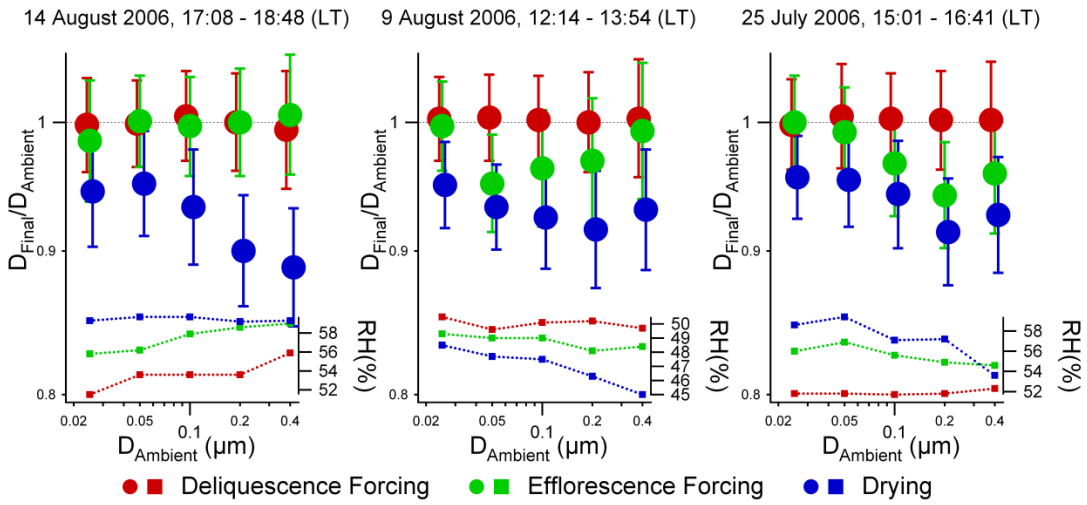

Figure 10: The results of three AS-TDMA full measurement cycles from the GRSM summer campaign. The point and error bar markers follow the convention described in the methods section: Each point characterizes a mode in the size distribution. The size of the point reflects the relative contribution of the mode to the concentration of particles having that ambient diameter; the vertical position depicts the characteristic ratio of post-process to ambient size of particles in the mode; and the error bars describe the breadth of the mode. Below the measurement results is the ambient RH during each measurement. The slight lateral offset between the results from each process is artificial and for clarity only.

Figure 10 shows three measurement cycles from the GRSM summer study period. The first of these depicts no hysteresis, evidenced by the near unity size ratio of the results from the DF and EF process measurements. The slight departures from unity are typical of the noise level in most of the measurements. The remaining two plots depict hysteresis for some of the ambient sizes, shown by less than unity size ratios (i.e. water loss) in the EF results. In these two plots, the portion of particulate water involved in hysteresis varies with size, with an apparent maximum inside the set of sizes measured. It is also interesting that not all of the water in the particles is lost in the EF

process, illustrated by the greater water loss in the Drying measurements than in the EF measurements. This is a typical summer feature and is revisited in the study summaries of the next subsection.

Summer results were highly regular and these three results typify that study well. As noted above, no summer measurements detected less hydrated, hysteretic aerosol. Approximately 31 % of the 318 full measurement cycles recorded during the summer included a more hydrated, hysteretic fraction at some size. Of these, 81 % displayed a variation of hysteretic water with particle size similar to that shown in the second and third plots, though the location of the apparent maximum varied. In addition, 90 % of the cycles showed increasing hygroscopicity with size.

The persistent variation of water retained in the less hydrated state with size is worth consideration. Due to limited supporting data, no conclusions can be drawn; however, the following plausible hypotheses have been suggested: a reduction in hysteretic water occurs selectively for larger sizes activated as cloud condensation nuclei, driven by the rapid addition of sulfate in cloud processing. This increases the acidity of particles, reduces the deliquescence RH, and increases the likelihood of partial and stepwise dissolution of solids. The lack of hysteresis in the small sizes is caused by mechanisms driving the growth of nucleation mode aerosol such as the addition of secondary organic mass. This is supported by the generally lower hygroscopicity indicated by the Drying process for smaller sizes.

The winter results showed greater variety as illustrated in the three plots in Fig. 11. The 0.1, 0.2 and 0.4 μm ambient size results in the first plot depict two populations,

one hysteretic and more hydrated and one containing little or no water. With the smaller sizes, it is possible that the single EF and Drying process modes contain two convoluted modes – illustrating the resolution limits of the AS-TDMA and challenges in fitting data. It is notable that the EF and Drying process results for the larger sizes are almost identical, which implies that there is little residual water in the less hydrated form of the hysteretic population. The second plot depicts an aerosol in which all of the sizes measured contain a population of less hydrated, hysteretic aerosol. For most of the sizes, there is also a fraction of more hydrated, hysteretic aerosol. In addition, there appears to be a fraction of non-hysteretic aerosol, implied by comparisons between the hysteretic mode of the DF (or EF) results and the near unity mode in the results of the EF (or DF) that contains its aerosol fraction. A residual non-hysteretic fraction is inferred because the number concentration (the size of the point) of the hysteretic mode does not fully account for the complementary non-hysteretic mode. A lack of certainty rises from the time separation between the measurements. The final plot illustrates a case in which only a less hydrated, hysteretic fraction exists in the larger sizes. In this case, there appears to be some residual water in the less hydrated state. This is apparent from the difference in size between the EF and Drying process modes near unity.

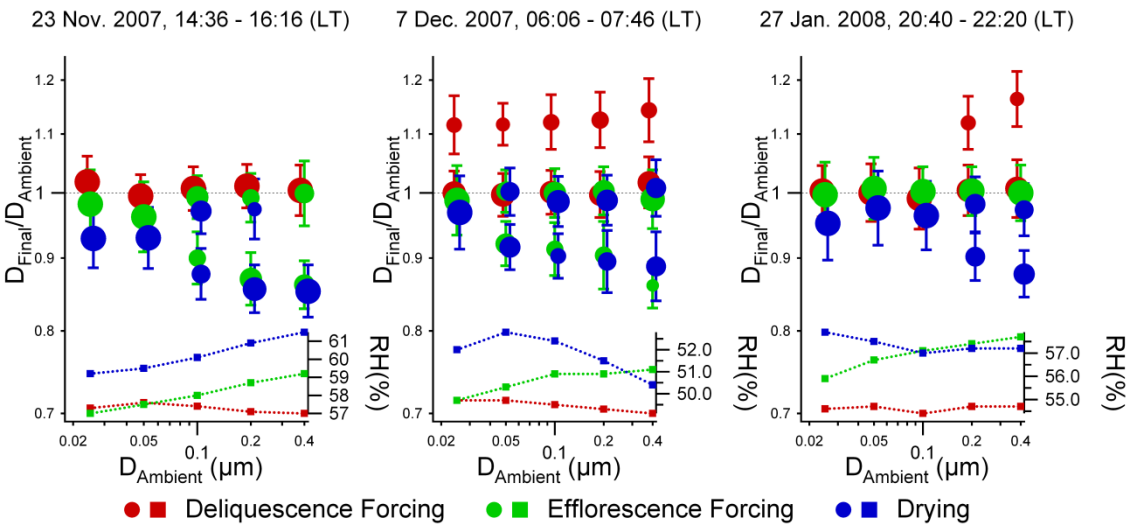

Figure 11: Results of three AS-TDMA full measurement cycles from the GRSM winter campaign.

The variety of results from the winter campaign defied easy typecasting (as the summer). Though the number of variations in the 432 recorded measurement cycles prohibits full treatment in this format, a few characteristics may be noted. First, the multi-modal behavior apparent in the three winter plots above was fairly typical. This contrasts with the summer results that were more typically mono-modal. A second contrast, also treated in the result summaries, is the general lack of residual water in the less hydrated state of hysteretic aerosol during the winter. Finally, it should be noted that the simultaneous appearance of more- and less-hydrated states seen in the second of the winter plots was a regular feature. It is apparent in the winter time series and its frequency is illustrated in Fig. 16 the surrounding discussion. It is a surprising feature and deserves some consideration.

RH history is a determinative factor of hydration state. In conjunction with this, the coexistence of a more and less hydrated state is interesting, if not problematic. Though it is beyond the scope of this work to rigorously treat this question, two possibly complimentary mechanisms can be suggested. First, it might be explained by differences in efflorescent and deliquescent transition points within the aerosol populations. A second explanation is mixing of parcels with different RH histories. This question will appear again in the second of the following time series. The AS-TDMA results will not be sufficient to answer this question but more context is provided in that format.

Time series

This section discusses Figs. 12 and 13: two time series of ASTDMA results from the course of several days during each study period. The plots differ from those above primarily in that the ordinate is time rather than ambient size, now depicted by color. For the sake of clarity only two sizes, 0.05 and 0.2 μm, are shown. In addition to the ambient RH, these time series show the controlled RH to illustrate the proficiency of the instrument at reproducing ambient levels.

This format neatly depicts transitions in the hydration characteristics of ambient aerosol. The following examples illustrate the effect of varying RH on both the detection of hysteresis and the hydration state observed. However, it must be emphasized that the length of time considered is sufficient to include significant variation in the aerosol. The treatment of concentration in these plots is deceptive as it is normalized by the total AS-TDMA scan concentration (i.e. each resultant size distribution is normalized to unity total concentration). This emphasizes the contribution of individual modes but obscures

aerosol population dynamics and comparative concentration. These cautions notwithstanding, the following plots highlight interesting variety in hydration behavior.

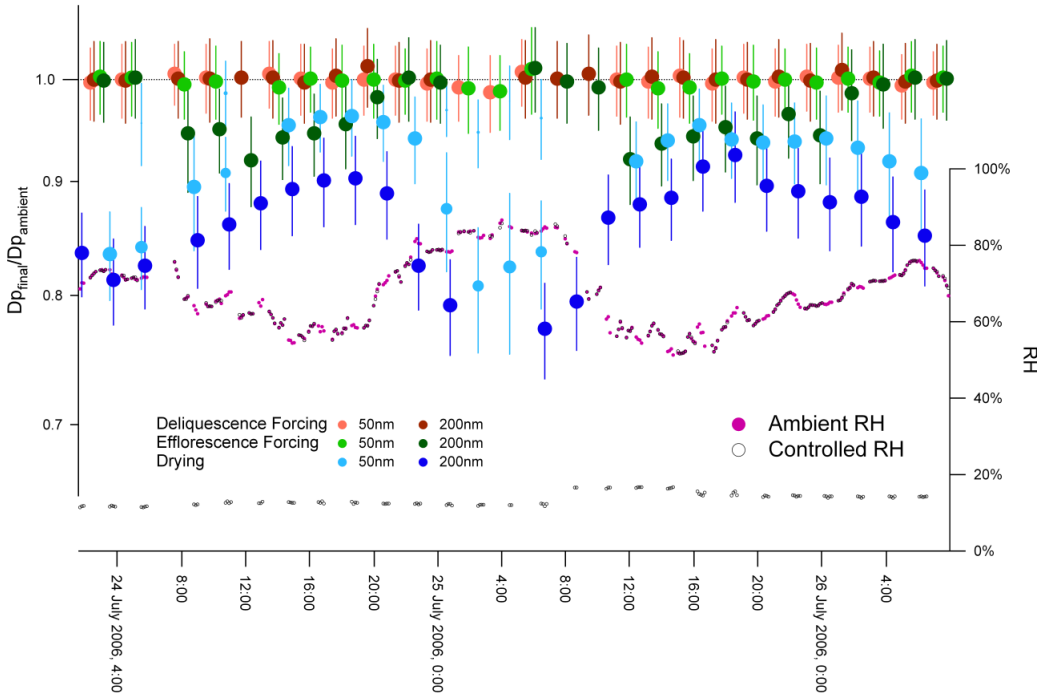

Figure 12: A time series of AS-TDMA measurements from the GRSM summer campaign. The point and error bar markers follow the convention described in the Methods section.

A typical time series from the summer campaign is shown in Fig. 12. It includes all measurements made over a 2.5 day period. It features the diurnal RH cycles that were shown, in Fig. 3 of the seasonal characterizations, to typify the period. A portion of the Drying process results (in blue) mirror the ambient RH, indicating a significantly hygroscopic aerosol fraction. The larger sizes are generally bottommost, or most hygroscopic: an attribute noted in the measurement cycle plots above. The DF results (in red) are consistently near unity in coherence to the study-long failure to detect any less

hydrated ambient state. The EF results vary with RH. During the nights and mornings when the RH is high, the EF results remain near unity. As RH decreases through the afternoons, a portion of the EF results begin to indicate water loss. This suggests that a portion of the aerosol does exhibit hysteretic hydration behavior, but that the deliquescence threshold is crossed as the RH increases beyond the domain of hysteresis.

As noted, this was a typical case for the summer. Most generally, some portion of the ambient aerosol would exhibit hysteresis when RH levels fell. The transition point and portion of the aerosol involved varied. Detecting that transition point is a task better suited to the RH-scanning H-TDMA. Thus, the primary unique AS-TDMA result from the summer is quite monotonic: whenever hysteresis was detected, the aerosol was found in the more hydrated state.

This was not so during the winter. Figure 13 depicts a case study chosen from the GRSM winter campaign that shows changes in the hydration state detected during a 2-day period. Three related aspects of hydration state variability highlighted in this case study are interesting, if not surprising. The first is the variability of the detected ambient hydration state despite local RH remaining within the RH domain of hysteresis. The second is the continuous variation of the fraction in each state, evident from the changes in the relative concentration of less-hydrated particles. The final feature is that only part of the hysteretic fraction at each size is ever detected in a less hydrated state.

Before discussing these more subtle points, one additional feature should be noted. This plot shares with the summer case study a descent of ambient RH into and out of the RH domain of hysteresis of some fractions of the aerosol. This occurs during the

first and second measurement cycles, shown at 09:00 LT, 6 December 2007; with hysteresis detected only during the 0.4 μm EF measurement (not shown) in the first and the detection of a hysteretic fraction of all sizes in the second. Near the end of the case study, ambient RH rises out of the hysteresis domain with no non-unity EF or DF results appearing after 00:00, 8 December. Unlike the summer case study, RH also appears to fall below the domain of hysteresis, with little hysteresis detected in the measurement after 12:00, 7 December.

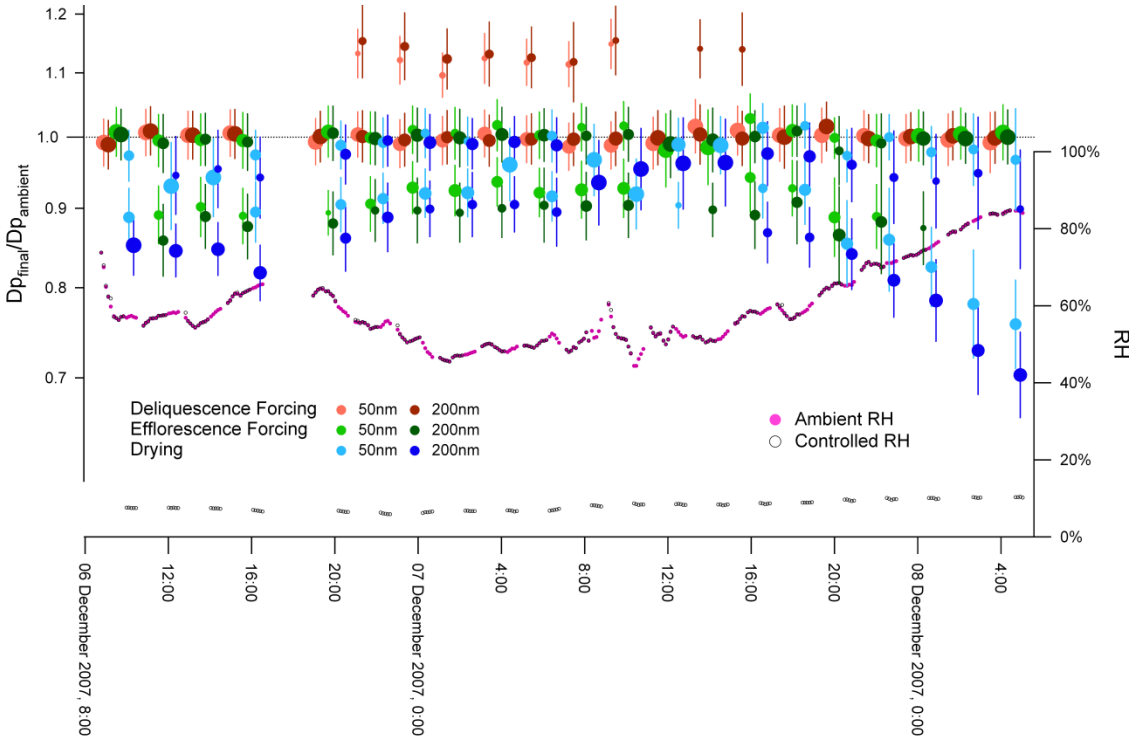

Figure 13: A time series of AS-TDMA measurements from the GRSM winter campaign. The point and error bar markers follow the convention described in the Methods section above.

The first of the points listed above, the variability of hydration state within the apparent RH domain of hysteresis, is illustrated best by the appearance and disappearance of less hydrated fractions in the results. These occur while RH is falling and rising, respectively. Yet, though RH continues to fall (and rise), a hysteretic fraction continues to be detected. This indicates that the endpoints of the hysteretic domain, the RH's for irreversible efflorescence and deliquescence, are not reached. In the case of disappearing less hydrated states, the transition occurs well in advance of the apparent deliquescence RH indicated by the cessation of hysteresis detection at 01:00, 8 December. Similarly, local ambient RH falls significantly following the first appearance of the less hydrated state before reaching the supposed efflorescence RH immediately following 12:00, 7 December.

During this period of falling RH after the first appearance of less hydrated, hysteretic ambient aerosol, the second interesting feature is evident. The fraction of hysteretic ambient aerosol determined as less hydrated continues to increase with falling RH. Though not evident, the total hysteretic fraction for the smaller sizes increases during this time, but the 0.2 μm hysteretic aerosol fraction remains constant. For that size, it appears that the hysteretic population is conserved while a portion of more hydrated aerosol transitions to the less hydrated state. However, at no point do all hysteretic aerosols occupy a less hydrated ambient state. This third feature is broadly evident, but is most surprising following the apparent fall of RH below the domain of hysteresis at 12:00, 7 December.

Before speculating further about these features, some consideration is given here to the typicality of this case. During the winter campaign the detection of less hydrated, hysteretic aerosol most often involved a similar apparent transition from a fraction of metastable aerosol as RH fell. The exceptions were 2 cases in which the RH fell lower than the ostensible efflorescence point. When RH rose back into the hysteretic domain, the hysteretic fraction was generally detected in a less hydrated form. However, the gradual increase, with falling RH, in the portion of hysteretic aerosol in a less hydrated form depicted in the case in Fig. 13 is typical. Similarly, the gradual reversion of the hysteretic fraction to a metastable state with increasing RH is typical. For both transitions, the noted feature that they occur while local RH remains within the bounds of efflorescence RH and deliquescence RH is consistent in all observed cases. Also, these transitions all proceeded through a regime in which more- and less-hydrated states were simultaneously detected. In some cases, as RH fell sufficiently low, the entire hysteretic aerosol fraction was eventually found in a less hydrated state. Yet, this complete reduction in the portion of metastable aerosol progressed gradually with falling RH.

This case study is thus largely typical. One additional feature should be covered, springing from the two exceptional cases mentioned above in which RH apparently fell below the domain of hysteresis. The notable feature of these cases is that the apparent efflorescence RH (determined by the cessation of hysteresis detection with low RH) is near the RH at which the meta-stable fraction disappears: much nearer, particularly, than the apparent deliquescence RH (detected in the case above near 00:00, 8 December

2007) is to the RH at which a less hydrated, hysteretic fraction is no longer present in the case above and all others considered.

Taken together, these characteristics suggest a significant degree of mixing and a significant divergence between the local RH and the RH history of the particles. The bias discussed in the previous paragraph suggests that the RH history is more often perturbed higher than lower. This bias is likely due to the characteristic profile of increased RH with height in active boundary layers. Finally, the ridge-crest location of the measurement facilities should be recalled, adding complication. In conclusion, the results depicted in this case study suggest that ambient hydration states are quite dynamic, highlighting the need for comparative studies between the various model treatments of hydration state and in situ measurement.

GRSM Study Summaries

This section features a variety of plots summarizing AS-TDMA results from the two measurement campaigns. It begins with a set of simple summaries of the AS-TDMA DF and EF process results. The next element treats the seasonal contrast in water content of the less hydrated state of hysteretic aerosol. Finally, two sets of plots illustrate relations between the observance of hysteresis and time of day, RH and the composition measurements discussed above.

AS-TDMA deliquescence forcing and efflorescence forcing process results summary

The frequency plots in Fig. 14 simply summarize the DF and EF AS-TDMA measurements for each ambient size during the two measurement periods. In keeping

with convention, the DF process results are shown in red and EF results in green. The counting is based on the modes characterized by log-normal curves. Each mode is counted as the fraction it contributes to the total concentration in its containing size distribution. Each measurement is given a total weight of 1. The grey bars indicate the fraction of non-hysteretic results. These are calculated based on the portion of aerosol in each measurement not accounted for by a hysteretic DF or EF process mode. In effect, they are 100 % less the sum of the bars shown in red and green.

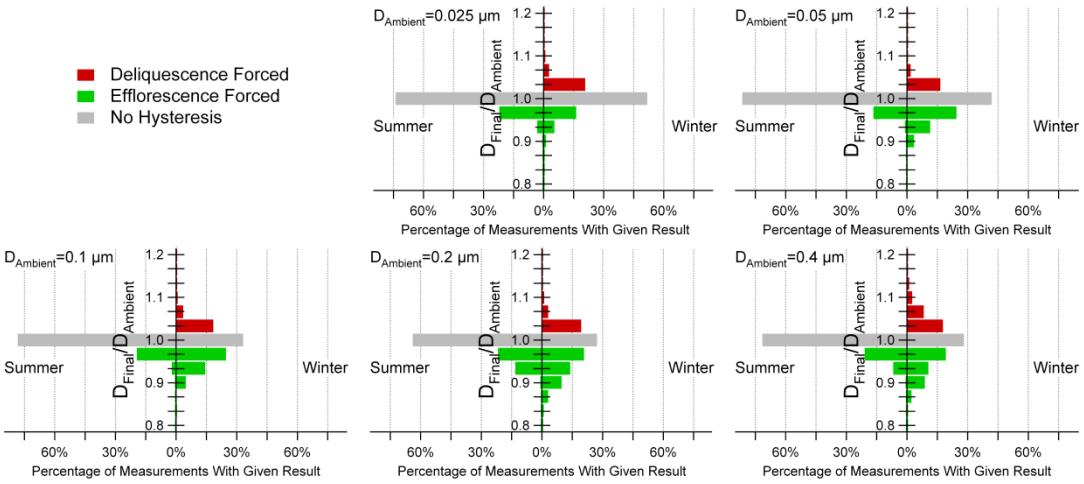

Figure 14: Deliquescence and efflorescence forcing measurement summaries for the GRSM summer and winter campaigns.

Two major features appear in the summer results. The first is the lack of less hydrated, hysteretic aerosol, indicated by no non-unity DF results. The second is the variation with size in the portion of more hydrated hysteretic aerosol. A maximum frequency of detection occurs in 0.2 µm measurements. This corresponds with the size variation noted in the single measurement cycle results shown above. The winter results

stand in contrast to the summer on two points: more frequent detection of hysteresis and variety in the hydration state detected. Similar to the summer, the winter results also show variation with size. Most frequent detection of hysteresis occurred with the larger sizes. Interestingly, there is little size variation in the fraction of less hydrated states detected.

Residual water

The charts in Fig. 14 summarize only the differences between hydration states. However, as indicated in the discussions of the measurement cycle examples, there was a seasonal contrast in the amount of water contained in the less hydrated state. This is based on the difference between the least hydrated state and the Drying process results.

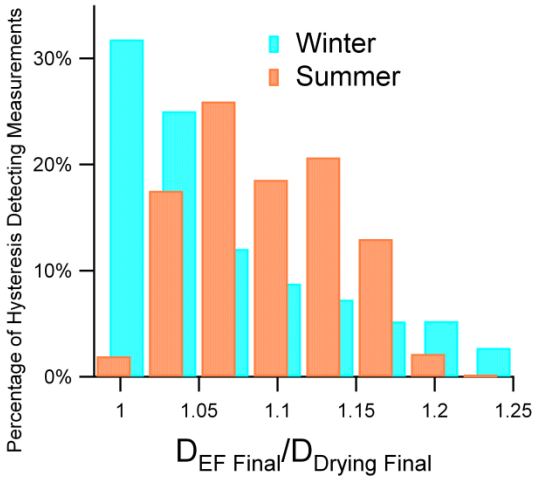

Figure 15: A frequency plot illustrating the variation in residual water content of the less hydrated state between the GRSM summer and winter studies.

The formations of this and the remaining charts in this section rely on the qualification of each mode (as characterized by log-normal curve fits) in each EF and

DF process measurement as either hysteretic or non-hysteretic. This qualification is discussed in the methodology appendix (Appendix part 4). As with the previous charts, modes are counted as the fraction they contributed to their containing size distribution.

The residual water in the less hydrated state is quantified here by the ratio of final diameter following the EF process and following the Drying process. Figure 15 contrasts this result for the GRSM summer and winter campaigns. Only the measurements in which hysteresis is detected are counted. Also, the hygroscopic growth model described in the methodologies section was applied to simulate equivalent results at 60 % RH. This corrected for the additional bias introduced by variation in the RH at which hysteresis occurred, a concept more fully treated in the next sub-section. As previously noted, the difference between the post-EF and post-Drying sizes was generally larger during the summer. This is indicated by more common occurrence of higher ratios.

Relative humidity and time-of-day dependence of hysteresis detection

Figure 16 contains frequency plots of the detection of hysteresis versus time of day and versus RH. The formation of these relies on the hysteresis qualifications already discussed and counts each measurement as a unit with multiple modes as their appropriate fraction. The frequency is normalized by the total number of measurements, so that each bar indicates the fraction of all measurements (not only those detecting hysteresis) of each type (EF or DF) that both has the characteristics of the bin and is categorized as hysteretic. Because of this, the bars do not sum to 1, but to the total fraction of hysteresis detection. For comparison, the total fraction of all measurements that were conducted under the bin conditions are also plotted in the RH charts using the

right axis. Finally, the darker portion of the bars in the GRSM winter RH chart indicates the fraction that was detected in coincidence with the other hydration state, mentioned in the case study discussion.

The major feature of the summer RH chart is the lack of hysteresis at high RH. This also appears in the winter chart, but the truncation occurs at higher RH levels. This cutoff corresponds roughly to an average RH for deliquescence during the season and the higher deliquescence RH in the winter is in accordance with the estimates from composition illustrated in Fig. 4. The summer and winter charts also contrast in overall frequency of hysteresis. But the greatest contrast lies in the detection of less hydrated, hysteretic aerosol during the winter.

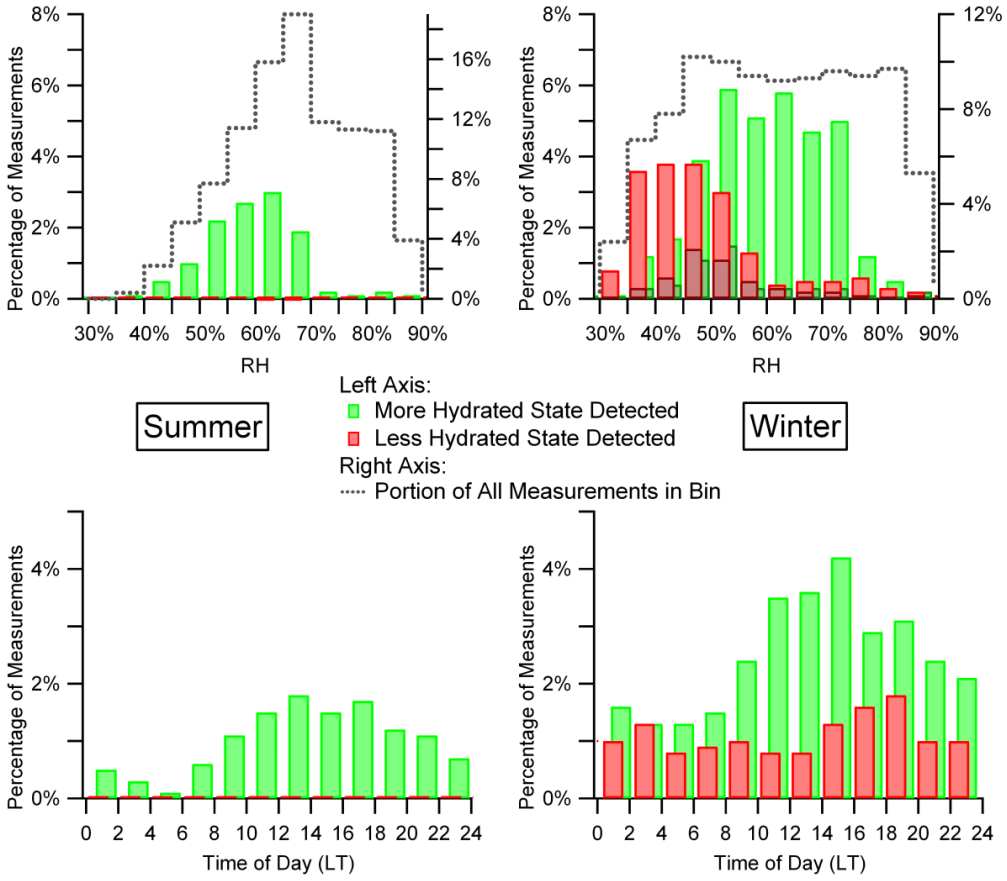

Figure 16: Frequency plots of hysteresis detection versus RH and time-of-day for GRSM summer and winter campaigns. The darker portion of the bars in the winter RH plot indicates fractions detected in coincidence with the alternative hydration state.

The winter RH based hysteresis frequency chart illustrates a strong relationship between RH level and hydration state, with less hydrated states being more frequently detected at low RH. It also shows the predominance of more hydrated over less hydrated states. Reasons for this predominance can be suggested. First, it is evident from the dashed distribution of total measurement frequency that ambient RH more often exceeded the deliquescence point than it fell below the efflorescence point. In addition, as discussed concerning the winter case study, there appears to be a bias in RH history

versus local, ambient RH history toward higher RH. This would follow from active boundary layer circulations. However, these suppositions need further work and treatment of local atmospheric dynamics to be confirmed.

From comparisons of the dashed distribution of total measurement frequency of each season it is evident that RH fell lower in the winter than in the summer. Yet it is interesting that the detection of less hydrated, hysteretic aerosol in the winter often occurred at RH levels reached during the summer. This could be the result of likely seasonal differences in the efflorescence point, similar to the variation in deliquescence RH roughly evident in the charts. But an additional factor could be local dynamics. As illustrated in the depictions of diurnal RH and temperature in Fig. 7, in the summer RH generally fell in conjunction with daytime heating. Thus, the periods of low RH were likely associated with active boundary layers. This in turn would suggest that the RH history is driven by boundary layer circulations with accompanying lofting, cooling and increased RH. In contrast, the weak diurnal variation illustrated for the winter period both in the case study (Fig. 13) and Fig. 7 seems less susceptible to this bias.

The lower set of charts shows the time-of-day dependence of hysteresis detection. The results are strongly anticipated from RH dependence above and RH and temperature characterizations in Fig. 3. Thus the summer plot indicates a strong diurnal cycle. While the winter plot shows a cycle as well, it is weaker and hysteresis was detected at all times of day. No total measurement frequency plot is included in the time-of-day charts to avoid confusion. It would be equivalent to the time-of-day distribution shown in Fig. 7 that has the major characteristic of nightly depression due to the

inoperability of the instrument at very high RH. However, as the RH plots in Fig. 16 show, it is highly unlikely that hysteresis would have been detected during these periods. Otherwise, measurements were conducted with nearly uniform frequency. Thus, the missing measurements should not be assumed to contain a similar proportion of hysteresis detection as by-eye comparisons would suggest.

GRSM Hysteresis detection versus filter composition results

In this final sub-section, the relationship between the filter composition measurements and the detection of hysteresis is considered. This comparison is slightly compromised by limitations on the size and time resolution of filter based measurements. However, beyond being the best available composition data, these filter results are comparable to the nation-spanning IMPROVE network. This greatly increases the possible applicability of constructive comparisons. The AIM model deliquescence predictions shown in Fig. 8 are the basis of this comparison. Efflorescence is not treated for a variety of reasons: first, the determination of efflorescence RH thresholds is significantly more difficult, being dependent on solid phase nucleation kinetics rather than bulk thermodynamics (as deliquescence). Consequently, models predicting this behavior are not as readily available. Secondly, full efflorescence and cessation of hysteresis detection rarely occurred in these studies. Therefore, this comparison focuses on the deliquescence transition as predicted by composition and indicated by cessation of hysteresis detection in AS-TDMA measurements.

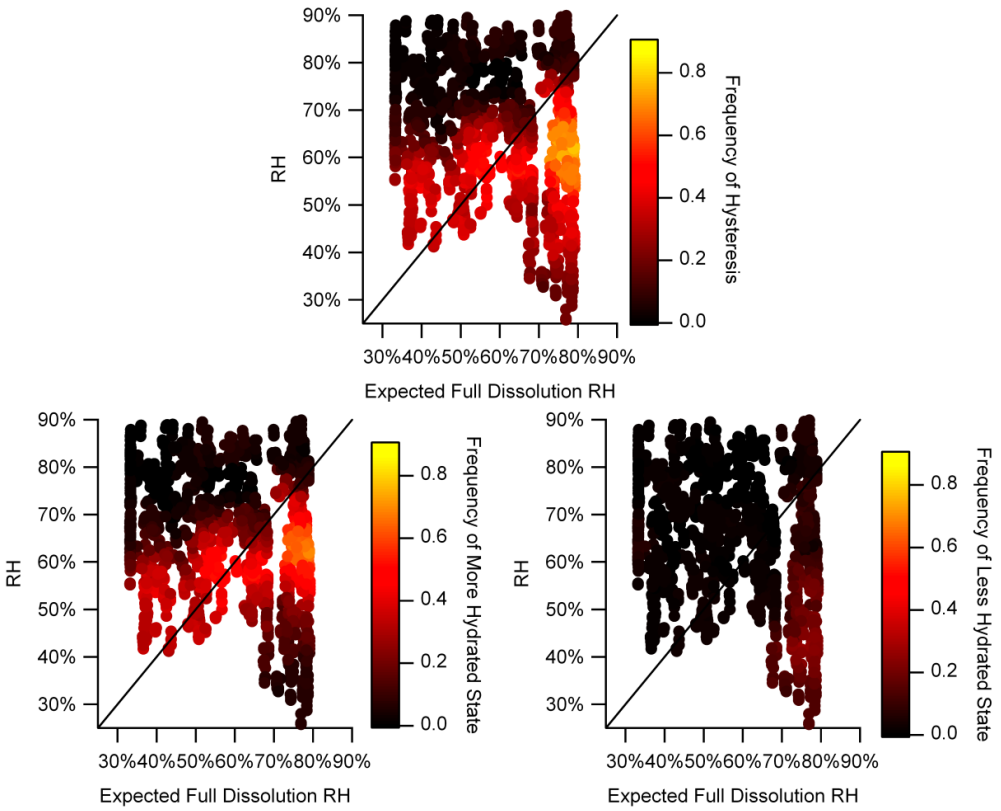

Figure 17: Hysteresis detection versus the ambient RH during measurement and filter determined composition based estimates of deliquescence RH. The upper chart indicates frequency of any hysteresis detection, while the lower two treat each state individually. Every measurement from both campaigns is plotted based on the interpolated AIM estimate of dissolution RH and ambient RH at the time it is conducted. The frequency at each point is calculated as the fraction of the nearest 80 measurements that detect either (or both) hydration state, depending on the plot.

Figure 17 depicts the relation between predicted deliquescence RH, ambient RH, and hysteresis detection and was formed as follows. First, the filter composition results were interpolated to all of the measurement triplets (DF, EF and Drying process) from the intensive periods of each campaign. The interpolation was based on the time each measurement occurred and ascribing the daily filter results to 12:00 p.m. From these compositions the expected full dissolution RH was calculated for each AS-TDMA

measurement using AIM as described in the first portion of the results section. Each measurement was then plotted as a point in the charts of Fig. 17 with coordinates of the expected full dissolution RH and the average ambient RH during the measurement. Next, the point was shaded based on the fraction of measurements with similar RH coordinates that detected more- or less-hydrated (or either), hysteretic aerosol, depending on the plot. The local hysteresis frequency was calculated for each point using the nearest 80 measurements under a simple distance on the ambient RH, calculated dissolution RH coordinates.

With this formation, if the ambient aerosol deliquescence RH is consistent with expectation from composition, hysteresis should be detected only and universally at coordinates below the 1:1 bisection. This is not the case. Focusing on the top plot, it is evident both that hysteresis is detected beyond expected deliquescence RH levels and that hysteresis is not consistently detected below the expected deliquescence levels. This result is somewhat anticipated by the illustrated size dependence of hysteresis detection already discussed. Beyond this, however, there is a surprisingly persistent threshold for hysteresis. The less hydrated state detection indicated does not form as distinct a feature, a consequence of the deliquescence basis of the plot.

Mount Rainier and Acadia Studies

AS-TDMA measurements were also made in subsequent summer campaigns at Mt. Rainier (Washington, USA) and Acadia National Parks (Maine, USA). As described in Table 1, hysteresis was detected less frequently (versus GRSM) during both studies, and only for particles 0.1 μm or larger. These results are consistent with H-

TDMA and aerosol composition analysis during these studies, both of which only occasionally indicated an aerosol capable of hysteresis. Only meta-stable aerosols were detected during these projects, despite ambient RH frequently falling as low as or lower than during the GRSM Winter project. This behavior is likely driven both by relatively lower efflorescence RH and by boundary layer dynamics.

Table 2: Summary of hydration state measurements.

	More hydrated state indicated (% of measurements)					Less hydrated state indicated (% of measurements)					$NH_4^+ : SO_4^{2-}$ (molar ratio)†
Ambient Size (µm)	0.025	0.05	0.1	0.2	0.4	0.025	0.05	0.1	0.2	0.4	PM2.5
GRSM(S)	26	26	32	45	29	0	0	0	0	0	1.17 ± 0.22
GRSM(W)	24	29	27	29	26	25	20	24	27	35	2.4 ± 0.80
MORA	< 1	1	2	20	26	0	0	0	0	0	1.86 ± 0.30
ACAD	1	< 1	< 1	< 1	17	0	0	0	0	0	1.26 ± 0.51

† Corrected ratio taken from Lowenthal et al. (2014).

MORA and ACAD Aerosol Characteristics

Unlike the persistent regional sulfate haze that dominated the GRSM measurements, MORA and ACAD PM2.5 sulfate levels varied widely. Both sites draw from disparate source regions. MORA is influenced by eastward flow from either industrial regions along Puget Sound or (more frequently) rural regions south of the Seattle-Tacoma metro area. But it is also influenced by fairly pristine wilderness areas to the north, south and east, as described in introduction to this dissertation (fig. 4). Figure 18 shows a time series of PM1.0 composition derived from Aerosol Mass Spectrometry (AMS) measurements during the MORA project, with associated TDMA

scans. The period of high sulfate (and interrupted measurements) from August 23rd to 25th corresponds to a front passing through and a temporary shift from rural to urban/industrial source regions, as shown in Fig. 18. As indicated in Table 2, sulfate at MORA was associated with more ammonium, consistent with more prevalent hysteresis.

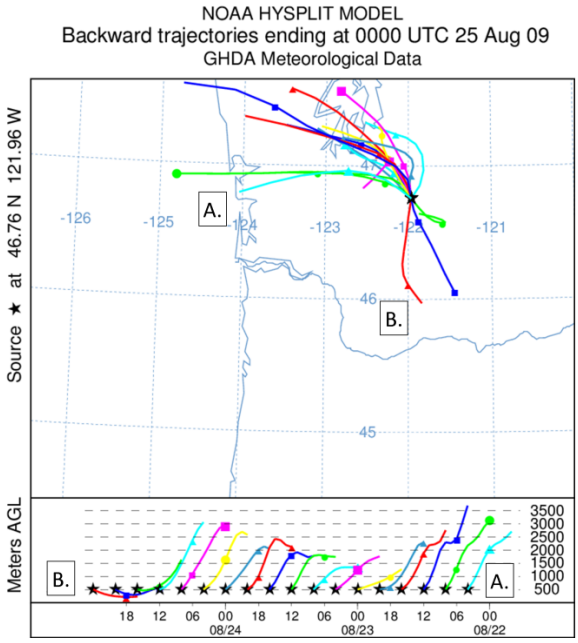

Figure 18: NOAA Hysplit backtrajectories corresponding to high sulfate period during MORA project.

ACAD aerosols may come from the rural Maine interior or from highly developed regions along the New England Coast. Figure 20 shows a rough correlation between coastal aerosol sources and the appearance of hysteresis. Coastal influences typically corresponded to higher anthropogenic pollution levels, particularly sulfate. In

contrast to MORA, the ACAD aerosol contained more acidic sulfate, reducing the likelihood of hysteresis.

Linking these two studies in contrast with GRSM is a lack of local sulfate sources. This is evident in both the sporadic presence of sulfate, and its evident correlation to likely source regions. This characteristic also influences the AS-TDMA results. As shown in Table 2, hysteresis under ambient conditions was only detected for the largest particles, which is consistent with sulfate being primarily present in aged, remotely sourced aerosol.

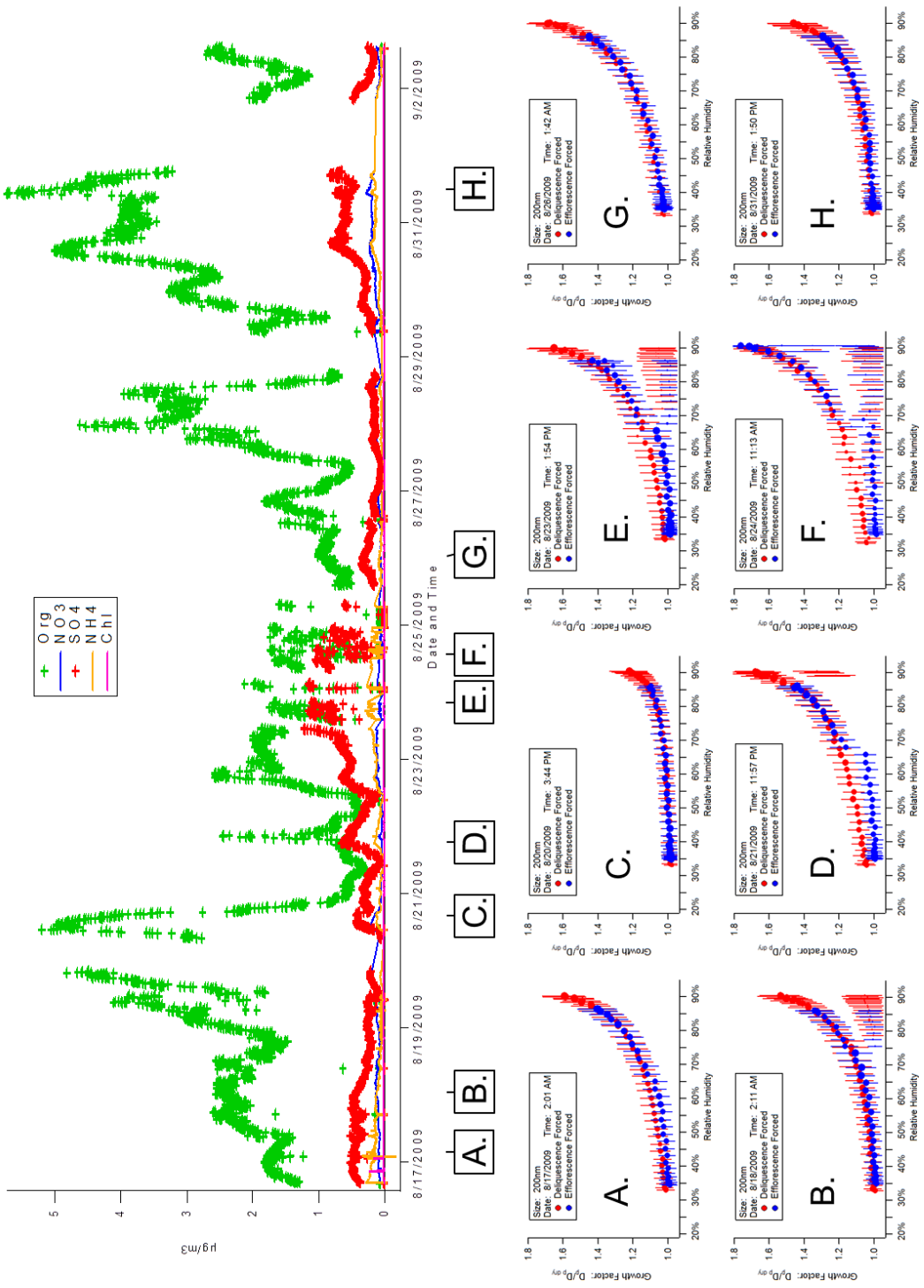

Figure 19: Rough correlation between integrated AMS aerosol composition and hysteresis at MORA. Hysteresis is primarily indicated when sulfate levels are high. The MORA aerosol was notably complex—most hygroscopic growth measurements were noisy with multiple modes present.

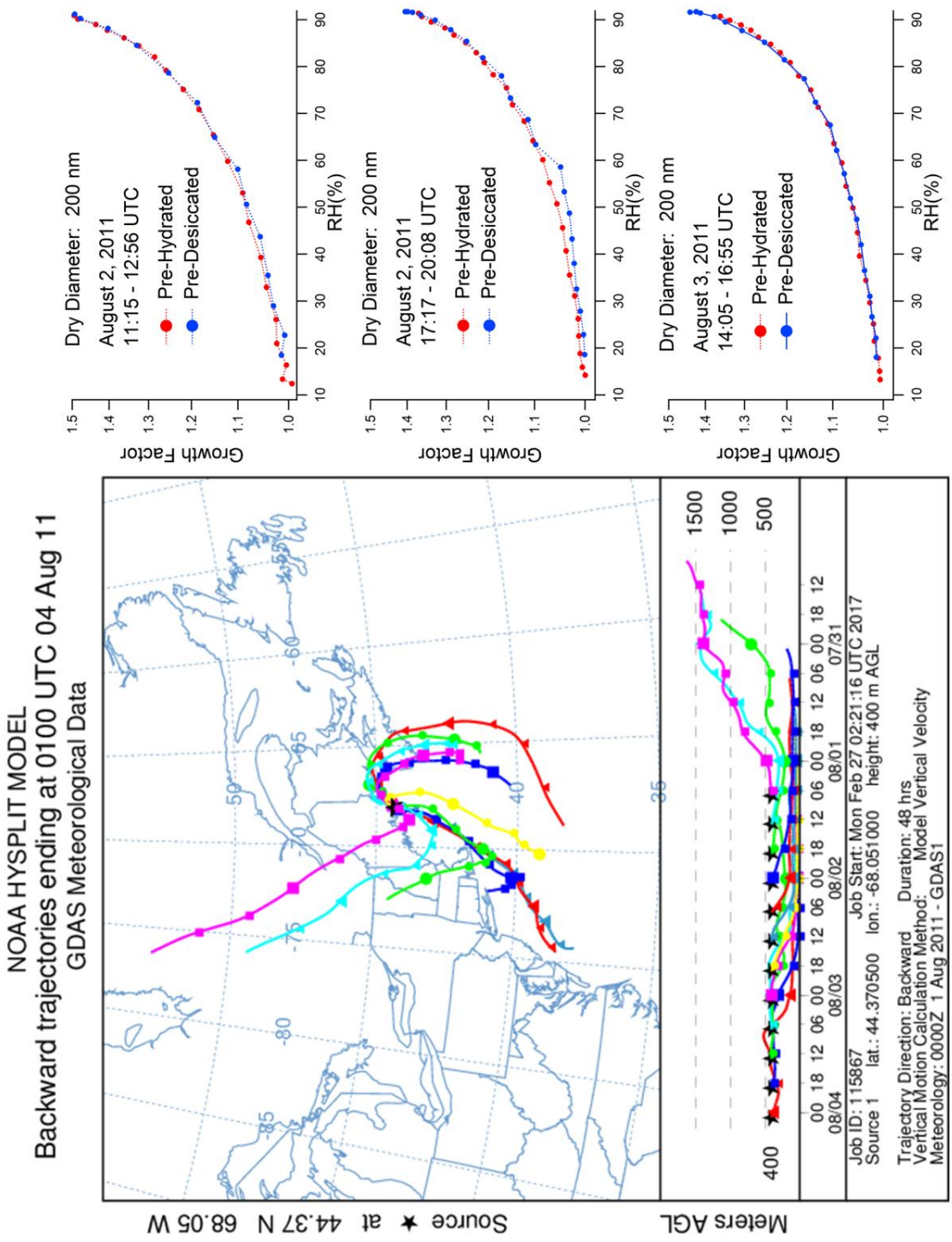

Figure 20: Influence of ACAD source regions. Occasionally during the month-long ACAD study, the site received influences from coastal New England, which typically corresponded to the appearance of hysteresis and higher PM2.5 sulfate.

Limits on Less-Hydrated/Crystalline State at MORA and ACAD

As indicated in Table 2, AS-TDMA measurements only detected meta-stable aerosol during the MORA and ACAD studies. Particularly at ACAD, this behavior was likely driven in-part by relatively low ERH. As noted above, ACAD sulfate was more acidic, which corresponds typically to a much lower ERH. The study wide average ammonium –to-sulfate ratio reported by Lowenthal et al. at ACAD (1.26) corresponds roughly to an ERH of ~10% (Martin et al., 2003). This is consistent with H-TDMA measurements made during this period. RH scan measurement were only made for aerosol with a dry diameter of 0.2 µm, while AS-TDMA measurements only indicated hysteresis at the 0.4 µm *ambient* diameter. But ~5 H-TDMA measurements at 0.2 µm indicated hysteresis and the middle RH scan in Fig. 20 is typical in having an indistinct ERH at very low RH (~15-25%). Surface RH at ACAD did not reach these levels during the project, as indicated by the diurnal RH plot in Fig. 21.

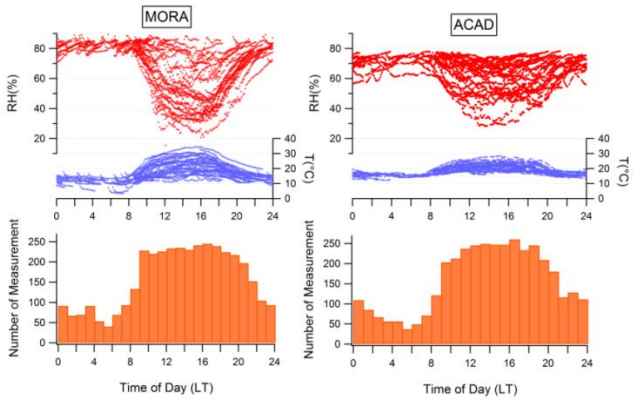

Figure 21: Diurnal RH and Temperature profiles at MORA and ACAD. AS-TDMA operation was suspended when ambient RH reached 80-85% to avoid condensation in the instrument, producing much lower measurement counts during the night and early morning periods of both studies.

Sulfate aerosol at MORA was more fully neutralized and exhibited hysteresis more often, yet still was only found in a metastable hydration state. The ammonium-to-sulfate molar ratio at MORA (1.86) translates roughly to an expected ERH of 30% (Martin et al., 2003). H-TDMA detected ERH and DRH values from MORA are shown in fig. 21. ERH values at MORA were ~5% RH lower on average than at GRSM during the winter (shown in Fig. 6, above). RH at GRSM during the winter was more frequently very low (shown in Fig. 7), but daily RH minimums at MORA were occasionally below the ERH (see Fig. 21). Moreover, for the AS-TDMA to indicate a less-hydrated state—as at GRSM during the winter—the RH must be between ERH and DRH. Thus, at GRSM during the winter, the lower hydration state became more prevalent when ambient RH reached the lower end of that range, as shown in Fig. 16, above. This certainly occurred at MORA; the contrasting results are most likely caused by the atmospheric dynamics controlling RH history and a key difference in the sampling locations.

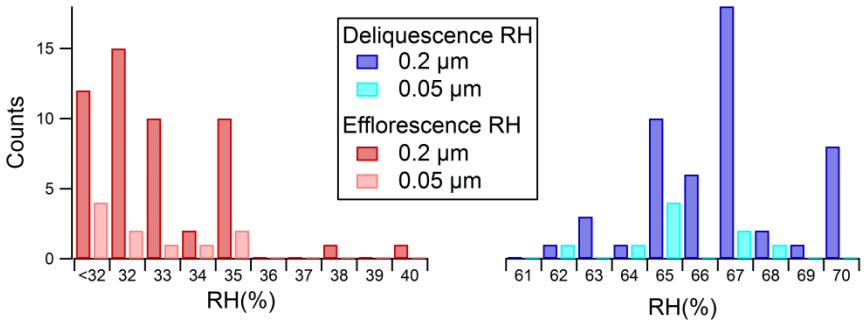

Figure 22: DRH and ERH detected in H-TDMA measurements at MORA. Hysteresis was indicated in 10 0.05 µm and 53 0.2µm RH scans out of ~120 of each size.

This contrast can be rationalized as an effect of boundary layer dynamics and the relative height of the AS-TDMA within the boundary layer. Within a daytime boundary layer, a parcel's RH history is determined by its convective cycles through the boundary layer. Figure 23 shows a typical sounding for the measurement period for Salem, OR, near MORA. The sounding shows a well-developed convective boundary layer that is capped by an inversion at 800mb. In such a boundary layer (one driven by daytime heating), the surface is the warmest and driest part. As air moves up from the surface, it cools adiabatically until it saturates—creating a consistent profile of increasing RH with height. This is the expected profile at MORA during days when RH falls due to diurnal heating. Thus, when RH levels were low enough at MORA to reasonably expect the less hydrated state to occur (the heat of the day), the RH history of all parcels reaching the surface (the point of lowest RH) was high RH in the cooler, moister parts of the boundary layer. If surface RH was below the ERH, no hysteresis would be detected. If surface RH was above ERH, the aerosol would be meta-stable as there would be no opportunity for it to experience lower RH.

The situation was different at GRSM. The GRSM measurement site—Look Rock in eastern Tennessee—is on a ridge approximately 600m above the broad Tennessee River valley to the NW, a common source region for the site. The MORA site is in in the Nisqually River valley, ~300m below the level of the surrounding foothills. Consequently, even within a well-developed boundary layer, GRSM is not situated at the warmest and driest point; adiabatic cooling would result in temperatures ~6 °C cooler and RH 5% higher than the valley floor.

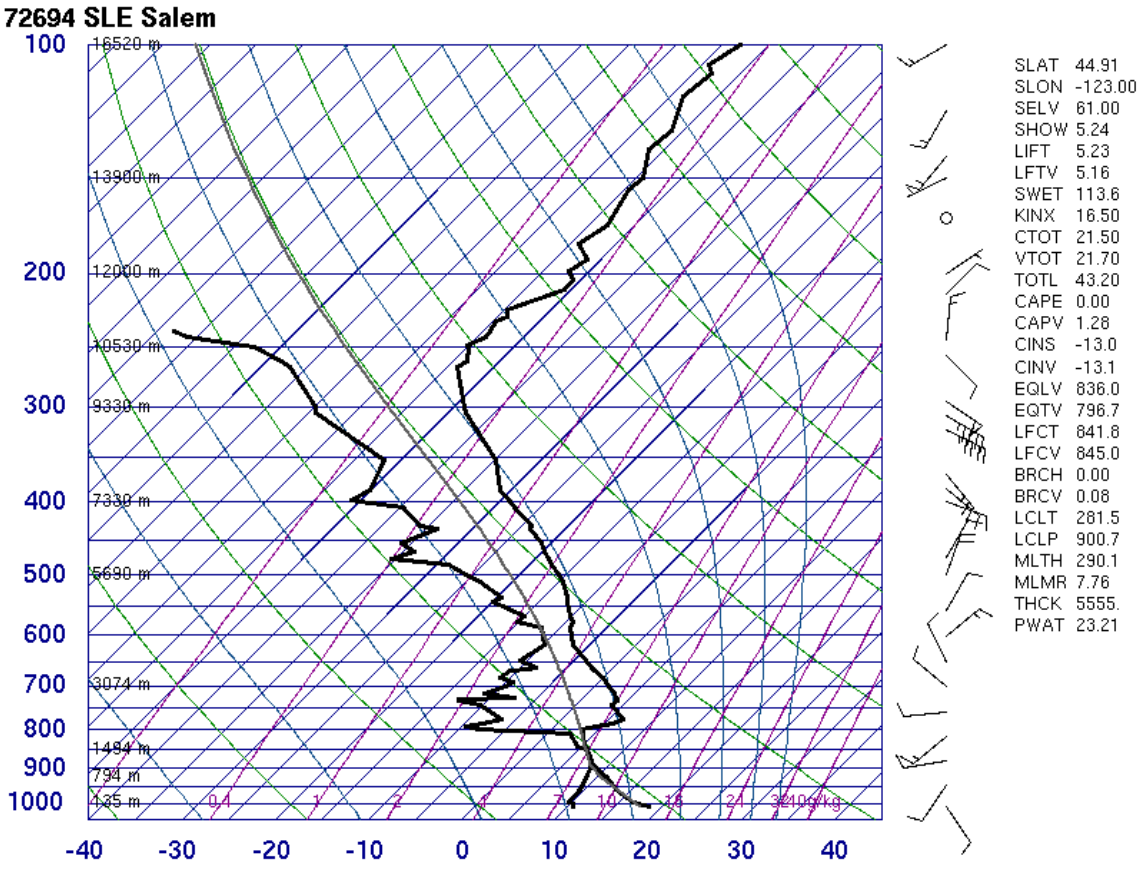

Figure 23: Skew-T plot of atmospheric sounding on August 7th, 2009 at 0:00 UTC (5:00 pm local time, August 6th). Data from the University of Wyoming sounding database.

The less-hydrated state was also detected during the winter at GRSM, when a simple, well-mixed boundary layer may not exist. Likewise, RH during the winter at GRSM did not follow a consistent diurnal pattern. Thus, this dynamic does not control at all sites and seasons. It also is only applicable to boundary layer aerosol. In the sounding in Fig. 23, the layer immediately above the boundary-capping inversion is quite dry and well below the ERH of MORA aerosol. Regardless, boundary layer

dynamics are highly relevant to the RH history of boundary layer aerosol, which constitute the bulk of atmospheric aerosol.

Conclusions

The findings presented in the paper provide a first look at aerosol hydration state in the atmosphere. Primary among the unique elements of this investigation was the positive detection of both more- and less- hydrated forms of hysteretic ambient aerosol. This detection was strongly biased by season, with less-hydrated states detected only during the GRSM winter project. The discussion illustrated that this was likely driven by seasonal variation in RH and aerosol composition, as well as by the characteristics of the sampling location and boundary layer dynamics. Variability in the detection of both states during the winter project allowed us to examine the relationship between local conditions and ambient hydration state. This relationship was shown in case studies to be complex and dynamic. The GRSM winter case study contained several notable features such as the coincident detection of more- and less- hydrated states within the results of a single measurement and the continuous variation in the fraction in these states even as local RH remained within the domain of hysteresis.

These results, complemented by H-TDMA measurements, also illustrate the variability of hysteresis patterns between the sites and seasons. First, the apparent RH levels for phase transitions varied between the two seasons, with the highest RH thresholds for both efflorescence and deliquescence apparent during the GRSM winter. Second, even the less hydrated state typically contained some particulate water. Finally,

detection of hysteresis showed dependence on size, especially during the three summer campaigns.

In the presentation of these results, some considerations of future directions have already been given. First, more sophisticated treatment of local dynamics would greatly enhance the applicability of the findings. While the AS-TDMA has been demonstrated to retrieve the ambient hydration state of aerosol, the ultimate objective is to achieve this determination with models. Future work would be greatly enhanced by the incorporation of modeling efforts. While the Great Smoky Mountains findings clearly show that not all particulate sulfate is hydrated, they also demonstrate the importance of local conditions for that result and underscore the need for measurements in divers environments. In conclusion, the AS-TDMA results from this study provide a first look at the variability of ambient aerosol hydration state. Though future efforts are needed to close gaps in our understanding, the AS-TDMA has been demonstrated to be an effective tool for retrieving aerosol hydration state.

Chapter II Appendix: AS-TDMA Data Treatment

AS-TDMA results take the form of size distributions, as illustrated on the right side of Fig. 6. While this form is adequate for simple evaluations, additional procedures were applied to refine the results and to facilitate more complicated analysis. These are described in the elements of this appendix titled Log-Normal Curve Fits, Mode Correlation, Hygroscopic Growth Model Use, and Qualification of Hysteresis and Scan Offset. Two final elements cover the treatment of multiply charged particles and AS-TDMA calibration.

Log-Normal Curve Fit

The resultant size distributions were produced by inverting the response of the CPC with respect to the final classifier only. This causes the signal from the initial, ambient classifier to remain. This signal is the natural, roughly triangular distribution actually transmitted. Thus, when no change is effected by the inter-classifier processes, the final size distribution accurately depicts this signal. Some groups using TDMA have utilized this signal as a kernel for a second inversion (Gysel et al., 2009); however, additional sources of noise and signal breadth make this technique less applicable to AS-TDMA results. One source of mode broadening is compositional heterogeneity, which causes a blurred response to inter-classifier processes. Also, occasional deviations between ambient and controlled RH levels can generate additional broadening and variation in the location of the effective "no change" size. For these reasons it is difficult to fully invert the AS-TDMA results using traditional methods. Yet, because the size responses of the AS-TDMA processes are often small (roughly analogous to classic hygroscopicity TDMA measurements at low RH) and often involve responses in minor populations of the aerosol, it is imperative to refine the results as much as possible.

To this end, a constrained Levenburg-Marquardt optimization routine was used to fit the data with the sum of up to 4 log-normal modes. An application of this technique is demonstrated in the lower left of Fig. 6 for a set of measurements made during the winter portion of this study. Each lognormal mode is characterized by its relative contribution to total concentration, geometric mean diameter and geometric standard deviation. In effect, this method serves as a pseudoinversion. Each mode ideally

captures the response (both broadening and translation) of various fractions of the initial kernel distribution to the inter-classifier processes. The adaptive nature of this treatment to mode location and breadth make it a good choice for AS-TDMA measurements. Inevitably, there are difficulties that arise from poorly resolved modes. In these cases, the optimization results can be non-unique and unstable. The optimization routine used may also be sensitive to choices of initial guess and this becomes truer in these cases. However, by utilizing systematic and well-tuned heuristics for the initial guesses and the constraints on the mode parameters these effects can be reduced. Non-ideal cases were observed only occasionally; more frequently, the modes were clearly resolved. Overall, though this technique is not rigorous, its systematic application provided consistent results. These results are also ideal for application of the experimental principles of the AS-TDMA. For the DF and EF processes, the criteria of size change can be applied to the mean size of each mode in comparison to the mean size selected by the first classifier. Additional steps are needed to utilize the Drying process results, but they are greatly facilitated by this characterization of the data.

Mode Correlation

The Drying process measurements are made to recover the total amount of water in both the ambient hydration state and final, processed hydration states detected in the DF and EF measurements. To apply the Drying process results, the modes resolved in the DF and EF measurements must be correlated to the modes in the Drying process results that contain those fractions of the aerosol. Moreover, to repair deviations in the synchronization of the ambient and controlled RH, it is useful to correlate the modes

detected in the EF and DF processes. The final product of these mode correlations is a tabulation of all the distinct fractions of the aerosol that are resolved by the three processes. The difficulty achieving this objective ranges from trivial when the aerosol is internally mixed (and therefore characterized by single modes) to impossible when too many modes are resolved in each scan. To clarify the nature of this objective and to motivate the routine and simplifications finally used to approximate it, the correlation process for the measurements depicted in the lower right of Fig. 6 is elaborated.

The correlation of modes in DF and EF results is simple. Any fraction of the ambient aerosol that changes size during one of these processes is assumed to not change size during the other, i.e. a particle does not simultaneously have both a more- and less-hydrated possible state. This requires the assumptions that there are no intermediate ambient hydration states and that no change in the hydration state occurs between the two process measurements. In the results depicted in the lower right of Fig. 6, the DF process resolves a fraction of the aerosol initially in a less hydrated state. Because it is initially less hydrated, that fraction is assumed to be included in the mode that does not change size in the EF process results. Similarly, the fraction found to be initially in a more hydrated state by the EF process is assumed to contribute to the mode at unity size ratio in the DF results. Note that only a subset of the aerosol displayed hysteresis. Less than half of the aerosol is in each of the hysteretic modes, implying a fraction of non-hysteretic aerosol in the modes at unity size ratio in both the DF and EF results. In this way the EF and DF results together resolve both the hysteretic fractions and the total non-hysteretic fraction.

The further correlation to the Drying process results is more problematic. The first two processes have a clear relationship that can be used to compare them. This is not the case with the Drying process. Between it and the DF and EF processes only a weak and often inconclusive relation exists, consisting of a system of constraints on possible water content and the conservation of total aerosol fraction between the three measurements. Consider the case above. The most concrete constraint exists for locating the fraction known to be initially in a more hydrated state. Those particles are known to contain at least the amount of water that was lost as they transitioned to their less hydrated state in the EF process. Thus, that fraction is known to correlate to a fraction in the Drying process results that has lost at least so much water. In the case above, there is a mode that fills this criterion. Locating the aerosol fraction shown to be initially in a less hydrated state by the DF process is less constrained. During the summer measurement period, the amount of water retained in the less hydrated state of hysteretic aerosol was occasionally near 50 % of the amount contained in the most hydrated state. Yet no indication of the residual water content is given by the EF and DF process results alone. In the case above, some headway can be made by assuming the hydration characteristics of the two hysteretic fractions are similar, hydration state aside. This would imply little residual water content in the less hydrated state because the loss of water by efflorescence and by drying is similar for the fraction of the aerosol initially in its most hydrated state. This would also determine the aerosol fraction resolved by the DF process as hysteretic and in a less hydrated state to be in the Drying process mode that shrinks less upon drying. These assumptions are strengthened by the fact that the

aerosol fraction in the Drying process mode with the greatest reduction in size is almost entirely accounted for by the most hydrated ambient aerosol fraction resolved in the EF process measurement. Therefore, that Drying process mode could not contain the entire ambient less hydrated hysteretic aerosol fraction. In this way, the conservation of aerosol fraction can be used to apportion the remaining non-hysteretic population resolved by the EF and DF process comparison. Indeed, for this fraction of the aerosol no other constraint exists.

The above case approaches the limit of reasonable correlation. If an additional mode had been resolved in the Drying process results (a distinct possibility, as the non-hysteretic fraction is unconstrained by the EF and DF results) the apportionment might have been impossible. However, the vast majority of cases were readily correlated, consisting of two or fewer modes from each measurement. In addition, the primary objective is to determine the dry size of the modes resolved in the EF and DF scans. A multiplicity of modes in the Drying process results may depict a variety of externally mixed aerosol types, but these do not necessarily concern this study. Thus, to retrieve an approximation of the dry size in cases where the explicit correlation of aerosol fractions is impossible, the Drying scans were constrained to be fit by at most two major modes. The correlation to these Drying process modes assumed that all hysteretic particles in the most hydrated state were accounted for by the Drying process mode that contained the most water initially, and the ambient less hydrated hysteretic aerosol fraction was entirely contained in the Drying process mode that contained the least water. While this treatment is imperfect, the error it introduces is limited. Also it converges with the

explicit consideration described above, only introducing error in the minority of cases that contain intractably many modes.

These correlations result in a set of descriptions of the various resolved fractions. For each fraction, the characteristic dry size, the ambient size, the size of the most hydrated state it could occupy, and the size of the least hydrated state it could occupy are known. The ambient hydration state can be determined by comparisons between known hydration state sizes and the ambient size. The water content of each state is known by comparison with the dry size. The resolved and correlated populations thus make the ideal result of the ASTDMA operation, allowing full and easy comparison of the three measurements.

Hygroscopic Growth Model Use

It should be recognized that ambient RH did vary sufficiently for the RH during each of the three processes in a measurement cycle to be significantly different. This inconsistency is partially removed by using a hygroscopic growth model to predict from the retrieved values the equivalent response at a standard RH. This treatment has the advantage that it also partially removes the effect of discrepancies between the ambient RH and the controlled RH intended to mirror ambient levels. While this control was mostly excellent, an additional complication was caused by lag between the internal temperature of the ambient classifier column and the actual ambient temperature. The ambient RH probe did not have this limitation. Thus, the controlled RH of the sample stream entering the final classifier was accurate, but sometimes differed from the RH, perturbed by temperature lag, in the ambient classifier. This perturbation was small, but

did decrease the accuracy of detection of hysteretic aerosol near phase transition RH levels. When the aerosol was not near phase transitions, this perturbation is also corrected by the application of a hygroscopic growth model. The limitations of this method lie in its inability to treat phase transitions, only modeling continuous variation of water content with changes in RH. The hygroscopicity model utilized for these manipulations treated the aerosol as a single component salt solution surrounding an inactive "core". The water activity and surface tension of the solution were calculated using parameterizations from Tang (Tang and Munkelwitz, 1994; Tang, 1996; Tang, 1997). The prediction of the equivalent measurement results for an aerosol for an arbitrary, alternative ambient RH was also used to standardize all measurements to a single RH as a means of normalizing the variation in water content due to RH.

Qualification of Hysteresis and Scan Offset

Though these attempts to remove RH and temperature driven deviations in the measurements greatly improved the results, some noise remained in the AS-TDMA measurements. A final refinement of the results was conducted based on the position of non-hysteretic modes in the EF and DF results. These modes should possess a unity size ratio, but occasionally were offset. This was most likely due to too rapid shifts in ambient RH and temperature for either the controlled RH to mirror or the ambient RH probe to capture, thus frustrating the RH correction routines. However, modes in the EF and DF results can be determined to be non-hysteretic on other criteria than unity size ratio. The simplest criterion that indicates non-hysteretic modes without depending on direct comparison to ambient size is similar size ratio for the EF mode with the highest

size ratio and DF mode with the smallest. Roughly 75 % of measurements during the winter contained modes that met this criterion. This size ratio of the non-hysteretic fractions can then be defined as a new effective unity. Using a standard set of similar criteria, a version of the dataset was created that applied determined unity values from EF and DF measurements to their associated Drying process results as well.

Though this technique is not perfectly rigorous, it is expected to produce a reasonable first-order approximation of the actual ambient hydration characteristics. Moreover, it significantly improves the qualification of modes as hysteretic (the primary result of the AS-TDMA), basing the determination on the set of criteria rather than a less reliable unity basis. Also, the offset was only applied to the DF, EF and Drying results together and did not change their relative results. Finally, this technique is applicable to every scan as either the EF or DF process results must have a mode that does not change due to phase transitions.

The qualification of DF and EF process modes as hysteretic is slightly more complicated than applying a threshold deviation from the corrected unity growth. Using a simple threshold of characteristic size ratio in this determination would skew the results, admitting more measurements at high RH where more particulate water is generally involved. To remove this bias, the hygroscopic growth model is applied to the results to simulate their equivalents for a standard RH (here, 60 %). A threshold departure of ± 0.03 (for DF and EF, respectively) from unity ambient-to-final size ratio was then used as the criteria for the determination. While such hygroscopic

manipulations are fraught by unknown surface tension and activity characteristics, the benefits here outweighed introduced error.

Multiply Charged Particles

At this stage, no attempt has been made to recover the effects of multiply charged particles in the AS-TDMA results. This is due primarily to unfortunately unavailable, necessary knowledge of the concurrent ambient size distribution; but, also to the non-triviality of developing the necessary procedures. Based on the limited ambient size data available, it is expected that multiply charged particles will very rarely contribute more than 8 % to the resulting AS-TDMA size distributions, save for the 0.1 μm ambient diameter measurements. At that size, the normal contribution is closer to 18 %. This is significant, but note that multiply charged particles only blur "size-resolution" and are evident only when sharp transitions with size exist in the response to the inter-DMA process (i.e. when the lost "size resolution" becomes salient). In conclusion, it is possible, in principle, to retrieve these errors with data procedures; these have not yet been developed for the AS-TDMA; and this lack does not greatly undermine the value and use of this data set.

Calibration

In this final element of methodology the calibration techniques for the AS-TDMA are described. Similar to other TDMA systems, the RH probe calibration is derived from the instrument response to a known aerosol. The calibration of the other critical TDMA components, the flow meters and high voltage sources, were based on direct measurements.

The RH calibration was inferred from AS-TDMA measurements conducted on atomizer generated ammonium sulfate aerosol. The atomizer generated aerosol stream was conditioned to contain both meta-stable hydrated and crystalline particles by dividing the initially hydrated stream into two parts, drying one part with a Nafion bundle and recombining. In addition, the apportionment between the two streams was adjustable, allowing the manipulation of the final RH level for multiple calibration points. Before it entered the first classifier, it was allowed to come to equilibrium with ambient temperature. From the results of the AS-TDMA measurements made on this aerosol, the actual ambient and controlled RH were determined. The two could be calibrated independently with this aerosol as only the hydrated fraction (either ambient or post-DF process) is sensitive to RH. Thus, the magnitude of growth by the initially crystalline fraction in the DF process only reflects the RH in the second classifier and controlled RH probe. Conversely, the loss in particulate water in the EF and Drying by the initially hydrated fraction indicates the RH levels in the ambient classifier and ambient RH probe only. The actual RH levels required to sustain the water content detected were calculated using activity and surface tension data from Tang (Tang and Munkelwitz, 1994; Tang, 1996; Tang, 1997). For calculating the dry particle volume, the crystalline particles were assumed to be non-spherical with mobility equivalent diameters 1.02 times greater than their volume equivalent diameters (Biskos et al., 2006). Table 3 lists the values inferred from each process for each of the aerosol fractions. The quantity 1 Q sheath /HV refers to variation in size selection accuracy between the two classifiers: Q sheath refers to the sheath flow rates and HV refers to the

classifier high voltage levels. These are the two variables that determine classifier accuracy and are calibrated directly. The duplicity evident in Table 3 allows additional checks on the consistency of these variables during RH calibration.

Table 3: Calibration parameters of AS-TDMA.

	Process	Result	Reflected in Size Change
Initially Metastable Fraction	DF	little or no change	ΔRH, $\Delta Q_{sheath}/HV$
	EF	shrinking	$RH_{Ambient}$, $\Delta Q_{sheath}/HV$
	Drying	shrinking	$RH_{Ambient}$, $\Delta Q_{sheath}/HV$
Initially Crystalline Fraction	DF	growth	$RH_{Controlled}$, $\Delta Q_{sheath}/HV$
	EF	little or no change	$\Delta Q_{sheath}/HV$
	Drying	little or no change	$\Delta Q_{sheath}/HV$

CHAPTER III

HYGROSCOPIC GROWTH OF WATER SOLUBLE ORGANIC CARBON ISOLATED FROM ATMOSPHERIC AEROSOL COLLECTED AT U.S. NATIONAL PARKS AND STORM PEAK LABORATORYAND LITERATURE REVIEW[*]

Introduction

This chapter examines the hygroscopicity and CCN activity of atmospheric Water Soluble Organic Carbon (WSOC) particulate matter isolated from filter samples taken during the IMPROVE studies and measured without the compounding effects of common, soluble inorganic aerosol constituents. Across all sampling locations and seasons, the hygroscopic growth of WSOC samples at 90% RH, expressed in terms of the hygroscopicity parameter, κ, ranged from 0.05 – 0.15. Comparisons between the hygroscopicity of WSOC and that of samples containing all soluble materials captured by the filters implied a significant modification of the hydration behavior of inorganic components, including decreased hysteresis separating efflorescence and deliquescence and enhanced water uptake between 30 and 70% RH. Together, the findings in this chapter that WSOC appreciably contributes to particle water and undermine the lack of consideration in the IMPROVE protocol.

[*] Parts of this chapter are adapted with permission from "Hygroscopic growth of water soluble organic carbon isolated from atmospheric aerosol collected at US national parks and Storm Peak Laboratory," by N.F. Taylor, D.R. Collins, D.H. Lowenthal, I.B. McCubbin, A.G. Hallar, V. Samburova, B. Zielinska, N. Kumar, and L.R. Mazzoleni, originally published in *Atmospheric Chemistry and Physics* in 2017 (vol. 17, pp 2555-2571). The article is fully available for re-use under the Creative Commons 3.0 license.

Background

Interactions with atmospheric water are central to the impacts of aerosols on human health (Vu et al., 2015), climate (Boucher et al., 2014) and visibility (Malm and Pitchford, 1997). The tendency of an aerosol to take up water in sub-saturated conditions—its hygroscopicity—directly affects its impact on climate and visibility by modifying the efficiency with which it scatters and absorbs radiation (Tang, 1996). The presence of an aqueous phase in an aerosol affects its aging in the atmosphere, generally increasing the uptake of reactive and soluble trace gases and enhancing aerosol growth (Herrmann et al., 2015; Carlton and Turpin, 2013), significantly impacting all of its atmospheric roles. Likewise, atmospheric aerosols play a critical role in earth's climate as cloud condensation nuclei (CCN) (Boucher et al., 2014), while cloud processing, in turn, may dramatically modify the size distribution and chemical composition of aerosols (Herrmann et al., 2015).

Water soluble organic carbon (WSOC) is well-known to constitute a major fraction of atmospheric aerosols. Measurements at various locations and seasons, including the measurements associated with this report, have shown WSOC to constitute from 20 to >90% of the total aerosol organic carbon (OC) (Du et al., 2014; Lowenthal et al., 2014; Anderson et al., 2008; Sullivan et al., 2004; Saxena and Hildemann, 1996). Atmospheric WSOC correlates strongly with secondary organic aerosol (SOA), but also has sources in primary biogenic aerosol such as pollen (Miyazaki et al., 2012) and that from biomass burning (Timonen et al., 2013). Sun et al. (2011) found that biogenic SOA (characterized by mass spectra) constituted ~75% of WSOC during the summer at

rural sites in the eastern U.S., while biomass burning-like aerosol dominated during winter months. Finally, studies applying dual-isotope, radiocarbon analysis to WSOC indicate that modern carbon predominates in WSOC, but that fossil-carbon in aerosols can also contribute significantly (~20% of WSOC) in polluted air masses (Kirillova et al., 2014; Kirillova et al., 2013; Miyazaki et al., 2012).

The atmospheric prevalence of WSOC anticipates a significant WSOC contribution to global, water-modulated aerosol impacts; yet assessing its impact is similarly challenging to modeling global SOA (Hallquist et al., 2009). Moreover, far fewer measurements of WSOC properties have been made to support such assessments and validate models than to support the efforts to assess global SOA. This report of ambient WSOC hygroscopicity and CCN activity, from a series of five, month-long studies at remote continental sites in the U.S., helps bridge the gap between WSOC prevalence and the impact of WSOC on ambient aerosol properties.

Most methods of analyzing atmospheric aerosol-phase WSOC begin with the collection of a bulk sample of soluble aerosol material either using a Particle-into-Liquid Sampler (PILS) or by extracting the soluble material from aerosol collected on filters (Psichoudaki and Pandis, 2013). Thus, the designation of organic material as water soluble has been called 'operational', defined by the method of dissolving the material (Psichoudaki and Pandis, 2013). These samples of Water Soluble aerosol Material (WSM) are frequently dominated by common inorganic compounds such as sulfate, nitrate, and ammonium. Extensive analysis of WSOC can be conducted on such mixtures. Total Organic Carbon (TOC) instruments can retrieve WSOC mass

concentration (Chow et al., 2004), and chemical speciation can be determined using a wide range of analytical instruments. The hygroscopicity and CCN activity of WSOC can then be inferred by measuring those properties for WSM and estimating the contribution of WSOC from chemical composition and the well-known behavior of soluble inorganic components (Cerully et al., 2015; Kristensen et al., 2012). Using this approach, Guo et al. (2015) reported an average contribution by WSOC of 35% to particulate water across several sites in the southeastern U.S. However, the calculations required to subtract the inorganic contribution introduces uncertainty due to the complexity of WSOC composition, limitations of chemical analysis, non-ideal mixtures, and multiplicity of aerosol phases (Hodas et al., 2015). Alternatively, the physical characteristics of purely organic, laboratory-generated aerosols are frequently measured (Frosch et al., 2013; Engelhart et al., 2011b; Frosch et al., 2011; Cruz and Pandis, 1997) to inform estimates of ambient WSOC properties and the mechanisms by which WSOC is formed. However, modeling is required to relate such data to ambient WSOC.

The measurements of WSOC hygroscopicity and CCN reported in this chapter rely on a third approach—isolating WSOC from the inorganic compounds in a WSM sample. Various methods of isolating WSOC exist, as reviewed by Duarte and Duarte (2011) and Sullivan and Weber (2006), capable of retaining from 50%–90% of sample WSOC with less than 5% retention of inorganic compounds. To the authors' knowledge, this approach to quantifying WSOC hydration properties has not been widely employed. Notable exceptions are Gysel et al. (2004); Asa-Awuku et al. (2008); and Suda et al. (2012). The earlier work, by Gysel et al. (2004) carried out a bulk

separation of organic matter from WSM extracts of filter-collected ambient aerosol. This isolated organic matter was then re-aerosolized and its hygroscopicity analyzed with a Tandem Differential Mobility Analyzer (TDMA). They reported hygroscopic growth factors, GF, from 1.08–1.17 at 90% relative humidity, RH, corresponding to a hygroscopicity parameter, κ (Petters and Kreidenweis, 2007), from ~0.03–0.08. Asa-Awuku et al. (2008) used similar methods not only to 'desalt' samples of biomass burning aerosol, but also to isolate hydrophilic and hydrophobic WSOC—all for the purpose of determining how each fraction impacted aerosol hygroscopic growth within a multi-parameter, Köhler-theory based framework. The approach of Suda et al. (2012) is quite dissimilar, with extracts from filter samples of smog chamber-produced aerosol fractionated by reversed-phase high-performance liquid chromatography (HPLC). The HPLC eluate was continuously atomized and analyzed using a Droplet Measurement Technologies CCN counter (CCNc). The approach described here bears many similarities to that of Gysel et al. (2004), but captured a larger fraction of the WSOC. Moreover, the present work is distinguished by its focus on connections between the solubilities of organic and inorganic compounds present in the same particles.

Study Details

This chapter reports measurements of the hygroscopicity and CCN activity of WSOC isolated from aerosol samples collected during a series of five, month-long field campaigns, as detailed in Table 4. The first four campaigns were part of a larger project focused on sources of visibility degradation in U.S. national parks. The measurements were designed to assess the contribution of WSOC to aerosol water content and the

resulting impact on visibility. These studies took place at Great Smoky Mountains (GRSM) National Park in eastern Tennessee during the summer of 2006 and fall-winter of 2007–08, and at Mount Rainier (MORA) and Acadia (ACAD) national parks during the summers of 2009 and 2011, as described in Chapter I. A similar study took place at Storm Peak Laboratory (SPL) near Steamboat Springs, Colorado, in the summer of 2010. SPL is situated on a high ridge in remote northwestern Colorado (40.455°N, 106.744°W, 3214 m asl); due to its elevation, SPL provides access to the free troposphere and is influenced by both local and distant sources (Hallar et al., 2013). The measurements of WSOC at SPL were part of a closure experiment attempting to estimate WSOC hygroscopicity from highly detailed chemical speciation and were variously reported by Hallar et al. (2013), Samburova et al. (2013), and Mazzoleni et al. (2012). This paper goes beyond those prior analyses to highlight the hydration behavior of ambient WSOC, especially the complementary enhancement of aerosol water uptake in internal mixtures of WSOC and common inorganic aerosol components.

Methodology

The analysis of WSOC for the five field studies reported here had three major steps: collection of daily, high volume, PM2.5 filter samples; laboratory-based isolation of WSM and WSOC; and analysis of the hygroscopicity and CCN activity of aerosol generated from those isolated fractions. We provide a brief synopsis of the steps but direct the reader elsewhere for detailed descriptions.

PM2.5 Filter Samples

PM2.5 filter samples were taken for one month during each of the five studies. Four high-volume (~1100 L/min) PM2.5 filter samplers were operated during each project, as described by Lowenthal et al. (2009). The filters were Teflon-impregnated glass fiber (TIGF) except during the first 12 days of the summer GRSM study, when Zefluor Teflon membrane filters were used. The filters were pre-cleaned by sonication in methanol and dichloromethane. The sample period was 24 hours. Filters were collected daily from each sampler during all projects and were kept refrigerated during storage and shipping after sampling and prior to analysis. Filters were typically processed within three months of the completion of the respective measurement campaign.

WSOC Sample Production

High molecular weight WSOC, referred to as Humic Acid-Like Substances (HULIS), was isolated from the filters as described in Lowenthal et al. (2009, 2015), following the method of Duarte and Duarte (2005). First, WSM was extracted from each daily set of 4 high-volume filters by sonication in 250 mL of ultrapure water. The WSM solution was passed through a PTFE membrane filter and then concentrated to 15–20 mL using a rotovap under gentle vacuum. WSOC was then isolated from the WSM using XAD-8 and XAD-4 macro-porous resins/chromatography columns: the WSM was acidified and applied to the XAD-8 and XAD-4 columns in series, the columns were rinsed with ultrapure water to remove inorganic material, and the WSOC was eluted from the columns using a mixture of water and methanol. The WSOC eluate was then concentrated by drying and combined with filter extracts from other days to produce

sufficient samples for hygroscopicity and CCN activity analysis. After concentration and combination of consecutive daily samples, 5–8 samples of isolated WSOC material remained for each month-long study. The filter sampling days associated with each sample are given in the data supplement.

Extraction with two resins, rather than one, increased the molecular weight range of retained WSOC components. XAD-8 material is traditionally used to isolate humic-like, high molecular weight substances while the XAD-4 column has been demonstrated to retain lower molecular weight, hydrophilic organic compounds. The use of XAD-4 likely resulted in more complete and representative WSOC extracts when compared with single column approaches. However, a significant fraction of lower molecular weight organic acids, sugars, and alcohols—likely more hygroscopic than HULIS—were not retained by either XAD column (Samburova et al., 2013).

Chemical analyses of inorganic ions and OC were conducted at various stages of the extraction process. Filter captured sulfate, nitrate, and chloride were measured using ion chromatography (IC) (Dionex DX 3000); ammonium was measured using automated colorimetry (Astoria 301A analyzer) (Lowenthal et al. 2009; Samburova et al., 2013). Similar IC and colorimetry measurements were conducted on the extracts (Lowenthal et. al 2009) and to determine the "sulfate cleaning efficiency" reported in Table 1. Filter and extract OC and organic mass (OM) were determined using thermo-optical reflectance (TOR) (Chow et al., 2004) and/or total organic carbon (TOC) (OI Analytical Aurora 1030W TOC Analyzer) methods, which showed good agreement (Lowenthal et al., 2015). During the SPL study, dissolved WSOC was measured using only TOC

(Shimadzu Model TOC-VCSH). During the four national park studies, measurement uncertainties for OC, sulfate, nitrate, and ammonium were 12, 5, 26, and 5% (Lowenthal et al., 2015). The OM to OC ratio was evaluated by depositing and drying isolated WSOC sample material on pre-fired quartz filter punches, and combining TOR carbon analysis with before-and-after measurements of the punch mass; a standard value of 1.8 was employed during all studies except SPL, for which 2.1 was assumed. The performance of the WSOC extraction, summarized as WSOC Recovery in Table 4, was evaluated by before-and-after measurements of dissolved OC (Lowenthal et al. 2009). More extensive chemical analysis was conducted on the extracts from samples collected during the SPL project, including detailed speciation of WSOC and IC measurements of crustal ions (using a Dionex CS16 column) in WSM samples (Samburova et al., 2013).

Table 4: WSOC project summaries.

	GRSM Summer	GRSM Winter	MORA	SPL	ACAD
Sample period	7/19/2006 –8/17/2006	1/11/2008 –2/9/2008	8/1/2009 –8/30/2009	6/24/2010 –7/28/2010	8/1/2011 –8/30/2011
WSOC/OC	22%	21%	77%	89%	93%
Sulfate cleaning efficiency	99.7%	99.2%	99.8%	97.7%	99.8%
Std. Dev.	0.3%	0.2%	0.2%	2.2%	0.2%
WSOC Recovery	46%	100%	90%	73%	60%
Std. Dev.	22%	17%	13%	17%	70%
WSOC ($\mu g \cdot C \cdot m^{-3}$)	0.64	0.22	1.41	0.72	0.78
PM2.5 Reconstructed ($ng \cdot C \cdot m^{-3}$)	16.2	5.3	5.0	2.3	3.1

WSOC Hygroscopicity and CCN Activity Analysis

The hygroscopicity and CCN activity of the prepared samples from each study were evaluated within several months of their extraction. The samples were continuously refrigerated, which effectively preserved their properties. A remnant of a GRSM Summer sample was re-analyzed alongside the GRSM Winter samples over a year after its first analysis and showed little change in hygroscopicity. WSOC hygroscopicity analysis was conducted using a TDMA largely identical to that described by Gasparini et al. (2006), configured as depicted in Fig. 24. CCN activity was measured using the same TDMA, operating as a Scanning Mobility Particle Sizer (SMPS), paired with a DMT CCN-100 counter (CCNc) in the configuration described by Frank et al. (2006).

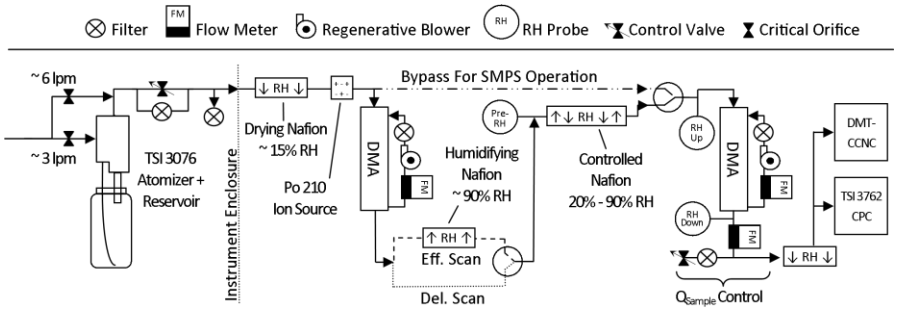

Figure 24: TDMA and SMPS-CCNc configuration.

Sample aerosol generation

The isolated WSOC samples were aerosolized using a TSI 3076 atomizer configured to recirculate overspray. Several precautions were necessary due to the limited sample material available (~5 mg dissolved in ~15 mL of water). First, because

the atomizer consumed ~45 mL of sample solution over the course of the RH-scanning TDMA measurements (~3 h) and the SMPS-CCNc measurements (~1.5 h), it was necessary to dilute the ~15 mL samples with ~40 mL of ultrapure water. These very dilute samples were susceptible to contamination from residues in the atomizer assembly and soluble gases in the compressed air stream. To minimize contamination, the atomizer assembly and reservoir were thoroughly purged with ultrapure water between measurements and with particular care following its use with ammonium sulfate for instrument calibration. Further, the compressed air stream was scrubbed using a HEPA filter and canisters containing silica gel desiccant and activated carbon. Contamination was assessed by contrasting the size distribution produced by the atomizer with and without the extracts. Under consistent conditions, the atomizer will produce a consistent droplet size distribution. The resultant dry particle size distribution reflects the concentration of solute in those droplets; a thousand-fold increase in the dissolved concentration of the atomizer solution translates to a ten-fold shift in the diameter of particles produced. Before each sample was placed into the atomizer, the particle size distribution produced from atomizing ultrapure water was checked to ensure it was roughly 1000 times less concentrated than the sample solution and remained consistent for ~30 minutes. The atomizer was re-cleaned if it failed this test.

TDMA and SMPS-CCNc operation

The hygroscopicity of each sample was evaluated in two sets of TDMA measurements: a series to detect the deliquescence of an initially desiccated (~15% RH) aerosol and a series to detect the efflorescence of an initially hydrated (RH ~90%)

aerosol. In both, the first DMA column was operated to select dry particles with electrical mobility diameter of 0.07 μm, roughly corresponding to the peak in number concentration of the dried atomizer-generated aerosol. The second DMA column was operated in conjunction with the condensation particle counter (CPC) as a traditional SMPS, capturing the response of this roughly monodisperse aerosol to the humidification and drying processes occurring between the two DMA columns at ~90s intervals. During the first series—the "pre-desiccated" or "deliquescence" scan—the dry, monodisperse aerosol bypassed the humidifying Perma Pure PD-Series Nafion tube bundle as depicted in Fig. 24. The aerosol was next directed through the RH controlled Nafion tube bundle, which was used to track a gradually descending RH setpoint from ~90% to ~25% RH over the course of ~90 minutes. Thus, this configuration mapped the hygroscopic growth response of an initially desiccated aerosol to capture deliquescence behavior. The second series—the "pre-hydrated" or "efflorescence" scan—mapped the hygroscopic growth of an initially hydrated aerosol to detect distinct efflorescence transitions and meta-stable hydration states. During the second series, the monodisperse aerosol passed through the humidifying Nafion tube bundle, while the controlled Nafion tracked an RH setpoint that gradually increased from ~25% to ~90% RH.

Each series of TDMA measurements resulted in a series of distributions in which the location (representing hydrated particle size) of a single, narrow mode reflected the hygroscopic growth of the sample. Each distribution was condensed to a single parameter, growth factor, or GF(RH), which is the ratio of the particle size detected by the second DMA/CPC to the dry particle diameter selected in the first DMA column

(here 0.07 μm). The basic GF(RH) curves for each sample from each study are included in the data supplement. Growth factor is an intuitive metric of hygroscopicity, but we primarily discuss these results using the hygroscopicity parameterization, κ(RH), of Petters and Kreidenweis (2007). GF(RH) translates directly into κ(RH).

(Eq. 4)

$$\kappa(\mathrm{RH}) = ([GF(RH)]^3 - 1)\frac{\left(\exp\left(\frac{A}{GF(RH)\cdot D_p}\right) - RH\right)}{RH}$$

(Eq. 5)

$$A = \frac{4 \cdot \sigma_{s/a} \cdot MW_{water}}{R \cdot T \cdot \rho_{water}}$$

Here, σs/a is assumed equal to 0.072 J·m-2, the surface tension of pure water. Dp, the dry diameter, is chosen to reflect the minimum measured over the range in RH, rather than the size selected by the first DMA column (0.07 μm), to correct for a measurement artifact described in the shape factor discussion in the last section. These particles are assumed to be spherical. Among the advantages of κ(RH) is that it is more closely a bulk property of the material; for an ideal solution, κ(RH) is independent of RH and proportional to the molecular volume of the solute.

The CPC count array was inverted with respect to the second DMA only; the resulting distributions retained the natural breadth and multiply charged particles contribution from the aerosol population selected by the first DMA. Neither significantly impacts the results. The relative concentration of multiply charged particles is expected to be relatively low, as the generated aerosol distribution was quite

narrow and the selected size near its peak. Furthermore, the composition of the generated aerosol was not dependent on particle size and the only difference between the GF of singly and multiply charged particles is due to the differing magnitude of the curvature effect. For these experiments, the only parameter of interest was the peak diameter of the resultant size distribution, not its breadth. But the distributions were narrow and well-resolved, driven by the TDMA's sheath-to-sample flow ratio of 10:1 (30 vs. 3 l·min-1).

CCN activity of aerosol samples from MORA, ACAD, and SPL was analyzed using a DMT-CCNc operated at four fixed supersaturations (nominally 0.2, 0.4, 0.6 and 0.8%) in parallel with the CPC of the TDMA while operating the TDMA as an SMPS. SMPS-CCNc measurements produce two particle size distributions: a conventional distribution based on the response from the CPC and a distribution of the particles that activate in the CCNc. For an internally mixed aerosol, such as the atomizer-generated aerosol measured here, the ratio of the size-dependent concentrations from these two distributions appears as a sigmoidal function that steps from 0 to 1 with increasing particle size. That is, at sizes below the critical activation diameter of the aerosol for the set supersaturation, the CCNc size distribution is zero; above the aerosol's activation diameter the CCN and CCNc distributions are identical. The mid-point of the transition between these regimes (Dp50%) corresponds to the critical dry diameter for CCN activation at the set CCNc supersaturation. These results are typically reported as Dp50%(SSC) as in Fig. 25, where SSC is the aerosol critical supersaturation expressed

as a percentage. Dp50%(SSC) also translates into κ(SSC), which is comparable to κ(RH) (Petters and Kreidenweis, 2013) , as in Fig. 26.

(Eq. 6)

$$\kappa(SS_C) = \frac{4A^3}{27 \cdot \left[D_p 50\%(SS_C)\right]^3 \cdot ln^2(SS_C + 1)}$$

This equation is an approximation of κ(SSC), slightly overestimating (~5%) where κ(SSC)<0.2. It is retained for its consistency with other studies. A is given in Eq. 5 above.

Both instruments were calibrated at the outset of each study and least once more over the course of measurements (~10 days). The critical sizing parameters of the TDMA, the flow meters and high voltage sources, were calibrated directly using a Sensidyne Gilibrator and Fluke multimeter. The RH sensors and CCNc performance were calibrated using the instruments' response to an atomized ammonium sulfate aerosol. The uncertainty associated with TDMA and SMPS-CCNc measurements is primarily driven by uncertainty in RH and supersaturation, respectively. RH was measured using Vaisala HMM-22D RH probes, which have a manufacturer reported accuracy of ±2-3%. The precision of CCNc supersaturation has been reported to range from ±1-5% depending on the stability of ambient conditions and time period (Rose et al., 2008). The uncertainty associated with particle sizing by the TDMA/SMPS instrument, linked to the sheath flow rate measurement (±1%) and high voltage supply (±0.5% for the relevant voltage range), is lower, near ±0.001 μm at 0.070 μm.

Additional uncertainty arises from the possibility of irregularly shaped aerosol. Shape factor, the ratio between TDMA-relevant particle mobility diameter and particle volume-equivalent diameter, is used to correct for the depressed mobility of irregularly shaped particles and commonly ranges from 1.02 for ammonium sulfate to 1.08 for cubic sodium chloride to 1.24 for irregularly formed sodium chloride (Wang et al., 2010). Calculations of κ(RH) are very sensitive to shape factor at low RH: an uncertainty of ±0.03 in shape factor can translate to >50% uncertainty in κ(RH) at low RH but <5% at high RH. No independent recoveries of shape factor, such as SEM micrographs, were made during these studies to constrain this uncertainty. Some confidence can be gained from the continuity between measurements before and after the particles dissolve (and become spherical)—which is detected at low RH for all WSOC samples.

Results and Discussion

WSOC comprised 22–93% of the PM2.5 organic carbon during these studies, with 46–100% recovered in the WSOC isolation process. Isolated WSOC was characterized by hygroscopicity parameters (κ) ranging from ~0.05–0.15 calculated from the GF at 90% RH. In addition to direct contribution to particle water uptake, WSOC appeared to complement the water uptake of inorganic compounds in WSM samples. Finally, measurements of samples from the GRSM Winter and SPL studies implied that atomizer-generated WSOC particles may assume complex morphologies.

Filter Samples and WSOC Extracts

As presented in Table 4, WSOC concentration ranged from 0.22 to 1.41 μg·C·m-3. The lowest concentration, unsurprisingly, was during the sole winter study (GRSM

Winter); otherwise, WSOC varied much more narrowly than reconstructed PM2.5. (PM2.5 was not measured, but Lowenthal et al. (2015) found the sum of measured constituents (SO4, NO3, etc.) reasonably duplicated PM2.5 measurements by co-located IMPROVE network samplers.) For all studies, the WSOC isolation procedure effectively removed sulfate. During the four national park studies, the cleaning efficiency was slightly higher, reflecting a slightly different methodology. For those projects, the samples were reprocessed until the reduction in sulfate reached 99%, likely reducing the fraction of WSOC retained. The Storm Peak Lab samples were only processed once, to maximize WSOC retention.

Seasonal and Locational Variation in WSOC Hygroscopicity

Figure 25 shows the results of analysis of the samples collected during the five projects. The pre-desiccated hygroscopic growth curves for each measurement are omitted for clarity, and the scans are normalized with respect to their minimum GF according to the discussion of shape factor in the final section. As reported by Lowenthal et al. (2015), these measurements indicate significant hygroscopic growth of the WSOC aerosol, and a sizable contribution to particulate water.

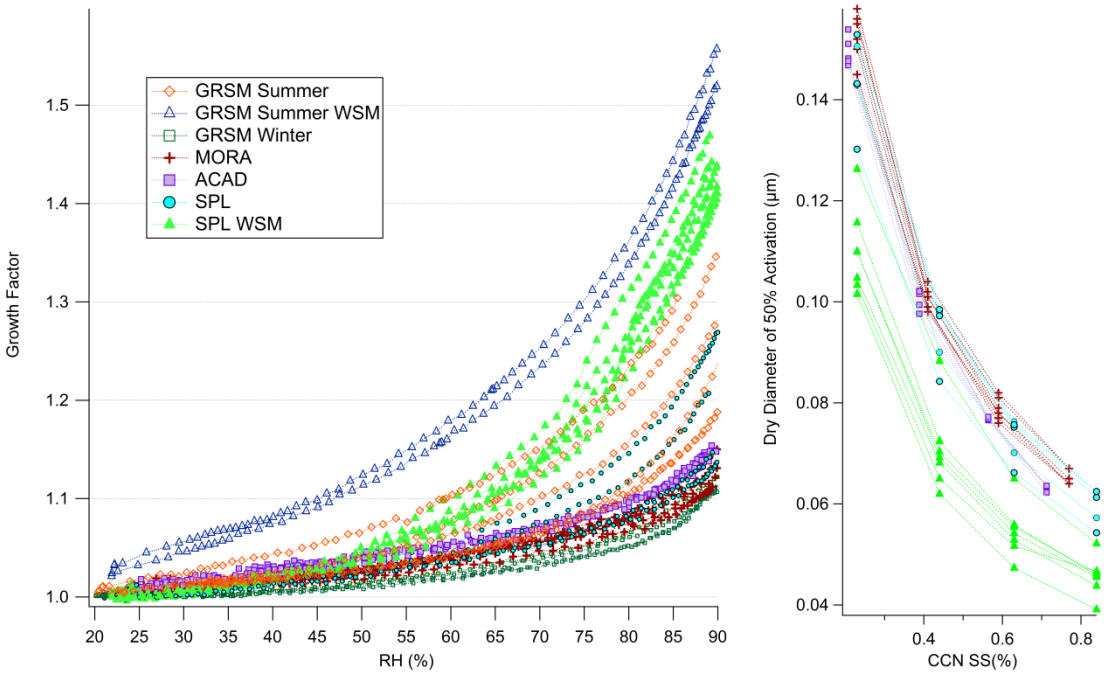

Figure 25: Hygroscopic growth curves for initially hydrated aerosol samples (designed to detect efflorescence) and CCN activity results. CCN measurements were conducted only on MORA, ACAD, and SPL samples (both WSM and WSOC).

The measured hygroscopic growth varied little among the samples from each study, but contrasts were apparent between studies. The least hygroscopic samples were taken at GRSM during the only winter study, likely indicating a smaller relative contribution from highly oxidized, lower molecular weight WSOC. This is consistent with the seasonal cycle of WSOC characteristics measured by Miyazaki et al. (2012) in a deciduous forest in Japan, which indicated low molecular weight, isoprene-derived WSOC only during summer months.

The differences in hygroscopicity among the samples collected during the summer studies could have various causes. GRSM samples were most hygroscopic. That site is characterized by being more polluted with much higher particulate mass

loading, by deciduous (rather than coniferous) forest, and by being the southernmost site. From these characteristics, higher levels of isoprene, a more oxidative environment, and greater availability of aqueous aerosol for WSOC partitioning could be expected, all of which could contribute to WSOC dominated by lower molecular weight, highly oxidized species. Recent studies, e.g., Carlton and Turpin (2013), have emphasized the role of 'anthropogenic' particle water in biogenic SOA formation, especially in the eastern United States.

In Fig. 26, the hygroscopic growth and CCN activity measurements from each study have been recast in terms of κ, to illustrate the consistency between hydration behavior at high RH and that for supersaturated conditions. The lines are study averages; the error bars indicate the standard deviation of those averaged measurements. In general, there is close agreement between hygroscopic growth at high RH and CCN activity estimates of κ. Somewhat surprisingly, the largest deviation is lower CCN activity-derived κ for the SPL WSM samples: the potential for droplet surface tension depression (leading to enhanced CCN inferred κ) by surface active organics can be enhanced in mixtures with inorganic ions such as in the WSM (Asa-Awuku et al., 2008).

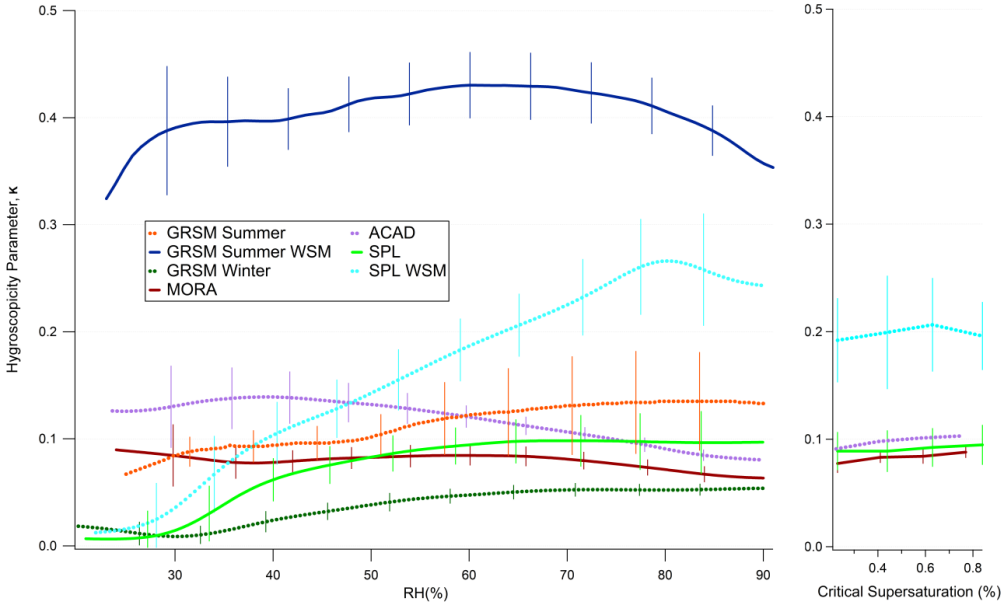

Figure 26: Average κ(RH) and κ(SSc) from all initially hydrated hygroscopicity measurements for all WSOC and WSM samples. Whiskers indicate the standard deviation between samples from each study.

The shape of these κ(RH) curves indicates that WSOC behaves somewhat differently than an ideal, aqueous aerosol. Neglecting the influence of surface tension, κ(RH) for an ideal, fully aqueous aerosol is relatively constant and determined by relative molecular weights and densities of the solute and solvent (water). We rationalize minor deviations in the shapes of these κ(RH) curves as non-ideal solution behavior, and abrupt deviations as changes in aerosol phase. In particular, an abrupt decrease in κ(RH) with decreasing RH in measurements of an initially hydrated aerosol can indicate efflorescence. One caveat to κ(RH) inferred from hygroscopic growth, especially at low RH, is sensitivity to aerosol shape. When the shape is known, a corrective term—shape factor—is used to adjust the measured mobility diameter to a volume-equivalent diameter (e.g., cube-shaped, crystalline sodium chloride has the

mobility of a spherical particle with 1.08 times its volume) (Wang et al., 2010; Zelenyuk et al., 2006). Here, particles are assumed to be spherical, having a shape factor of 1, with the notable exception discussed in Sect. 3.6 below. Thus, as κ(RH) for most WSOC samples is fairly constant from 40% RH through CCN activation, it is assumed that the soluble components in these particles are entirely dissolved in that range. However, at low RH, κ(RH) for the SPL and MORA WSOC samples climbs from near zero to ~0.1, indicating a distinct deliquescence point (DRH). Neglecting curvature effects, DRH relates to solubility as it is the RH over a solute-saturated solution. This suggests that the solubility of these samples limits the existence of an aqueous phase to RH >30%, i.e., when the activity of the aerosol-phase water is greater than ~0.3. For WSOC collected during the GRSM Winter project, κ(RH) also increases with increasing RH, but the change is less abrupt. With the remaining WSOC samples there is little change in κ(RH) over the full RH range, suggesting lower, undetected DRH and higher solubility. The κ(RH) of WSM samples tends to increase with RH, especially for samples taken at SPL. Because Fig. 26 shows the behavior of initially hydrated particles, these κ(RH) curves indicate that some species that make up the WSM gradually leave the aqueous solution as RH decreases. Together with the WSOC measurements, this implies a complementary effect between WSOC and inorganic aerosol material, which is discussed in the next section.

Complementary Enhancement of Water Uptake by Mixtures of WSOC and Inorganic Ions

During two projects, the summers at GRSM and SPL, samples of both ambient WSOC and ambient WSM were isolated and analyzed (only WSOC samples were analyzed for the remaining three projects). In addition to the compounds retained in the WSOC sample, the WSM samples contained all water soluble inorganic and organic material not retained by the WSOC extraction. The hygroscopic growth of these materials indicates that mixtures of WSOC and soluble, inorganic compounds can uptake significantly more water than their individual hygroscopicities would predict. This result is not unanticipated as it is well known that the efflorescence/deliquescence behavior of inorganic salts is modified by the presence of WSOC (Smith et al., 2012; Marcolli et al., 2004; Brooks et al., 2002; Hansson et al., 1998) and that the deliquescence point of an internal mixture of inorganic salts is generally lower than the deliquescence points of the individual compounds (Zardini et al., 2008; Ansari and Pandis, 1999). However, the isolation and analysis of atmospheric WSOC and WSM in the present study provides a unique perspective on these effects in complex, atmospherically representative mixtures.

To evaluate the significance of this complementary effect, the measured WSM hygroscopicity for the SPL and GRSM Summer samples is contrasted with a modeled prediction of WSM hygroscopicity that assumes no interaction between the organic and inorganic fractions—a ZSR-like estimate. Particularly for samples from SPL, this prediction consistently underestimated water uptake by WSM at RH between 30 and

70%, as illustrated in Fig. 27, which suggests that interactions between the inorganic and organic fractions enhance water uptake. As is explored below, this enhancement is linked to the RH at which the inorganic PM dissolves.

Table 5: Concentration ($ng \cdot m^{-3}$) of Inorganic Ions, Organic Carbon, and Organic Mass in WSM Extracts.

Storm Peak Lab WSM Samples*					
Sample Number	1	2	3	4	6
Na^+	6.5	2	11	8.9	6.4
SO_4^{2-}	544	330 (449)	452	77 (488)	242
NH_4^+	85	58 (80)	41	66 (112)	33
NO_3^-	83	83 (105)	137	126 (124)	50
Cl^-	4.4	4.3	2.6	5.6	0.4
Ca^{2+}	28	27	27	33	33
K^+	42	46	54	44	29
Mg^{2+}	5	4.6	6	7	2.2
Total Inorganic Ions	797	555 (718)	730	368 (810)	396
WSOC ($ng \cdot C \cdot m^{-3}$)	525	1,932	601	596	490
WSOC Recovery (%)	55	87	81	92	52
WSOM (x2.1)	1,070	3,940 (1,390)	1,226	1,220	999

GRSM Summer WSM Samples**		
Sample Number	4	6
$SO4_4^{2-}$	13,200	12,000
NH_4^+	2,580	1,950
$NO_3^{-\dagger}$	---	---
Total Inorganic Ions	15,800	14,000
WSOC ($ng \cdot C \cdot m^{-3}$)	1,640	533
WSOC Recovery (%)††	---	---
WSOM (x1.8)	2,950	960

*Direct analysis of SPL samples was performed and reported by Samburova et al. (2013). Values in parenthesis were inferred from concurrent daily PM2.5 filter analysis reported by Hallar et al. (2013).
**WSM composition was not reported for GRSM Summer. The given values are inferred from concurrent daily PM2.5 filter analysis performed and reported by Lowenthal et al. (2009).
†Daily nitrate was not reported; Lowenthal et al. (2009) indicated that 50 ng/m^3 was typical during this study.
††Daily WSOC Recovery was not reported for these samples; Lowenthal et al. (2009) indicated an average WSOC Recovery of 46% for GRSM Summer.

Storm Peak Lab: Enhanced Water Uptake Driven by Low-DRH WSOC

Enhanced water uptake is most clearly demonstrated in the results from Storm Peak Laboratory in remote northern Colorado. Primarily this is because the SPL study involved more detailed chemical analysis as well as a full set of complementary WSM and WSOC samples. As noted above, the enhancement of water uptake is shown by contrasting the measured WSM hygroscopic growth with a prediction of WSM hygroscopic growth based upon the independent contribution of WSOC and inorganic components assuming no interaction. This prediction is based on the measured WSOC hygroscopicity and the inorganic hygroscopicity estimated from the measured composition.

Modeling the hygroscopic properties from the available SPL inorganic composition was done using the E-AIM thermodynamic model (Clegg and Brimblecombe, 2005; Clegg et al., 1998a, b) and presented several challenges. First, E-AIM does not treat K+, Mg2+, and Ca2+. However, it does treat multiple solid phases, including hydrates. Critically, it appears to handle the addition of nitrate more realistically than other models. The untreated cations K+ and Mg2+ were included in the model input as charge equivalent Na+, while Ca2+ was assumed to remove one sulfate ion to form CaSO4 or gypsum, both of which are relatively insoluble, only expected to dissolve at high RH, and not expected to impact the relevant deliquescence transitions.

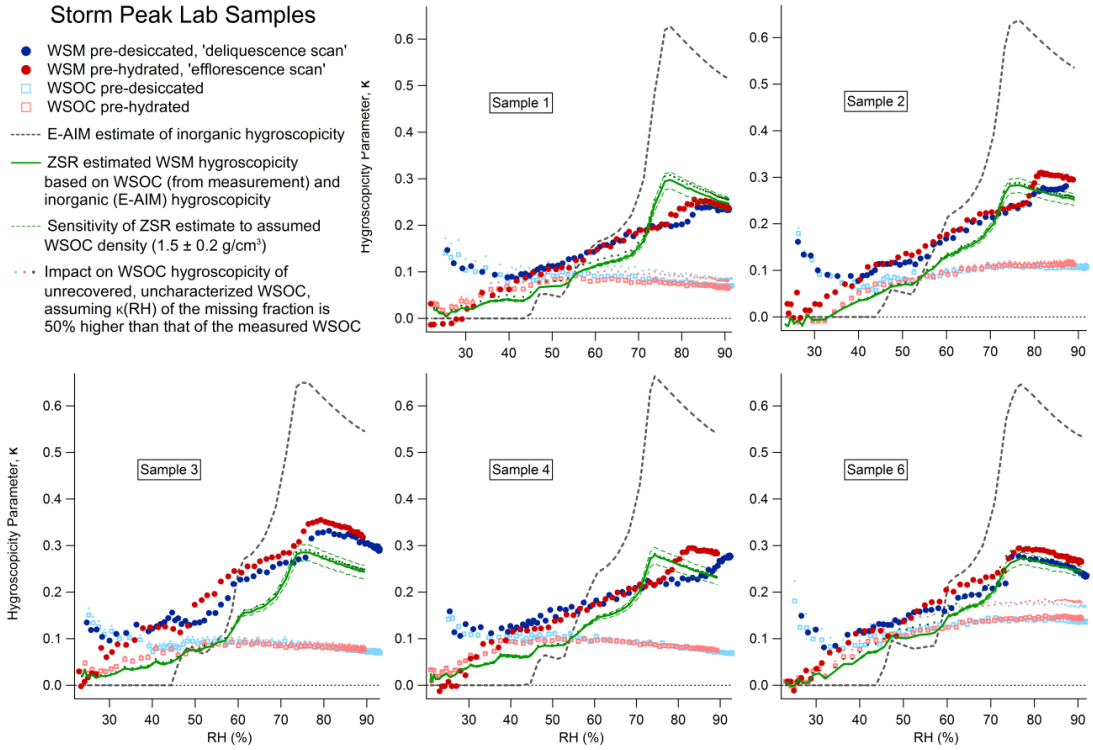

Figure 27: Comparison of the measured hygroscopicity of SPL WSM samples to expected WSM hygroscopicity assuming no interaction between the organic and inorganic components. WSM hygroscopicity (in green) was estimated from independent assessments of the hygroscopicity of the organic fraction (from WSOC measurements) and of the inorganic fraction (predicted from composition using the E-AIM model). For each sample, WSM hygroscopicity is underestimated below 70% RH, driven by the expectation of the model that the majority of the inorganic fraction will not dissolve until RH reaches ~70%. This suggests that WSOC can significantly depress inorganic DRH, enhancing water uptake below 70% RH.

A second issue is that that the inorganic anions and cations for these samples do not balance (Hallar et al., 2013). In very similar analysis of WSM and WSOC, Gysel et al. (2004) assumed that a negative ion balance was simply offset with protons. For various reasons, we more closely followed the approach of Hallar et al. (2013) and assumed that the missing cations are ammonium. This approach was chosen largely because the samples all contained significant nitrate which does not typically exist in the aerosol phase with acidic, un-neutralized sulfate (Fountoukis and Nenes, 2007). The

cations in the available composition data are insufficient to neutralize the detected sulfate (the average ammonium to sulfate ratio is ~0.93). Moreover, assuming a more acidic aerosol would overestimate the hygroscopic growth. κ(RH) for ammonium bisulfate, with a molar ratio of ammonium to sulfate of one, is almost 0.8 at 50% RH, much higher than is indicated by the WSM samples. Similarly, each WSM sample exhibits an abrupt increase in κ(RH) near 80%, which appears to correspond to the deliquescence of the inorganic fraction, but is inconsistent with the acidic mixtures the ammonium to sulfate ratios indicate (DRH of ammonium bisulfate is ~40% RH). The E-AIM results, given as solute mass in and out of solution, were translated into κ(RH) using the density model of Clegg and Wexler (2011a, b) and are depicted by the dashed lines in Fig 27.

The green curves in Fig. 27 show WSM hygroscopicity as predicted from the independent hygroscopicity of the organic (measured) and inorganic (modeled) fraction of each sample by simply taking the dry solute volume-weighted average of the independent κ(RH) (Petters and Kreidenweis, 2007). While the dry solute volume of the inorganic fraction can be accurately calculated from the known mass and modeled density, no density information is available for the WSOC. We assume a value of 1.5 g·cm-3, but also show that the results are relatively insensitive to this assumption by including the results when assuming 1.3 and 1.7 g·cm-3 for contrast. A second minor assumption is that the measured WSOC properties are representative of all the WSOC present in the WSM samples. Other analyses of the SPL samples have indicated that un-extracted WSOC was characterized by relatively lower molecular weight (Hallar et al.,

2013; Samburova et al., 2013), which in an ideal mixture would cause greater hygroscopic growth. However, the impact here is expected to be limited; as shown in Table 5, unrecovered WSOC is a minor fraction. Figure 4 shows the result of assuming that the κ(RH) of the unanalyzed WSOC is 1.5 times that of the analyzed fraction, constraining the likely impact of WSOC not retained by the isolation process. The uncertainty in WSOC density and unanalyzed WSOC is minor and does not appear to account for the enhancement in water uptake by mixed aerosol.

A final note should be made concerning the composition data relied on for this analysis. For Samples 2 and 4, the reported concentrations of inorganic compounds derived from direct analysis of the samples were not consistent with concurrent daily filter-based PM2.5 composition measurements and produced unrealistic predicted WSM hygroscopicity. For this analysis, the relative prevalence of inorganic compounds for those samples was derived from the daily measurements. For Sample 2, the relative abundance of WSOC was also inferred. In inferring composition, no attempt was made to correct for filter sampling artifacts, such as adsorption of OC, reported by Lowenthal et al. (2009). The potential underestimation is expected to be minor and not impact the overall conclusion.

The measured WSOC hygroscopicity, modeled inorganic component hygroscopicity, and measured and estimated WSM hygroscopicity for each sample from SPL are shown in Fig. 27. As described in Tables 1 and 2, PM2.5 collected during the SPL study was predominantly organic, with an average WSOC to OC ratio of 89%. Each WSOC sample fully deliquesced at RH between 25 and 35%, above which κ(RH)

remains fairly constant near 0.1. The potential impact of the un-recovered WSOC, assuming it has a κ 50% higher than that recovered, is indicated by the smaller markers above each WSOC data point. Apart from Sample 6, for which the unrecovered fraction was large and κ(RH) relatively high, the impact is minor. At low RH, SPL samples exhibit a behavior shared by those from the GRSM Winter study, as well as by the WSOC studied by Gysel et al. (2004): the pre-desiccated measurement-based κ(RH) climbs steeply with decreasing RH while that based on the pre-hydrated measurements converge to zero. The final section discusses this further, suggesting that it is a measurement artifact related to generated particle morphology. For the purposes of this discussion we assume that, at low RH, the pre-hydrated measurements are representative of the actual deliquescence properties of the samples.

The inorganic soluble material in SPL WSM samples was dominated by a mixture of sulfate (54% of inorganic mass averaged across samples), nitrate (18%), and ammonium (11%), with minor fractions of Cl- (<1%), K+ (8%), Na+ (1%), Mg2+ (1%), and Ca2+ (6%) (Hallar et al., 2013). The hygroscopic growth of the inorganic fraction estimated using the E-AIM model was fairly consistent from sample to sample, characterized by gradual deliquescence from 45-75% RH. The gradual dissolution predicted by E-AIM is punctuated by the formation of several hydrates and minor salts, but dominated by ammonium sulfate. The model predicts that ammonium sulfate will dissolve gradually below its pure DRH as a solution containing other ions is a more effective solvent (Marcolli et al., 2004). In each sample, the inorganic components are predicted to fully dissolve at RH > 75%.

Measured WSM hygroscopicity of each sample indicates gradual dissolution from 30-80% RH, with a small but abrupt increase around 80%. In Samples 1, 2, and 4, this transition is associated with a small hysteresis loop, which suggests the existence of an ordered, crystalline phase (Martin, 2000). Apart from this small hysteresis loop, there is little difference between the pre-desiccated and pre-hydrated measurements and dissolution and formation of solids appears reversible. Because the WSOC measurements indicate that it will be dissolved above 30% RH and because WSOC cannot account for κ(RH) above ~0.07 (κ(RH)WSOC reduced in proportion to WSOC contribution to dry particle volume), the gradual dissolution can be attributed to the inorganic fraction. However, based on the expected deliquescence profile of the inorganic fraction predicted using E-AIM, this dissolution should not take place at all below 45% RH, and should not contribute significantly until ~60% RH. The impact of this shift in the deliquescence RH of the inorganic fraction of the WSM samples is evident in the contrast between the predicted and measured WSM hygroscopicity. Near 90% RH, where both the predicted and measured WSM κ(RH) of most samples have plateaued indicating that all solutes are dissolved, there is reasonably good agreement between them, given the uncertainties involved. The observed difference is most likely due to error in the measured relative abundance of inorganic and organic compounds, which determines the relative weight of the inorganic and organic hygroscopicities. Errors in WSOC and inorganic hygroscopicity would need to be unrealistically large to close the gap; in Sample 3 for example, κ(RH) of the inorganic fraction would need to peak above 0.85. More relevant to this discussion are the errors in the deliquescence

profile at lower RH. First, there is some inconsistency in the point at which κ(RH) plateaus and all solutes have dissolved. The model captures the profiles of Samples 2 and 3, but predicts full dissolution at too low RH for the other three samples. For all samples, however, the model generally predicts deliquescence at much higher RH than is evident from the measured WSM profiles. This behavior is consistent with the expectation that DRH is depressed in mixtures (e.g., Marcolli et al., 2004). This trend is even evident near the DRH of WSOC. Because no part of the inorganic fraction is expected to be dissolved below 45% RH, the expected WSM hygroscopicity profile is below even the WSOC curve. Yet κ(RH) of the measured WSM is consistently higher than WSOC at low RH. For Sample 2, the measured onset of dissolution of WSM is even lower than that of WSOC.

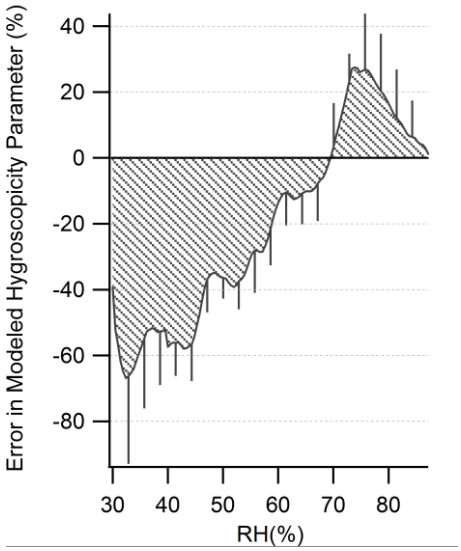

Figure 28: Average error in predicted WSM κ(RH). Error is defined as (κ(RH)predicted - κ(RH)measured)/ κ(RH)measured. Whiskers depict the standard deviation of error among the five samples.

These results indicate that the hydration behavior of complex, internally mixed aerosol may deviate significantly from that expected based on its major inorganic constituents. The average error of the expected vs. measured WSM hygroscopicity of samples from SPL, shown in Fig. 28, indicates that at low RH the measured κ(RH) for WSM is on average twice that expected. This roughly corresponds to a doubling of aerosol water. This behavior is rationalized by depressed DRH of compounds in mixtures (Smith et al., 2012; Wu et al., 2011; Marcolli et al., 2004; Brooks et al., 2002; Choi and Chan, 2002; Cruz and Pandis, 2000; Hansson et al., 1998). The impact of this behavior is likely widespread as highly soluble, low-DRH WSOC was ubiquitous during these studies. In all SPL WSM samples hysteresis was limited, despite the general expectation that sulfate-nitrate-ammonium aerosols have distinct crystalline and metastable states. Some studies have suggested that mixtures of WSOC and inorganic salts form amorphous, rather than crystalline, phases as they are dried (Mikhailov et al., 2009). The data from our studies are insufficient to do more than speculate. What is clear is that hysteresis is much less consequential in these mixtures with WSOC and that inorganic compounds can be expected to contribute more to aerosol water in the presence of low-DRH WSOC. The atmospheric impact of this behavior could be significant in dry climates where crystalline aerosol would otherwise form.

GRSM Summer: Mixtures Dominated by Acidic Sulfate

Only two other WSM samples, corresponding to GRSM Summer Samples 4 and 6, were produced and analyzed as part of these studies. Unlike the SPL study, composition had to be inferred from simultaneous daily filter measurements. The

GRSM Summer aerosol was also quite distinct from that at SPL. It was dominated by sulfate (9.0 µg·m-3) that was not fully neutralized by the available ammonium (1.9 µg·m-3). While organic mass was relatively abundant (5.2 µg·m-3), only 24% was soluble.

The differences between predicted and measured WSM hygroscopicity for these samples, shown in Fig. 29, may stem from uncertainties in inferred composition. Measured WSM hygroscopicity is much lower than predicted. For both samples closure is possible by assuming the concentration of WSOC is 6.5 times that measured (an average of 7.1 µg·C·m-3 instead of 1.1 µg·C·m-3). Closure cannot be achieved by assuming realistic changes in the WSOC or inorganic hygroscopicity (i.e., WSOC hygroscopicity is unlikely to be negative). And only a small percentage (~5%) of WSOC hygroscopicity can be attributed to the lower sulfate cleaning efficiency for GRSM Summer samples. Because composition is inferred, it is difficult to speculate whether this error implies a higher than reported ambient WSOC concentration or simply a difference between the samples and daily filter measurements.

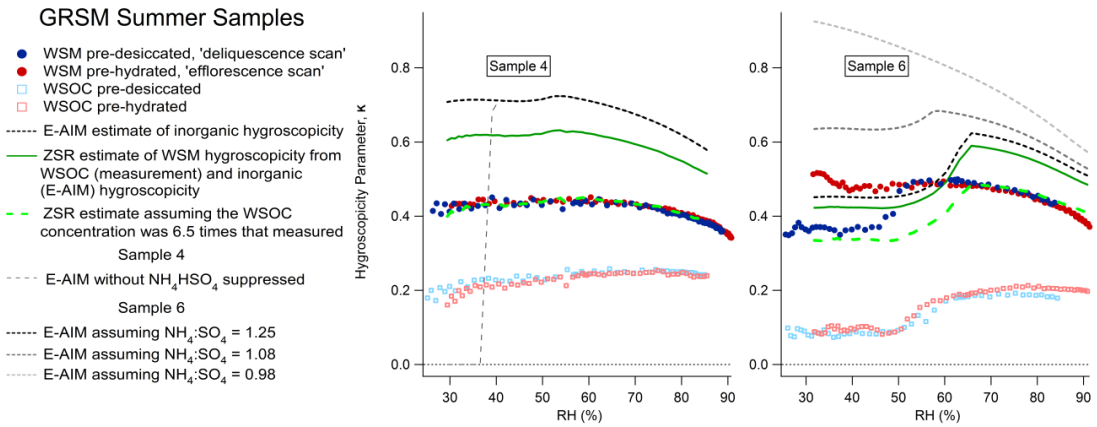

Figure 29: Contrasting expected and measured WSM hygroscopicity for samples taken during GRSM summer.

As with the SPL samples there is an ion imbalance. The molar ratios of ammonium to sulfate inferred for Samples 4 and 6 are 1.04 and 0.86, respectively. But there is less justification for assuming that ammonium is under-reported. Though sulfate levels have since dropped, GRSM has long been characterized by acidic sulfate aerosol in summer (Lowenthal et al., 2015). Nor was significant nitrate detected, which would have implied neutralized sulfate. The measured Sample 6 WSM hygroscopicity does show behavior consistent with the presence of letovicite, (NH4)3H(SO4)2, which would imply an ammonium to sulfate ratio greater than 1.

Though these results are uncertain, there are several features worth noting, including a potential depression of the deliquescence point of letovicite. Because the dominant fraction of both samples is acidic sulfate, the aerosols are expected to be fully aqueous at all measurement RH. Ammonium bisulfate does exhibit deliquescence (39% DRH) and a crystalline form, but its efflorescence point is below that encountered in the

H-TDMA used in this analysis (i.e., <15% RH) (Schlenker and Martin, 2005). Reflecting this, the formation of crystalline ammonium bisulfate is suppressed in the E-AIM estimates shown in Fig. 29. Despite this expectation, Sample 6 exhibits a distinct deliquescence transition near 50% RH. As noted above, this behavior appears to be most consistent with a fraction of crystalline letovicite. Figure 6 illustrates the impact of assuming different ammonium to sulfate ratios (i.e., assuming ammonium was under-reported to differing degrees). Depressed κ(RH) at low RH is due to the formation of crystalline letovicite. As is shown, the expected DRH differs from the measured DRH. E-AIM predicts some depression of DRH of letovicite, as some will dissolve into the surrounding aqueous solution. This is illustrated by the lower DRH of letovicite at lower ammonium-to-sulfate ratios in Fig. 29. There is more aqueous volume in proportion to letovicite and it is entirely consumed at lower RH. Here, the predicted depression was less than measured, suggesting that the presence of aqueous WSOC contributes to the effect.

Irregular Particle Morphology Rationalization for Anomalous Growth Factor at Low RH

This section addresses a measurement artifact that has been observed in other similar studies (Boreddy and Kawamura, 2016; Mikhailov et al., 2009; Mikhailov et al., 2004; Gysel et al., 2004). Analysis of samples taken during the GRSM Winter and SPL studies indicates separation between the pre-desiccated and pre-hydrated growth curves at low RH. The measured GF from these projects was also consistently below unity at low RH (as illustrated in Fig. 30, showing the results from GRSM Winter). These results

indicate a reduction in particle size as the aerosol is processed between the two DMAs in the TDMA. Though there are several plausible explanations for this behavior, including evaporation of volatile aerosol phase components, the parallels in Gysel et al. (2004) and Mikhailov et al. (2009) support the hypothesis that the size loss is due to the collapse of irregularly shaped particles. Regardless of the cause, in all measurements the pre-desiccated and pre-hydrated profiles eventually overlap and the smallest detected pre-hydrated size is assumed to be the most accurate assessment of dry volume for κ(RH) calculations and for inferring bulk WSOC hygroscopic properties.

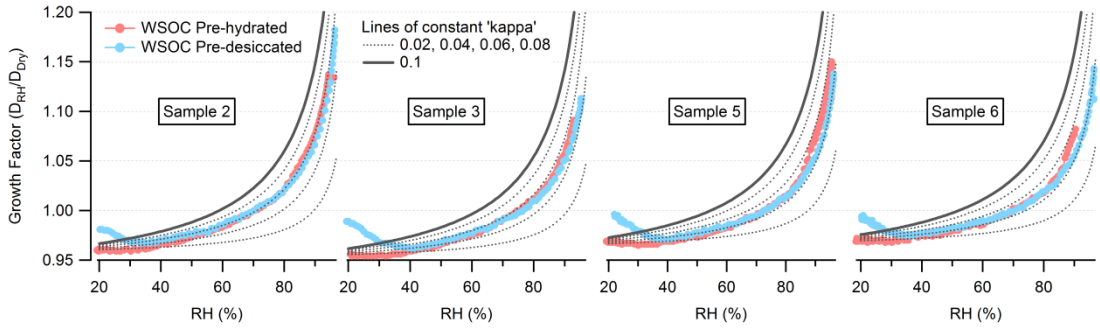

Figure 30: Hygroscopic growth measurements of WSOC samples from GRSM winter illustrating below unity growth factor and collapse of pre-desiccated scans at low RH.

The separation between the pre-desiccated and pre-hydrated measurements appears to relate to the aerosol being rehydrated. The aerosol entering the first DMA has been dried to low RH (<20%). The pre-hydrated aerosol is in the collapsed form even during measurements at very low RH because its conditioning begins with rehydration in the humidifying Nafion tube bundle (Fig. 24), while the pre-desiccated particles only collapse when the controlled RH is sufficient for them to substantially dissolve. This

link with dissolution is supported by the observance of this behavior only during the GRSM Winter, MORA and SPL projects: As shown in Fig. 26, the WSOC samples from these projects are the only ones that exhibit DRH greater than 30% RH, while the GRSM Summer and ACAD WSOC samples appear fully dissolved at the lowest RH measured. The link to dissolution is consistent with both the collapse of an irregularly shaped aerosol and kinetically limited evaporation. Nor are these rationalizations exclusive as evaporation can produce void fractions within a gel-like aerosol (Mikhailov et al., 2004).

Gysel et al. (2004), Mikhailov et al. (2009), and Boreddy and Kawamura (2016) each report on similar behavior for various WSOC. The report of Gysel et al. is most analogous and attributes this behavior to restructuring. Along with filter extracts of WSOC, they reproduced the phenomenon using Nordic reference humic and fulvic acids and Aldrich humic salts—i.e., substances unlikely to volatilize (Baltensperger et al., 2005). SEM micrographs in Gysel et al. (2004) depict approximately spherical particles; each of the three reports cited above suggests fissures and void fractions account for the apparent reduction in particle density of spray-dried aerosol. Mikhailov et al. (2009) detected similar behavior by oxalic acid aerosol. Though some dicarboxylic acids have been shown to exhibit evaporative losses in TDMAs, Mikhailov et al. (2009) demonstrated the stability of oxalic acid by varying its residence time within the system. Notably, Mikhailov et al. (2009) reported that rapidly drying atomized organic matter in its native, highly charged state could produce high void fraction (40-50%) aerogel-like aerosol. Here, as in Mikhailov et al. (2009), the initial drying of the highly-charged

atomizer spray is rapid and distinct from the drying of singly-charged particles within the TDMA system. The initial drying in this study was not as drastic (~25% vs. ~5% RH) but the similarities in process and result are convincing. These findings parallel other work linking drying rate (Wang et al., 2010) and particle charge (Berkland et al., 2004) to particle morphology. Alternatively, for succinic acid, the solvent used in the spray suspension has been found to dramatically affect morphology and void fraction (Carver and Snyder, 2012).

In sum, this behavior appears to be a measurement artifact. There is little direct evidence from this study to determine whether it is caused by irregularly shaped particles or evaporative losses, but similar findings by others support the former. For the purposes of this study, the cause is irrelevant and the minimum size reached by the pre-hydrated scan is assumed to most accurately reflect the amount of aerosol material involved in hygroscopic growth.

Conclusions

The WSOC in ambient aerosol has been shown to contribute to water uptake through hygroscopic growth and likely through complementary effects with other soluble aerosol components. WSOC was ubiquitous in PM2.5 collected during five month-long studies at various sites and was characterized by hygroscopic growth parameters (κ) ranging from 0.05 to 0.15. WSOC samples from GRSM Winter, MORA, and SPL deliquesced near 30% RH, while WSOC samples from GRSM Summer and ACAD did not display deliquescence, but instead were aqueous at all measured RH. No hysteresis was indicated for WSOC samples.

Contrasts between the hygroscopic growth of WSOC and total WSM samples from two of the studies suggest that soluble components in ambient aerosol can interact to enhance water uptake at atmospherically relevant RH. In particular, highly soluble, low-DRH WSOC can facilitate the gradual dissolution of sulfate-nitrate-ammonium (SNA) at RH below the typical deliquescence point for those substances. The hysteresis behavior of SNA-WSOC mixtures appears to be greatly truncated with mixed SNA-WSOC aerosol hydration instead characterized by gradual, reversible dissolution of SNA as RH increases from 40% to 80%.

Given the atmospheric abundance of internally mixed SNA and WSOC, this study not only indicates that WSOC contributes significantly to aerosol hygroscopicity but that a compartmentalized approach to WSOC and SNA hydration is flawed. The collection, isolation and analysis of WSOC from ambient aerosol provided a new perspective into the hydration behaviors of atmospherically complex mixtures of WSOC, but it is also a broad-brush and imprecise technique. Its primary value is in highlighting the complementary effects of WSOC and SNA hydration as a first-order impact on ambient aerosol hydration.

Data Availability

Hygroscopicity and CCN activity data for each sample are included in the article supplement to Taylor et al. (2017). Data related to the chemical analysis of aerosol samples are reported in Lowenthal et al. (2009, 2015), Hallar et al. (2013), Samburova et al. (2013), and Mazzoleni et al. (2012).

CHAPTER IV

CONCLUSIONS

As described in the conclusions of Chapters II and III, these findings on ambient aerosol hydration state and WSOC hygroscopicity are highly relevant to open questions about the behavior of atmospheric aerosol. Both are critical to predicting the amount of water associated with ambient aerosol, in turn influencing the roles aerosol play in atmospheric chemistry and climate, as well as their evolution and eventual fate in the atmosphere. These findings also permit conclusions about assumptions in IMPROVE light extinction algorithm, satisfying the objectives of the larger campaign and suggesting potential areas for improvement in the attribution of visibility impairment.

Chapter II explored the prevalence and impact of RH hysteresis in atmospheric aerosol, describing the use of a modified TDMA to detect which hydration state ambient aerosols occupied. This is a critical factor when estimating particulate water associated with atmospheric sulfate. As described in Chapter I, the current iteration of the IMPROVE LIRE estimates the light scattered by sulfate based upon the behavior of fully neutralized sulfate (ammonium sulfate) in its most-hydrated meta-stable form. This is partly justified by the substantial similarity between the sulfate-mass scattering efficiency under these assumptions, and that for more acidic forms of sulfate (i.e., the loss of assumed ammonium mass is offset by higher hygroscopicity). Chapter II demonstrates that this assumption is not sound: atmospheric sulfate was found in a less hydrated form at GRSM during the winter in ~1/6 of the measured aerosol. Remarkably,

the climatological monthly-average $f_S(RH)$ for GRSM in December is 4.13 (corresponding to RH of ~87%) (IMPROVE Web Site, 2017), preventing any direct application of these data. Yet it is reasonably likely that less-hydrated aerosol contribute to the regulation relevant 20% best visibility days.[5] For GRSM winter, at least, the original LIRE f(RH), which gradually transitioned from assuming less-hydrated to more-hydrated sulfate is more consistent with measurements.

Beyond undermining the LIRE assumption of ubiquitous most-hydrated state, the findings in Chapter II also highlight the impact of boundary layer dynamics and the vertical RH profile. While ambient hydration state may be expected to vary across viewscapes that involve elevation changes such as GRSM, the lack of variety in hydration state at MORA suggests that aerosol at low points or at the surface of a plain are most likely in the metastable state. For these reasons, it is difficult to posit a simple correction to the IMPROVE LIRE.

In summary, the measurements reported in Chapter II provide needed insight into the prevalence and dynamics of aerosol hydration state. While the results relate rationally to aerosol characteristics such as DRH and ERH, and to atmospheric conditions, few and limited measurements have been made to confirm these relationships. The findings undermine the current IMPROVE LIRE, but broadly extrapolating this result poses significant challenges.

[5] The RHR specifies that states must not allow further degradation on the 20% best days of each year versus the baseline period. It is admittedly likely the coarse treatment of RH for these calculations is much more problematic than the treatment of hydration state.

The findings in Chapter III also implicates the current IMPROVE LIRE, questioning both the lacking treatment of particulate water associated with WSOC and the isolated treatment of organic and inorganic aerosol constituents. First, WSOC was ubiquitous during each campaign, and represented a moderate portion (22-93%) of the measured total organic carbon—fractions consistent with other studies. Second, representative extracts of WSOC (46-100% of all captured WSOC) displayed relatively consistent hygroscopic growth across all studies (κ = 0.05-0.15 at 90% RH). Finally, mixtures of WSOC and inorganic ions took up substantially more (~50%) water at RH from 40-70% than expected from their isolated properties.

Unlike the hydration state results in Chapter II, the first two findings in this chapter both undermine the IMPROVE LIRE and provide a reasonably clear path forward. The LIRE should include an f(RH) for organic carbon. There is significant variability in the ratio of WSOC to OC, but it is never zero. Even a very conservative mass scattering enhancement would improve the accuracy of LIRE estimations. Figure 31 depicts the organic mass scattering enhancement resulting from assuming κ_{WSOC} = 0.1, DRH_{WSOC} = 25%, and WSOC/OC = 0.5. The Mie scattering calculations were performed based on the small organic mode (geometric mean diameter = 0.2 μm) describe by Pitchford et al. (2007). While these numbers are more modest than those for sulfate, the enhancement for December at GRSM, relying on the climatological RH (87%), would approach 20%. At remote sites dominated by organic compounds, this effect would be significant.

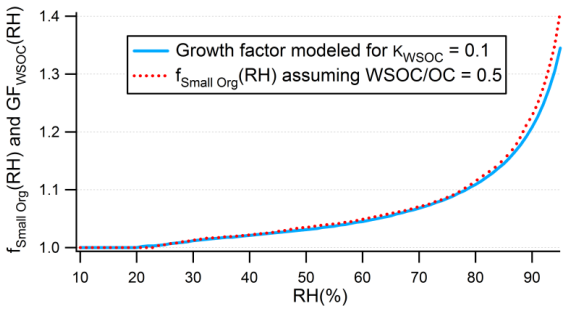

Figure 31: Organic mass scattering enhancement based on conservative assumptions.

The enhancement in water uptake driven by the mixing behavior observed at SPL described in Chapter III does not suggest any easy parameterization. That effect appeared to depended on the presence of partially dissolved solids, a quantity difficult to anticipate based on the IMPROVE measurements (most IMPROVE sites do not assess ammonium). However, the effect was persistent and may contribute significantly to visibility impairment under the right conditions.

In conclusion, the experiments done over the course of these four projects have yielded new insights into the hydration characteristics of atmospheric aerosol. Two key assumptions implicit in the US program of visibility regulation were evaluated. Contrary to both, aerosol exhibiting hysteresis were detected in both alternative hydration states and measurements of WSOC hygroscopic growth indicated significant water associated with the organic fraction of PM2.5. More broadly, these experiments will support future efforts to predict the roles of common aerosol constituents in climate and atmospheric chemistry, and ultimately their impacts on human well-being and the environment.

REFERENCES

ANDERSON, C., DIBB, J. E., GRIFFIN, R. J. & BERGIN, M. H. 2008. Simultaneous measurements of particulate and gas-phase water-soluble organic carbon concentrations at remote and urban-influenced locations. *Geophysical Research Letters,* 35**,** L13706.

ANSARI, A. S. & PANDIS, S. N. 1999. Prediction of multicomponent inorganic atmospheric aerosol behavior. *Atmospheric Environment,* 33**,** 745-757.

ASA-AWUKU, A., SULLIVAN, A. P., HENNIGAN, C. J., WEBER, R. J. & NENES, A. 2008. Investigation of molar volume and surfactant characteristics of water-soluble organic compounds in biomass burning aerosol. *Atmos. Chem. Phys.,* 8**,** 799-812.

BALTENSPERGER, U., KALBERER, M., DOMMEN, J., PAULSEN, D., ALFARRA, M., COE, H., FISSEHA, R., GASCHO, A., GYSEL, M. & NYEKI, S. 2005. Secondary organic aerosols from anthropogenic and biogenic precursors. *Faraday Discussions,* 130**,** 265-278.

BEISSINGER, S. R., ACKERLY, D. D., DOREMUS, H. & MACHLIS, G. 2017. *Science, Conservation, and National Parks*, University of Chicago Press, Chicago.

BERG, O. H., SWIETLICKI, E. & KREJCI, R. 1998. Hygroscopic growth of aerosol particles in the marine boundary layer over the Pacific and Southern Oceans during the First Aerosol Characterization Experiment (ACE 1). *J. Geophys. Res.,* 103**,** No. D13, 16535-16545.

BERKLAND, C., PACK, D. W. & KIM, K. 2004. Controlling surface nano-structure using flow-limited field-injection electrostatic spraying (FFESS) of poly(d,l-lactide-co-glycolide). *Biomaterials,* 25**,** 5649-5658.

BISKOS, G., PAULSEN, D., RUSSELL, L. M., BUSECK, P. R. & MARTIN, S. T. 2006. Prompt deliquescence and efflorescence of aerosol nanoparticles. *Atmos. Chem. Phys.,* 6**,** 4633-4642.

BOREDDY, S. K. R. & KAWAMURA, K. 2016. Hygroscopic growth of water-soluble matter extracted from remote marine aerosols over the western North Pacific: Influence of pollutants transported from East Asia. *Science of the Total Environment,* 557–558**,** 285-295.

BOUCHER, O., RANDALL, D., ARTAXO, P., BRETHERTON, C., FEINGOLD, G., FORSTER, P., KERMINEN, V.-M., KONDO, Y., LIAO, H., LOHMANN, U., RASCH, P., SATHEESH, S. K., SHERWOOD, S., STEVENS, B. & ZHANG,

X. Y. 2013. *Clouds and Aerosols, in: Climate Change 2013: The Physical Science Basis. Contribution of Working Group I to the Fifth Assessment Report of the Intergovernmental Panel on Climate Change,* Cambridge University Press, United Kingdom and New York, USA.

BRINK, H. M. T., VEEFKIND, J. P., WAIJERS-IJPELAAN, A. & VAN DER HAGE, J. C. 1996. Aerosol light-scattering in The Netherlands. *Atmospheric Environment,* 30**,** 4251-4261.

BROOKS, S. D., WISE, M. E., CUSHING, M. & TOLBERT, M. A. 2002. Deliquescence behavior of organic/ammonium sulfate aerosol. *Geophys. Res. Lett.,* 29**,** No. 19, 1917.

CARLTON, A. G. & TURPIN, B. J. 2013. Particle partitioning potential of organic compounds is highest in the Eastern US and driven by anthropogenic water. *Atmos. Chem. Phys.,* 13**,** 10203-10214.

CARRICO, C. M., KUS, P., ROOD, M. J., QUINN, P. K. & BATES, T. S. 2003. Mixtures of pollution, dust, sea salt, and volcanic aerosol during ACE-Asia: Radiative properties as a function of relative humidity. *J. Geophys. Res.,* 108**,** No. D23, 8650.

CARRICO, C. M., ROOD, M. J., OGREN, J. A., NEUSÜß, C., WIEDENSOHLER, A. & HEINTZENBERG, J. 2000. Aerosol optical properties at Sagres, Portugal during ACE-2. *Tellus B,* 52**,** 694-715.

CARVER, K. M. & SNYDER, R. C. 2012. Unexpected polymorphism and unique particle morphologies from monodisperse droplet evaporation. *Industrial & Engineering Chemistry Research,* 51**,** 15720-15728.

CERULLY, K. M., BOUGIATIOTI, A., HITE JR, J. R., GUO, H., XU, L., NG, N. L., WEBER, R. & NENES, A. 2015. On the link between hygroscopicity, volatility, and oxidation state of ambient and water-soluble aerosols in the southeastern United States. *Atmos. Chem. Phys.,* 15**,** 8679-8694.

CHARLSON, R. J., VANDERPOL, A. H., COVERT, D. S., WAGGONER, A. P. & AHLQUIST, N. C. 1974. $H_2SO_4/(NH_4)_2SO_4$ background aerosol: Optical detection in St. Louis region. *Atmospheric Environment (1967),* 8**,** 1257-1267.

CHOI, M. Y. & CHAN, C. K. 2002. The effects of organic species on the hygroscopic behaviors of inorganic aerosols. *Environmental Science & Technology,* 36**,** 2422-2428.

CHOW, J. C., WATSON, J. G., CHEN, L. W. A., ARNOTT, W. P., MOOSMÜLLER, H. & FUNG, K. 2004. Equivalence of elemental carbon by thermal/optical

reflectance and transmittance with different temperature protocols. *Environmental Science & Technology,* 38**,** 4414-4422.

CIOBANU, V. G., MARCOLLI, C., KRIEGER, U. K., ZUEND, A. & PETER, T. 2010. Efflorescence of ammonium sulfate and coated ammonium sulfate particles: evidence for surface nucleation. *The Journal of Physical Chemistry A,* 114**,** 9486-9495.

CLEGG, S. L. & BRIMBLECOMBE, P. 2005. Comment on the "Thermodynamic dissociation constant of the bisulfate ion from raman and ion interaction modeling studies of aqueous sulfuric acid at low temperatures". *The Journal of Physical Chemistry A,* 109**,** 2703-2706.

CLEGG, S. L., BRIMBLECOMBE, P. & WEXLER, A. S. 1998a. Thermodynamic model of the system H^+−NH4$^+$−Na^+−SO_4^{2-}−NO_3^-−Cl^-−H_2O at 298.15 K. *The Journal of Physical Chemistry A,* 102**,** 2155-2171.

CLEGG, S. L., BRIMBLECOMBE, P. & WEXLER, A. S. 1998b. Thermodynamic model of the system H^+−NH_4^+−SO_4^{2-}−NO_3^-−H_2O at tropospheric temperatures. *The Journal of Physical Chemistry A,* 102**,** 2137-2154.

CLEGG, S. L., SEINFELD, J. H. & BRIMBLECOMBE, P. 2001. Thermodynamic modelling of aqueous aerosols containing electrolytes and dissolved organic compounds. *Journal of Aerosol Science,* 32**,** 713-738

CLEGG, S. L. & WEXLER, A. S. 2011. Densities and apparent molar volumes of atmospherically important electrolyte solutions. Part 1: The solutes H_2SO_4, HNO_3, HCl, Na_2SO_4, $NaNO_3$, NaCl, $(NH_4)_2SO_4$, NH_4NO_3, and NH_4Cl from 0 to 50 °C, including extrapolations to very low temperature and to the pure liquid state, and $NaHSO_4$, NaOH, and NH_3 at 25 °C. *The Journal of Physical Chemistry A,* 115**,** 3393-3460.

COLBERG, C. A., LUO, B. P., WERNLI, H., KOOP, T. & PETER, T. 2003. A novel model to predict the physical state of atmospheric $H_2SO_4/NH_3/H_2O$ aerosol particles. *Atmos. Chem. Phys.,* 3**,** 909-924.

CRUZ, C. N. & PANDIS, S. N. 1997. A study of the ability of pure secondary organic aerosol to act as cloud condensation nuclei. *Atmospheric Environment,* 31**,** 2205-2214.

CRUZ, C. N. & PANDIS, S. N. 2000. Deliquescence and hygroscopic growth of mixed inorganic−organic atmospheric aerosol. *Environmental Science & Technology,* 34**,** 4313-4319.

DAY, D. E. & MALM, W. C. 2001. Aerosol light scattering measurements as a function of relative humidity: a comparison between measurements made at three different sites. *Atmospheric Environment,* 35**,** 5169-5176.

DAY, D. E., MALM, W. C. & AMES, R. B. 2001. Final report - southeastern aerosol and visibility study. *Interagency Monitoring of Protected Visual Enviroments Program Website.* Available: http://vista.cira.colostate.edu/improve/wp-content/uploads/ 2016/10/SEAVSReport.pdf [Accessed February, 2017].

DOUGLE, P. G., VEEFKIND, J. P. & TEN BRINK, H. M. 1998. Crystallisation of mixtures of ammonium nitrate, ammonium sulphate and soot. *Journal of Aerosol Science,* 29**,** 375-386.

DU, Z., HE, K., CHENG, Y., DUAN, F., MA, Y., LIU, J., ZHANG, X., ZHENG, M. & WEBER, R. 2014. A yearlong study of water-soluble organic carbon in Beijing II: Light absorption properties. *Atmospheric Environment,* 89**,** 235-241.

DUARTE, R. M. B. O. & DUARTE, A. C. 2005. Application of non-ionic solid sorbents (XAD resins) for the isolation and fractionation of water-soluble organic compounds from atmospheric aerosols. *Journal of Atmospheric Chemistry,* 51**,** 79-93.

DUARTE, R. M. B. O. & DUARTE, A. C. 2011. A critical review of advanced analytical techniques for water-soluble organic matter from atmospheric aerosols. *TrAC Trends in Analytical Chemistry,* 30**,** 1659-1671.

EL-ZANAN, H. S., LOWENTHAL, D. H., ZIELINSKA, B., CHOW, J. C. & KUMAR, N. 2005. Determination of the organic aerosol mass to organic carbon ratio in IMPROVE samples. *Chemosphere,* 60**,** 485-496.

ENGELHART, G. J., HILDEBRANDT, L., KOSTENIDOU, E., MIHALOPOULOS, N., DONAHUE, N. M. & PANDIS, S. N. 2011a. Water content of aged aerosol. *Atmos. Chem. Phys.,* 11**,** 911-920.

ENGELHART, G. J., MOORE, R. H., NENES, A. & PANDIS, S. N. 2011b. Cloud condensation nuclei activity of isoprene secondary organic aerosol. *Journal of Geophysical Research: Atmospheres,* 116**,** D02207.

EPA 1979. *Protecting Visibility: A Report to Congress*. EPA-450/5-79-008. Available: https://nepis.epa.gov [Accessesed February, 2017].

EPA 2016. Draft Guidance on Progress Tracking Metrics, Long-term Strategies, Reasonable Progress Goals and Other Requirements for Regional Haze State Implementation Plans for the Second Implementation Period. EPA-457/P-16-001. Available: https://www.epa.gov/sites/production/files/2016-

07/documents/draft_regional_haze_guidance_july_2016.pdf [Accessed February, 2017].

FIERZ-SCHMIDHAUSER, R., ZIEGER, P., GYSEL, M., KAMMERMANN, L., DECARLO, P. F., BALTENSPERGER, U. & WEINGARTNER, E. 2010. Measured and predicted aerosol light scattering enhancement factors at the high alpine site Jungfraujoch. *Atmos. Chem. Phys.,* 10**,** 2319-2333.

FOUNTOUKIS, C. & NENES, A. 2007. ISORROPIA II: a computationally efficient thermodynamic equilibrium model for K^+; Ca^{2+} ;Mg^{2+}; NH_4^+ ;Na^+ ;SO_4^{2-}; NO_3^-; Cl^-; H_2O aerosols. *Atmos. Chem. Phys.,* 7**,** 4639-4659.

FRANK, G. P., DUSEK, U. & ANDREAE, M. O. 2006. Technical note: A method for measuring size-resolved CCN in the atmosphere. *Atmos. Chem. Phys. Discuss.,* 6**,** 4879-4895.

FROSCH, M., BILDE, M., DECARLO, P. F., JURÁNYI, Z., TRITSCHER, T., DOMMEN, J., DONAHUE, N. M., GYSEL, M., WEINGARTNER, E. & BALTENSPERGER, U. 2011. Relating cloud condensation nuclei activity and oxidation level of α-pinene secondary organic aerosols. *Journal of Geophysical Research: Atmospheres,* 116**,** D22212.

FROSCH, M., BILDE, M., NENES, A., PRAPLAN, A. P., JURÁNYI, Z., DOMMEN, J., GYSEL, M., WEINGARTNER, E. & BALTENSPERGER, U. 2013. CCN activity and volatility of β-caryophyllene secondary organic aerosol. *Atmos. Chem. Phys.,* 13**,** 2283-2297.

GASPARINI, R., COLLINS, D. R., ANDREWS, E., SHERIDAN, P. J., OGREN, J. A. & HUDSON, J. G. 2006. Coupling aerosol size distributions and size-resolved hygroscopicity to predict humidity-dependent optical properties and cloud condensation nuclei spectra. *J. Geophys. Res.,* 111**,** D05S13.

GASPARINI, R., LI, R. & COLLINS, D. R. 2004. Integration of size distributions and size-resolved hygroscopicity measured during the Houston Supersite for compositional categorization of the aerosol. *Atmospheric Environment,* 38**,** 3285-3303.

GRANT, K. E., CHUANG, C. C., GROSSMAN, A. S. & PENNER, J. E. 1999. Modeling the spectral optical properties of ammonium sulfate and biomass burning aerosols: parameterization of relative humidity effects and model results. *Atmospheric Environment,* 33**,** 2603-2620.

GUO, H., XU, L., BOUGIATIOTI, A., CERULLY, K. M., CAPPS, S. L., HITE JR, J. R., CARLTON, A. G., LEE, S. H., BERGIN, M. H., NG, N. L., NENES, A. &

WEBER, R. J. 2015. Fine-particle water and pH in the southeastern United States. *Atmos. Chem. Phys.,* 15**,** 5211-5228.

GYSEL, M., WEINGARTNER, E., NYEKI, S., PAULSEN, D., BALTENSPERGER, U., GALAMBOS, I. & KISS, G. 2004. Hygroscopic properties of water-soluble matter and humic-like organics in atmospheric fine aerosol. *Atmos. Chem. Phys.,* 4**,** 35-50.

GYSEL, M., MCFIGGANS, G. B. & COE, H. 2009. Inversion of tandem differential mobility analyser (TDMA) measurements. *Journal of Aerosol Science,* 40**,** 134-151.

HALLAR, A. G., LOWENTHAL, D. H., CLEGG, S. L., SAMBUROVA, V., TAYLOR, N., MAZZOLENI, L. R., ZIELINSKA, B. K., KRISTENSEN, T. B., CHIROKOVA, G., MCCUBBIN, I. B., DODSON, C. & COLLINS, D. 2013. Chemical and hygroscopic properties of aerosol organics at Storm Peak Laboratory. *Journal of Geophysical Research: Atmospheres,* 118**,** 4767-4779.

HALLQUIST, M., WENGER, J. C., BALTENSPERGER, U., RUDICH, Y., SIMPSON, D., CLAEYS, M., DOMMEN, J., DONAHUE, N. M., GEORGE, C., GOLDSTEIN, A. H., HAMILTON, J. F., HERRMANN, H., HOFFMANN, T., IINUMA, Y., JANG, M., JENKIN, M. E., JIMENEZ, J. L., KIENDLER-SCHARR, A., MAENHAUT, W., MCFIGGANS, G., MENTEL, T. F., MONOD, A., PRÉVÔT, A. S. H., SEINFELD, J. H., SURRATT, J. D., SZMIGIELSKI, R. & WILDT, J. 2009. The formation, properties and impact of secondary organic aerosol: current and emerging issues. *Atmos. Chem. Phys.,* 9**,** 5155-5236.

HAND, J. L., COPELAND, S., DAY, D. A., DILLNER, A., INDRESAND, H., MALM, W. C., MCDADE, C., MOORE, C., PITCHFORD, M., SCHICTEL, B. & WATSON, J. G. 2011. Spatial and seasonal patterns and temporal variability of aaze and its constituents in the United States: Report V June 2011. *Interagency Monitoring of Protected Visual Enviroments Program Website.* Available: http://vista.cira.colostate.edu/Improve/improve-reports/ [Accessed February, 2017].

HAND, J. L. & MALM, W. C. 2006. *Review of the IMPROVE Equation for Estimating Ambient Light Extinction Coefficients*, Cooperative Institute for Research in the Atmosphere, Colorado State University, 0737-5352-71. Available: http://vista.cira.colostate.edu/Improve/gray-literature/ [Accessed February, 2017].

HANSSON, H. C., ROOD, M. J., KOLOUTSOU-VAKAKIS, S., HÄMERI, K., ORSINI, D. & WIEDENSOHLER, A. 1998. NaCl aerosol particle

hygroscopicity dependence on mixing with organic compounds. *Journal of Atmospheric Chemistry,* 31**,** 321-346.

HAYWOOD, J. M., ROBERTS, D. L., SLINGO, A., EDWARDS, J. M. & SHINE, K. P. 1997. General circulation model calculations of the direct radiative forcing by anthropogenic sulfate and fossil-fuel soot aerosol. *Journal of Climate,* 10**,** 1562-1577.

HERRMANN, H., SCHAEFER, T., TILGNER, A., STYLER, S. A., WELLER, C., TEICH, M. & OTTO, T. 2015. Tropospheric aqueous-phase chemistry: Kinetics, mechanisms, and its coupling to a changing gas phase. *Chemical Reviews,* 115**,** 4259-4334.

HODAS, N., ZUEND, A., MUI, W., FLAGAN, R. C. & SEINFELD, J. H. 2015. Influence of particle-phase state on the hygroscopic behavior of mixed organic–inorganic aerosols. *Atmos. Chem. Phys.,* 15**,** 5027-5045.

IMPROVE WEB SITE, 2017. *Interagency Monitoring of Protected Visual Environments Web Site and Database* [Online]. Available: http://vista.cira.colostate.edu/Improve/ [Accessed February, 2017].

KHLYSTOV, A., STANIER, C. O., TAKAHAMA, S. & PANDIS, S. N. 2005. Water content of ambient aerosol during the Pittsburgh Air Quality Study. *J. Geophys. Res.,* 110**,** D07S10.

KIRILLOVA, E. N., ANDERSSON, A., HAN, J., LEE, M. & GUSTAFSSON, Ö. 2014. Sources and light absorption of water-soluble organic carbon aerosols in the outflow from northern China. *Atmos. Chem. Phys.,* 14**,** 1413-1422.

KIRILLOVA, E. N., ANDERSSON, A., SHEESLEY, R. J., KRUSÅ, M., PRAVEEN, P. S., BUDHAVANT, K., SAFAI, P. D., RAO, P. S. P. & GUSTAFSSON, Ö. 2013. 13C- and 14C-based study of sources and atmospheric processing of water-soluble organic carbon (WSOC) in South Asian aerosols. *Journal of Geophysical Research: Atmospheres,* 118**,** 614-626.

KRISTENSEN, T. B., WEX, H., NEKAT, B., NØJGAARD, J. K., PINXTEREN, D. V., LOWENTHAL, D. H., MAZZOLENI, L. R., DIECKMANN, K., KOCH, C. B., MENTEL, T. F., HERRMANN, H., HALLAR, A. G., STRATMANN, F. & BILDE, M. 2012. Hygroscopic growth and CCN activity of HULIS from different environments. *Journal of Geophysical Research,* 117, D22203.

LOWENTHAL, D. H. & KUMAR, N. 2003. PM2.5 mass and light extinction reconstruction in IMPROVE. *Journal of the Air & Waste Management Association,* 53**,** 1109-1120.

LOWENTHAL, D., ZIELINSKA, B., MASON, B., SAMY, S., SAMBUROVA, V., COLLINS, D., SPENCER, C., TAYLOR, N., ALLEN, J. & KUMAR, N. 2009. Aerosol characterization studies at Great Smoky Mountains National Park, summer 2006. *J. Geophys. Res.,* 114**,** D08206.

LOWENTHAL, D., ZIELINSKA, B., SAMBUROVA, V., COLLINS, D., TAYLOR, N. & KUMAR, N. 2014. Evaluation of assumptions for estimating chemical light extinction at U.S. national parks. *Journal of the Air & Waste Management Association,* 65**,** 249-260.

MALM, W. C. & DAY, D. E. 2001. Estimates of aerosol species scattering characteristics as a function of relative humidity. *Atmospheric Environment,* 35**,** 2845-2860.

MALM, W. C. & PITCHFORD, M. L. 1997. Comparison of calculated sulfate scattering efficiencies as estimated from size-resolved particle measurements at three national locations. *Atmospheric Environment,* 31**,** 1315-1325.

MALM, W. C., SISLER, J. F., HUFFMAN, D., ELDRED, R. A. & CAHILL, T. A. 1994. Spatial and seasonal trends in particle concentration and optical extinction in the United States. *Journal of Geophysical Research: Atmospheres,* 99**,** No. D1, 1347-1370.

MARCOLLI, C., LUO, B. & PETER, T. 2004. Mixing of the organic aerosol fractions: liquids as the thermodynamically stable phases. *The Journal of Physical Chemistry A,* 108**,** 2216-2224.

MARTIN, S. T. 2000. Phase transitions of aqueous atmospheric particles. *Chemical Reviews,* 100**,** 3403-3454.

MARTIN, S. T., HAN, J., HO, HUNG, H. & MING 2001. The size effect of hematite and corundum inclusions on the efflorescence relative humidities of aqueous ammonium sulfate particles. *Geophys. Res. Lett.,* 28**,** No. 13, 2601-2604.

MARTIN, S. T., HUNG, H. M., PARK, R. J., JACOB, D. J., SPURR, R. J. D., CHANCE, K. V. & CHIN, M. 2004. Effects of the physical state of tropospheric ammonium-sulfate-nitrate particles on global aerosol direct radiative forcing. *Atmos. Chem. Phys.,* 4**,** 183-214.

MARTIN, S. T., ROSENOERN, T., CHEN, Q. & COLLINS, D. R. 2008. Phase changes of ambient particles in the Southern Great Plains of Oklahoma. *Geophys. Res. Lett.,* 35**,** L22801.

MAZZOLENI, L. R., SARANJAMPOUR, P., DALBEC, M. M., SAMBUROVA, V., HALLAR, A. G., ZIELINSKA, B., LOWENTHAL, D. & KOHL, S. 2012.

Identification of water-soluble organic carbon in nonurban aerosols using ultrahigh-resolution FT-ICR mass spectrometry: organic anions. *Environmental Chemistry,* 9**,** 285-297.

MIFFLIN, A. L., SMITH, M. L. & MARTIN, S. T. 2009. Morphology hypothesized to influence aerosol particle deliquescence. *Physical Chemistry Chemical Physics,* 11**,** 10095-10107.

MIKHAILOV, E., VLASENKO, S., MARTIN, S. T., KOOP, T. & PÖSCHL, U. 2009. Amorphous and crystalline aerosol particles interacting with water vapor: conceptual framework and experimental evidence for restructuring, phase transitions and kinetic limitations. *Atmos. Chem. Phys.,* 9**,** 9491-9522.

MIKHAILOV, E., VLASENKO, S., NIESSNER, R. & PÖSCHL, U. 2004. Interaction of aerosol particles composed of protein and saltswith water vapor: hygroscopic growth and microstructural rearrangement. *Atmos. Chem. Phys.,* 4**,** 323-350.

MIYAZAKI, Y., FU, P. Q., KAWAMURA, K., MIZOGUCHI, Y. & YAMANOI, K. 2012. Seasonal variations of stable carbon isotopic composition and biogenic tracer compounds of water-soluble organic aerosols in a deciduous forest. *Atmos. Chem. Phys.,* 12**,** 1367-1376.

PETTERS, M. D. & KREIDENWEIS, S. M. 2007. A single parameter representation of hygroscopic growth and cloud condensation nucleus activity. *Atmos. Chem. Phys.,* 7**,** 1961-1971.

PETTERS, M. D. & KREIDENWEIS, S. M. 2013. A single parameter representation of hygroscopic growth and cloud condensation nucleus activity – Part 3: Including surfactant partitioning. *Atmos. Chem. Phys.,* 13**,** 1081-1091.

PITCHFORD, M. L. & MALM, W. C. 1994. Development and applications of a standard visual index. *Atmospheric Environment,* 28**,** 1049-1054.

PITCHFORD, M., MALM, W., SCHICTEL, B., KUMAR, N., LOWENTHAL, D. & HAND, J. 2007. Revised algorithm for estimating light extinction from IMPROVE particle speciation data. *Journal of the Air & Waste Management Association,* 57**,** 1326-1336.

PITCHFORD, M. L. & MCMURRY, P. H. 1994. Relationship between measured water-vapor growth and chemistry of atmospheric aerosol for Grand-Canyon, Arizona, in Winter 1990. *Atmospheric Environment,* 28**,** 827-839.

PSICHOUDAKI, M. & PANDIS, S. N. 2013. Atmospheric aerosol water-soluble organic carbon measurement: A theoretical analysis. *Environmental Science & Technology,* 47**,** 9791-9798.

RISSLER, J., VESTIN, A., SWIETLICKI, E., FISCH, G., ZHOU, J., ARTAXO, P. & ANDREAE, M. O. 2006. Size distribution and hygroscopic properties of aerosol particles from dry-season biomass burning in Amazonia. *Atmospheric Chemistry and Physics,* 6**,** 471-491.

ROOD, M. J., COVERT, D. S. & LARSON, T. V. 1987. Hygroscopic properties of atmospheric aerosol in Riverside, California. *Tellus B,* 39B**,** 383-397.

ROOD, M. J., SHAW, M. A., LARSON, T. V. & COVERT, D. S. 1989. Ubiquitous nature of ambient metastable aerosol. *Nature,* 337**,** 537-539.

ROSE, D., GUNTHE, S. S., MIKHAILOV, E., FRANK, G. P., DUSEK, U., ANDREAE, M. O. & PÖSCHL, U. 2008. Calibration and measurement uncertainties of a continuous-flow cloud condensation nuclei counter (DMT-CCNC): CCN activation of ammonium sulfate and sodium chloride aerosol particles in theory and experiment. *Atmos. Chem. Phys.,* 8**,** 1153-1179.

ROSENOERN, T., PAULSEN, D. & MARTIN, S. T. 2009. The 1-by-3 Tandem Differential Mobility Analyzer for measurement of the irreversibility of the hygroscopic growth factor. *Aerosol Science and Technology,* 43**,** 641 - 652.

ROSENOERN, T., SCHLENKER, J. C. & MARTIN, S. T. 2008. Hygroscopic growth of multicomponent aerosol particles influenced by several cycles of relative humidity. *The Journal of Physical Chemistry A,* 112**,** 2378-2385.

RYAN, P. A., LOWENTHAL, D. & KUMAR, N. 2005. Improved light extinction reconstruction in Interagency Monitoring of Protected Visual Environments. *Journal of the Air & Waste Management Association,* 55**,** 1751-1759.

SAMBUROVA, V., HALLAR, A. G., MAZZOLENI, L. R., SARANJAMPOUR, P., LOWENTHAL, D., KOHL, S. D. & ZIELINSKA, B. 2013. Composition of water-soluble organic carbon in non-urban atmospheric aerosol collected at the Storm Peak Laboratory. *Environmental Chemistry,* 10**,** 370-380.

SANTARPIA, J. L., LI, R. & COLLINS, D. R. 2004. Direct measurement of the hydration state of ambient aerosol populations. *J. Geophys. Res.,* 109**,** D18209.

SCHLENKER, J. C. & MARTIN, S. T. 2005. Crystallization pathways of sulfate−nitrate−ammonium aerosol particles. *The Journal of Physical Chemistry A,* 109**,** 9980-9985.

SEINFELD, J. H. & PANDIS, S. N. 2006. Atmospheric Chemistry and Physics, from Air Pollution to Climate Change. 2nd ed. John Wiley & Sons, Inc., Hoboken, New Jersey.

SISLER, J. F., HUFFMAN, D., LATIMER, D. A., MALM, W. C. & PITCHFORD, M. 1993. spatial and temporal patterns and the chemical composition of the haze in the United States: An analysis of data from the IMPROVE network, 1988-1991.

SJOGREN, S., GYSEL, M., WEINGARTNER, E., ALFARRA, M. R., DUPLISSY, J., COZIC, J., CROSIER, J., COE, H. & BALTENSPERGER, U. 2008. Hygroscopicity of the submicrometer aerosol at the high-alpine site Jungfraujoch, 3580 m a.s.l., Switzerland. *Atmos. Chem. Phys.,* 8**,** 5715-5729.

SMITH, J. N., BARSANTI, K. C., FRIEDLI, H. R., EHN, M., KULMALA, M., COLLINS, D. R., SCHECKMAN, J. H., WILLIAMS, B. J. & MCMURRY, P. H. 2010. Observations of aminium salts in atmospheric nanoparticles and possible climatic implications. *Proceedings of the National Academy of Sciences,* 107**,** 6634-6639.

SMITH, M. L., KUWATA, M. & MARTIN, S. T. 2011. Secondary organic material produced by the dark ozonolysis of α-pinene minimally affects the deliquescence and efflorescence of ammonium sulfate. *Aerosol Science and Technology,* 45**,** 244 - 261.

STANIER, C. O., KHLYSTOV, A. Y., CHAN, W. R., MANDIRO, M. & PANDIS, S. N. 2004. A method for the *in situ* measurement of fine aerosol water content of ambient aerosols: The Dry-Ambient Aerosol Size Spectrometer (DAASS). Special issue of Aerosol Science and Technology on Findings from the Fine Particulate Matter Supersites Program. *Aerosol Science and Technology,* 38**,** 215-228.

SUDA, S. R., PETTERS, M. D., MATSUNAGA, A., SULLIVAN, R. C., ZIEMANN, P. J. & KREIDENWEIS, S. M. 2012. Hygroscopicity frequency distributions of secondary organic aerosols. *J. Geophys. Res.,* 117**,** D04207.

SULLIVAN, A. P. & WEBER, R. J. 2006. Chemical characterization of the ambient organic aerosol soluble in water: 1. Isolation of hydrophobic and hydrophilic fractions with a XAD-8 resin. *Journal of Geophysical Research: Atmospheres,* 111**,** D05314.

SULLIVAN, A. P., WEBER, R. J., CLEMENTS, A. L., TURNER, J. R., BAE, M. S. & SCHAUER, J. J. 2004. A method for on-line measurement of water-soluble organic carbon in ambient aerosol particles: Results from an urban site. *Geophysical Research Letters,* 31**,** L13105.

SUN, Y., ZHANG, Q., ZHENG, M., DING, X., EDGERTON, E. S. & WANG, X. 2011. Characterization and source apportionment of water-soluble organic matter in atmospheric fine particles (PM2.5) with High-Resolution Aerosol Mass

Spectrometry (HR-AMS) and GC–MS. *Environmental Science & Technology,* 45**,** 4854-4861.

SWIETLICKI, E., HANSSON, H. C., HÄMERI, K., SVENNINGSSON, B., MASSLING, A., MCFIGGANS, G., MCMURRY, P. H., PETÄJÄ, T., TUNVED, P., GYSEL, M., TOPPING, D., WEINGARTNER, E., BALTENSPERGER, U., RISSLER, J., WIEDENSOHLER, A. & KULMALA, M. 2008. Hygroscopic properties of submicrometer atmospheric aerosol particles measured with H-TDMA instruments in various environments—a review. *Tellus B,* 60**,** 432-469.

SWIETLICKI, E., ZHOU, J., COVERT, D. S., HÄMERI, K., BUSCH, B., VÄKEVA, M., DUSEK, U., BERG, O. H., WIEDENSOHLER, A., AALTO, P., MÄKELÄ, J., MARTINSSON, B. G., PAPASPIROPOULOS, G., MENTES, B., FRANK, G. & STRATMANN, F. 2000. Hygroscopic properties of aerosol particles in the north-eastern Atlantic during ACE-2. *Tellus B,* 52**,** 201-227.

TANG, I. N. 1996. Chemical and size effects of hygroscopic aerosols on light scattering coefficients. *J. Geophys. Res.,* 101**,** No. D14, 19245-19250.

TANG, I. N. 1997. Thermodynamic and optical properties of mixed-salt aerosols of atmospheric importance. *Journal of Geophysical Research: Atmospheres,* 102**,** No. D2, 1883-1893.

TANG, I. N. & MUNKELWITZ, H. R. 1984. An investigation of solute nucleation in levitated solution droplets. *Journal of Colloid and Interface Science,* 98**,** 430-438.

TANG, I. N. & MUNKELWITZ, H. R. 1994. Water activities, densities, and refractive indices of aqueous sulfates and sodium nitrate droplets of atmospheric importance. *J. Geophys. Res.,* 99**,** No. D9, 18801-18808.

TANG, I. N., MUNKELWITZ, H. R. & DAVIS, J. G. 1978. Aerosol growth studies -- IV. Phase transformation of mixed salt aerosols in a moist atmosphere. *Journal of Aerosol Science,* 9**,** 505-511.

TAYLOR, N. F., COLLINS, D. R., LOWENTHAL, D. H., MCCUBBIN, I. B., HALLAR, A. G., SAMBUROVA, V., ZIELINSKA, B., KUMAR, N. & MAZZOLENI, L. R. 2017. Hygroscopic growth of water soluble organic carbon isolated from atmospheric aerosol collected at US national parks and Storm Peak Laboratory. *Atmos. Chem. Phys.,* 17**,** 2555-2571.

TAYLOR, N. F., COLLINS, D. R., SPENCER, C. W., LOWENTHAL, D. H., ZIELINSKA, B., SAMBUROVA, V. & KUMAR, N. 2011. Measurement of

ambient aerosol hydration state at Great Smoky Mountains National Park in the Southeastern United States. *Atmos. Chem. Phys.,* 11**,** 12085-12107.

TIMONEN, H., CARBONE, S., AURELA, M., SAARNIO, K., SAARIKOSKI, S., NG, N. L., CANAGARATNA, M. R., KULMALA, M., KERMINEN, V.-M., WORSNOP, D. R. & HILLAMO, R. 2013. Characteristics, sources and water-solubility of ambient submicron organic aerosol in springtime in Helsinki, Finland. *Journal of Aerosol Science,* 56**,** 61-77.

VU, T., DELGADO-SABORIT, J. & HARRISON, R. 2015. A review of hygroscopic growth factors of submicron aerosols from different sources and its implication for calculation of lung deposition efficiency of ambient aerosols. *Air Quality, Atmosphere & Health***,** 1-12.

WANG, J., HOFFMANN, A. A., PARK, R. J., JACOB, D. J. & MARTIN, S. T. 2008a. Global distribution of solid and aqueous sulfate aerosols: Effect of the hysteresis of particle phase transitions. *J. Geophys. Res.,* 113**,** D11206.

WANG, J., JACOB, D. J. & MARTIN, S. T. 2008b. Sensitivity of sulfate direct climate forcing to the hysteresis of particle phase transitions. *J. Geophys. Res.,* 113**,** D11207.

WANG, W., ROOD, M. J., CARRICO, C. M., COVERT, D. S., QUINN, P. K. & BATES, T. S. 2007. Aerosol optical properties along the northeast coast of North America during the New England Air Quality Study Intercontinental Transport and Chemical Transformation 2004 campaign and the influence of aerosol composition. *J. Geophys. Res.,* 112**,** D10S23.

WANG, Z., KING, S. M., FRENEY, E., ROSENOERN, T., SMITH, M. L., CHEN, Q., KUWATA, M., LEWIS, E. R., PÖSCHL, U., WANG, W., BUSECK, P. R. & MARTIN, S. T. 2010. The Dynamic Shape Factor of Sodium Chloride Nanoparticles as Regulated by Drying Rate. *Aerosol Science and Technology,* 44**,** 939 - 953.

WU, Z. J., NOWAK, A., POULAIN, L., HERRMANN, H. & WIEDENSOHLER, A. 2011. Hygroscopic behavior of atmospherically relevant water-soluble carboxylic salts and their influence on the water uptake of ammonium sulfate. *Atmos. Chem. Phys. Discuss.,* 11**,** 7693-7714.

ZARDINI, A. A., SJOGREN, S., MARCOLLI, C., KRIEGER, U. K., GYSEL, M., WEINGARTNER, E., BALTENSPERGER, U. & PETER, T. 2008. A combined particle trap/HTDMA hygroscopicity study of mixed inorganic/organic aerosol particles. *Atmos. Chem. Phys.,* 8**,** 5589-5601.

ZELENYUK, A., CAI, Y. & IMRE, D. 2006. From agglomerates of spheres to irregularly shaped particles: Determination of dynamic shape factors from measurements of mobility and vacuum aerodynamic diameters. *Aerosol Science and Technology,* 40**,** 197 - 217.

ZHOU, J. C., SWIETLICKI, E., BERG, O. H., AALTO, P. P., HAMERI, K., NILSSON, E. D. & LECK, C. 2001. Hygroscopic properties of aerosol particles over the central Arctic Ocean during summer. *Journal of Geophysical Research-Atmospheres,* 106**,** No. D23, 32111-32123.